

RETRIEVAL OF NON-SPHERICAL DUST AEROSOL PROPERTIES FROM
SATELLITE OBSERVATIONS

A Dissertation

by

XIN HUANG

Submitted to the Office of Graduate Studies of
Texas A&M University
in partial fulfillment of the requirements for the degree of

DOCTOR OF PHILOSOPHY

| | |
|------------------------|--------------------|
| Chair of Committee, | George W. Kattawar |
| Co-Chair of Committee, | Ping Yang |
| Committee Members, | Edward S. Fry |
| | Roland E. Allen |
| Head of Department, | George R. Welch |

August 2013

Major Subject: Physics

Copyright 2013 Xin Huang

ABSTRACT

An accurate and generalized global retrieval algorithm from satellite observations is a prerequisite to understand the radiative effect of atmospheric aerosols on the climate system. Current operational aerosol retrieval algorithms are limited by the inversion schemes and suffering from the non-uniqueness problem. In order to solve these issues, a new algorithm is developed for the retrieval of non-spherical dust aerosol over land using multi-angular radiance and polarized measurements of the POLDER (POLarization and Directionality of the Earth's Reflectances) and wide spectral high-resolution measurements of the MODIS (MODerate resolution Imaging Spectro-radiometer).

As the first step to account for the non-sphericity of irregularly shaped dust aerosols in the light scattering problem, the spheroidal model is introduced. To solve the basic electromagnetic wave scattering problem by a single spheroid, we developed an algorithm, by transforming the transcendental infinite-continued-fraction-form eigen equation into a symmetric tri-diagonal linear system, for the calculation of the spheroidal angle function, radial functions of the first and second kind, as well as the corresponding first order derivatives. A database is developed subsequently to calculate the bulk scattering properties of dust aerosols for each channel of the satellite instruments.

For the purpose of simulation of satellite observations, a code is developed to solve the VRTE (Vector Radiative Transfer Equation) for the coupled atmosphere-surface system using the adding-doubling technique. An alternative fast algorithm, where all the solid angle integrals are converted to summations on an icosahedral grid, is also proposed to speed-up the code. To make the model applicable to various land and

ocean surfaces, a surface BRDF (Bidirectional Reflectance Distribution Function) library is embedded into the code.

Considering the complimentary features of the MODIS and the POLDER, the collocated measurements of these two satellites are used in the retrieval process. To reduce the time spent on the simulation of dust aerosol scattering properties, a single-scattering property database of tri-axial ellipsoid is incorporated. In addition, atmospheric molecule correction is considered using the LBLRTM (Line-By-Line Radiative Transfer Model). The Levenberg-Marquardt method was employed to retrieve all the interested dust aerosol parameters and surface parameters simultaneously. As an example, dust aerosol properties retrieved over the Sahara Desert are presented.

DEDICATION

This dissertation is dedicated to my mother, who always supported me through my life.

ACKNOWLEDGEMENTS

I would like to express the deepest appreciation, to my committee chair Dr. George W. Kattawar and co-chair Dr. Ping Yang, for their guidance and support during my doctoral study. Without their help, this dissertation would not have been possible.

I would also like to offer my special thanks to my committee members, Dr. Edward S. Fry and Dr. Roland E. Allen, whose brilliant works on light scattering experiments and condensed matter physics greatly inspired me.

In addition, I would like to thank all the former and current group members for the helpful discussions and encouragements when I was facing difficulties in my research.

The reported research was partly supported by NSF (ATM-0803779), NASA (NNX11AK39G), a sub-award from the University of Wisconsin (301K630), and the endowment funds related to the David Bullock Harris Chair in Geosciences at the College of Geosciences, Texas A&M University

Finally, I would like to thank my families and friends for their persistent attention and support.

NOMENCLATURE

| | |
|---------|---|
| AERONET | AErosol RObotic NETwork |
| ADDA | Amsterdam Discrete Dipole Approximation |
| ADT | Anomalous Diffraction Theory |
| BLAS | Basic Linear Algebra Subroutine |
| BRDF | Bidirectional Reflectance Distribution Function |
| BPDF | Bidirectional Polarization Distribution Function |
| CCN | Cloud Condensation Nuclei |
| CNES | French Space Agency |
| DDA | Discrete Dipole Approximation |
| DoLP | Degree of Linear Polarization |
| EOFs | Empirical Orthogonal Functions |
| EPC | Extended Precision Calculation |
| FDTD | Finite Difference Time Domain Method |
| GOME-2 | Global Ozone Monitoring Experiment-2 |
| HITRAN | HIgh-resolution TRansmission molecular AbsorptioN database |
| IGOM | Improved Geometric Optics Method |
| LBLRTM | Line-By-Line Radiative Transfer Model |
| LUT | Look-Up-Table |
| NASA | National Aeronautics and Space Administration |
| MISR | Multi-angle Imaging Spectro-Radiometer |
| MODIS | MODerate resolution Imaging Spectro-radiometer |
| PARASOL | Polarization and Anisotropy of Reflectances for Atmospheric Sciences coupled with Observations from a Lidar |

| | |
|---------|---|
| POLDER | POLArization and Directionality of the Earth's Reflectances |
| PSTD | Pseudo-Spectral Time Domain method |
| SEM | Scanning Electron Microscope |
| SOS | Successive Order of Scattering Method |
| SVM | Separation of Variables Method |
| SMART | Simulated MISR Ancillary Radiative Transfer |
| TOA | Top Of Atmosphere |
| UV | UltraViolet |
| VDISORT | Vector DIScrete Ordinates Radiative Transfer program for a multi-layered plane-parallel medium |
| VRTE | Vector Radiative Transfer Equation |

TABLE OF CONTENTS

| | Page |
|--|------|
| ABSTRACT | ii |
| DEDICATION | iv |
| ACKNOWLEDGEMENTS | v |
| NOMENCLATURE | vi |
| TABLE OF CONTENTS | viii |
| LIST OF FIGURES | x |
| LIST OF TABLES | xv |
| 1. INTRODUCTION | 1 |
| 2. SINGLE-SCATTERING PROPERTIES OF NON-SPHERICAL DUST AEROSOLS | 9 |
| 2.1 Introduction | 9 |
| 2.2 Fundamental Theory of Single Electromagnetic Scattering | 14 |
| 2.3 Computation of Spheroidal Functions | 24 |
| 2.3.1 Spheroidal Coordinate Systems | 25 |
| 2.3.2 Separation of Variables for the Scalar Helmholtz Equation | 25 |
| 2.3.3 The Prolate Spheroidal Angle Function | 27 |
| 2.3.4 The Prolate Spheroidal Radial Function | 30 |
| 2.3.5 Results | 32 |
| 2.4 Single-Scattering Property Database of Mineral Dust Aerosols | 33 |
| 2.5 Narrowband Bulk Scattering Properties | 37 |
| 2.6 Summary | 40 |
| 3. FORWARD RADIATIVE TRANSFER MODEL | 42 |
| 3.1 Introduction | 42 |
| 3.2 Vector Radiative Transfer Equation for Plane-Parallel and Turbid Media | 44 |
| 3.3 The Adding-Doubling Technique | 48 |
| 3.3.1 Adding Equations | 50 |
| 3.3.2 Fourier Transformation | 53 |
| 3.3.3 Adding-Doubling in Supermatrices Form | 56 |
| 3.3.4 Separation of Single-Scattering | 59 |

| | | |
|-------|--|-----|
| 3.3.5 | Truncation of Phase Matrix | 62 |
| 3.4 | The Atmosphere-Surface System | 64 |
| 3.4.1 | BRDF Models | 65 |
| 3.4.2 | Implementing Surface BRDFs in Adding-Doubling | 70 |
| 3.4.3 | Validation of the Adding-Doubling Code | 72 |
| 3.5 | A Fast Algorithm Based on Icosahedral Grid | 75 |
| 3.6 | Summary | 78 |
| 4. | RETRIEVAL OF NON-SPHERICAL DUST AEROSOL PROPERTIES USING COLLOCATED POLDER/PARASOL-MODIS/AQUA MEASURE- MENTS | 81 |
| 4.1 | Introduction | 81 |
| 4.2 | Detection of Dusty Pixels with MODIS/Aqua | 83 |
| 4.3 | Sensitivity of Multi-Angular Radiance and Polarized Measurements of POLDER/PARASOL | 86 |
| 4.4 | The Aerosol Retrieval Algorithm | 89 |
| 4.4.1 | Scattering and Absorption of Atmospheric Molecules | 89 |
| 4.4.2 | The Levenberg-Marquardt Method | 94 |
| 4.4.3 | A Description of the New Aerosol Retrieval Algorithm | 96 |
| 4.4.4 | Test of the Aerosol Retrieval Algorithm | 97 |
| 4.4.5 | Results | 99 |
| 4.5 | Summary | 104 |
| 5. | SUMMARY AND FUTURE WORK | 106 |
| | REFERENCES | 109 |

LIST OF FIGURES

| FIGURE | Page |
|---|------|
| 1.1 Schematic diagram showing direct and indirect effects of atmospheric aerosols. | 2 |
| 1.2 Saharan dust aerosols were blown away from the west coast of Africa, traveling over the Atlantic Ocean and reaching the east coast of South America as is observed by the MODIS/Aqua on March 10, 2012. . . . | 3 |
| 2.1 SEM images of aerosol samples ([53]). From top-left to bottom-right: (a) feldspar, (b) loess, (c) volcanic ash, (d) quartz, (e) red clay, (f) Saharan dust. | 10 |
| 2.2 Size distribution of the Sahara dust sample versus $\log r$, where the radius r is in μm . V, S, and N denote volume size distribution, surface area size distribution, and number size distribution, respectively ([53]). | 10 |
| 2.3 Phase matrix of the Sahara sand sample measured with the Helium-Chromium laser at wavelength 441.6 nm ([53]). | 11 |
| 2.4 Comparison between the analytical result, the results of the spheroidal functions imbedded in the Wolfram Mathematica and the new method for regular parameters ($n = 10, m = 5, c = 5\pi$). The top panel shows the perfectly matched Wronskian for the three methods. The following three plots on the left column show the spheroidal angle function, the radial functions of the first kind and the second kind calculated by the Mathematica and our new method. The other three plots on the right column show the corresponding derivatives of the spheroidal functions. | 34 |

| | | |
|-----|---|----|
| 2.5 | Comparison between the analytical result, the results of the spheroidal functions imbedded in the Wolfram Mathematica and the new method for extreme parameters ($n = 100, m = 50, c = 5\pi$). The top panel shows the perfectly matched Wronskian for the analytical method and our new method only, since the Mathematica failed to converge for such large parameters. The following three plots on the left column show the spheroidal angle function, the radial functions of the first kind and the second kind calculated by the Mathematica and our new method. The other three plots on the right column show the corresponding derivatives of the spheroidal functions. In fact, the Mathematica provided completely wrong results for the radial function of the first kind and kept running without providing any result for the radial function of the second kind. | 35 |
| 2.6 | Real part and imaginary part of the complex refractive index of Saharan dust aerosol, and the response functions of the POLDER/PARASOL spectral bands 490P, 670P, and 865P versus wavelength. The refractive index data are taken from [49]. | 39 |
| 2.7 | Comparison of elements P_{11} and P_{12} of the phase matrix of polydispersed spheroidal dust aerosols with aspect ratio ranged from 1.0 to 2.5 and mean radius ranged from 0.02 to 20.0 μm for the POLDER/PARASOL spectral bands 490P, 670P, and 865P. On the right column, the three panels are showing P_{11} s as functions of the scattering angle, the aspect ratio and the mean radius, for 490P, 670P, and 865P bands from top to bottom, respectively. On the left column, the three panels are showing $-P_{12}/P_{11}$ s as functions of the scattering angle, the aspect ratio and the mean radius, for 490P, 670P, and 865P bands from top to bottom, respectively. For each subgraph of the P_{11} , there are 5 slices at scattering angles of $60^\circ, 90^\circ, 120^\circ, 150^\circ, 180^\circ$. For each subgraph of the $-P_{12}/P_{11}$, there are 6 slices at scattering angles of $30^\circ, 60^\circ, 90^\circ, 120^\circ, 150^\circ, 180^\circ$ | 41 |
| 3.1 | Schematic diagram of the forward model. | 43 |
| 3.2 | Comparison of the computational time versus the number of used Gaussian division points between Chowdhary's code and the new code to reach the same precision (e.g. 10^{-6}) on the same computer. The model considered here is a three-layer atmosphere composed of atmospheric molecules and coarse mode dust aerosols. | 60 |

| | | |
|-----|---|----|
| 3.3 | Comparison of the Stokes vectors (I,Q,U,V) of upward radiances at the TOA calculated by our new adding-doubling code, the RayXP, and the Monte-Carlo method. The model here is a bi-layer atmosphere of fine mode dust aerosols with the total aerosol optical depth equal to 1.0 above a Lambertian surface with the surface albedo 0.8. The solar zenith angle is 60° . The Stokes vectors in three meridian planes at azimuthal angles equal to 0° , 90° , and 180° are plotted. | 73 |
| 3.4 | Comparison of the Stokes vectors (I,Q,U,V) of upward radiances at the TOA calculated by our new adding-doubling code, the RayXP, and the Monte-Carlo method. The model here is a bi-layer atmosphere of coarse mode dust aerosols with the total aerosol optical depth equal to 1.0 above a Lambertian surface with the surface albedo 0.8. The solar zenith angle is 60° . The Stokes vectors in three meridian planes at azimuthal angles equal to 0° , 90° , and 180° are plotted. | 74 |
| 3.5 | Comparison of the Stokes vectors (I,Q,U,V) of upward radiances at the TOA calculated by our new adding-doubling code and the RayXP. The model here is a thin Rayleigh layer with the optical depth equal to 0.1 above a windy-ruffled ocean surface with the wind speed at ocean surface equal to $10.0m/s$. The solar zenith angle is 60° . The Stokes vectors in three meridian planes at azimuthal angles equal to 0° , 90° , and 180° are plotted. | 75 |
| 3.6 | Icosahedral grid of level 2 consisting of 40 triangular faces on the left and icosahedral grid of level 4 consisting of 160 triangular faces on the right. | 76 |
| 3.7 | Comparison of the Stokes vectors (I,Q,U,V) of upward radiances at the TOA calculated by the fast model and the rigorous adding-doubling method. The model here is a thin dust aerosol layer above a black surface. The solar zenith angle is 60° and the relative azimuthal angle is 0° | 79 |
| 4.1 | Comparison between the MODIS RGB image (left panel) and the result of dusty pixel detection (right panel) for the west coast area of North Africa on April 1, 2010. The white gap in the right panel is due to the sun glint. | 84 |
| 4.2 | Comparison between the MODIS RGB image (left panel) and aerosol optical depth derived in the MODIS Deep Blue product (right panel) over the Sahara Desert on April 1, 2010. | 85 |

| | | |
|------|--|----|
| 4.3 | Comparison between simulations of normalized radiance using the spherical model and the spheroidal model with the aspect ratio 2.5. The contour is obtained from the actual measurements from the POLDER/PARASOL over global ocean on April 1, 2010, with the value defined as the number of observations at the particular scattering angle and with the particular value of normalized radiance divided by the total number of observations at the particular scattering angle. | 87 |
| 4.4 | Comparison between simulations of normalized polarized radiance using the spherical model and the spheroidal model with the aspect ratio 2.5. The contour is obtained from the actual measurements from the POLDER/PARASOL over global ocean on April 1, 2010 with the value defined as the number of observations at the particular scattering angle and with the particular value of normalized polarized radiance divided by the total number of observations at the particular scattering angle. | 88 |
| 4.5 | Angular dependence of normalized radiances measured by the POLDER/PARASOL over the Sahara Desert on April 1, 2010. | 89 |
| 4.6 | Comparison between simulations of normalized polarized radiance using spheroidal models with the aspect ratios 1.0,1.25, and 2.5. The contour is obtained from the actual measurements of the POLDER/PARASOL over the Sahara Desert on April 1, 2010. | 90 |
| 4.7 | Comparison between simulations of normalized polarized radiance using the optical depths 0.5 and 2.0. The spheroidal models of dust aerosol with the aspect ratio 2.5 is adopted in these calculations. The contour is obtained from the actual measurements of the POLDER/PARASOL over the Sahara Desert on April 1, 2010. | 91 |
| 4.8 | Comparison between simulations of normalized polarized radiance using the actual surface albedos and the doubled surface albedos. The spheroidal models of dust aerosol with the aspect ratio 2.5 is adopted in these calculations. The contour is obtained from the actual measurements of the POLDER/PARASOL over the Sahara Desert on April 1, 2010. | 92 |
| 4.9 | High-spectral-resolution optical depth of the Rayleigh scattering and molecule absorption around the channel 490P (top) and the channel 670P (bottom). | 93 |
| 4.10 | Flow chart of the new retrieval algorithm for non-spherical dust aerosols. | 98 |

| | | |
|------|---|-----|
| 4.11 | Histograms of the retrieved mean radius of the coarse mode dust aerosols, mean radius of the fine mode dust aerosols, aspect ratio, and single-scattering albedo. | 101 |
| 4.12 | Angular variation of the relative errors of radiance, for example, $(I_{\text{simulation}} - I_{\text{measurement}})/I_{\text{measurement}}$ | 102 |
| 4.13 | Angular variation of the errors of DoLP, for example, $DoLP_{\text{simulation}} - DoLP_{\text{measurement}}$ | 103 |
| 4.14 | Comparison of surface reflectance and aerosol optical depth retrieved by MODIS Deep Blue algorithm and our new retrieval algorithm. . . | 104 |

LIST OF TABLES

| TABLE | Page |
|--|------|
| 2.1 Ranges of microphysical properties. | 36 |
| 4.1 Technical features of POLDER/PARASOL and MODIS/Aqua. | 81 |
| 4.2 Test of new retrieval algorithm. | 99 |

1. INTRODUCTION

Aerosol refers to a dispersion of solid and liquid particles suspended in a gas. The earth's atmosphere contains aerosols of various types, such as dust, smoke, sea salt, soot, pollen, spores, bacteria, etc. As is shown in Figure 1.1, atmospheric aerosols can impact the earth radiation budget and climate through their direct and indirect effects ([18]). Scattering the shortwave solar radiation and absorbing the long-wave thermal radiation, atmospheric aerosols directly modify the energy budget of the earth ([46]); Acting as the CCN (Cloud Condensation Nuclei), atmospheric aerosols increase the number concentration and the lifetime, but reduce the size of cloud particles, through which they affect the climate and hydrological cycle indirectly ([40]). Due to chemical, microphysical, spatial and temporal variability of aerosols, the total radiative effect remains uncertain both in magnitude and even in sign, with an estimated uncertainty on the order of $2W \cdot m^{-2}$ which is comparable to the radiative forcing of well-mixed greenhouse gases ([42], [18]). Therefore, accurate characterization of aerosol is considered as a major challenge in the atmospheric science. Mineral dust aerosol, originating in desert and semi-arid areas, is one of the largest contributors to the mass loading of atmospheric aerosols. The major source of natural dusts in the world is the Sahara Desert, where the dusts are uplifted by convections over hot desert areas and reach the top of the troposphere ([48]). These dusts can spread across the Mediterranean ocean and the Atlantic ocean, and travel thousands of kilometers to Europe and South America by large-scale atmospheric circulations (see Figure 1.2). Another important source of dust aerosols is the Gobi Desert, which may affect eastern Asia and even western North America. Through the long-range transportation, dust aerosols are present worldwide and influence not

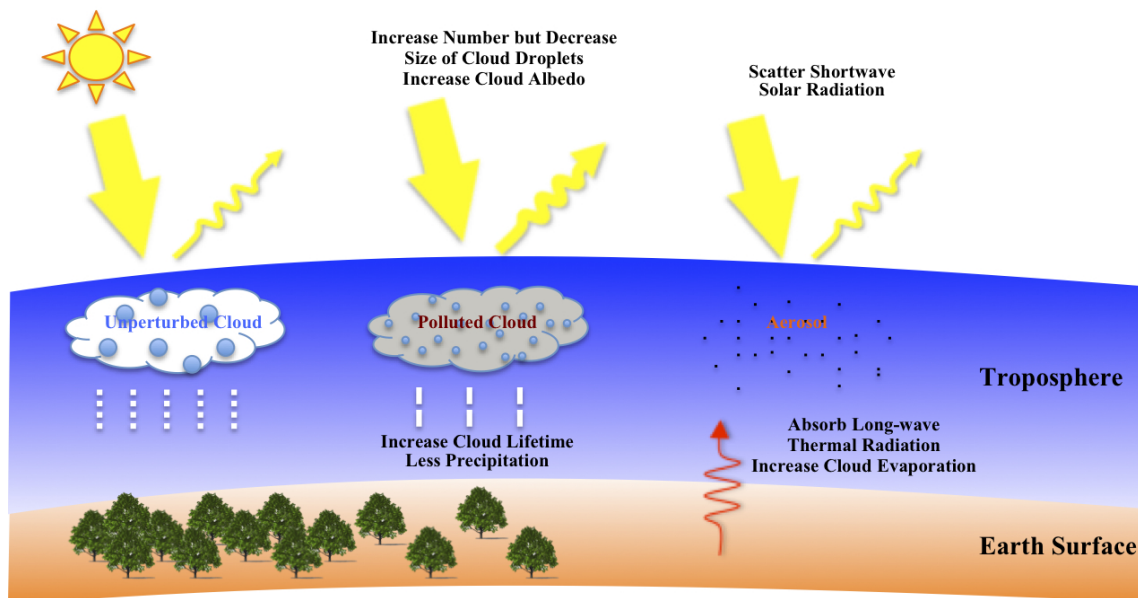


Figure 1.1: Schematic diagram showing direct and indirect effects of atmospheric aerosols.

only the local but also the global climate. During the transport process, dust aerosols may undergo significant changes in concentration, particle size distribution, particle shape and chemical composition, which result in the difficulty to evaluate the total radiative effect on the climate forcing ([50], [26]). Thus, estimation of the radiative forcing of dust aerosols requires globally resolving the spatial and temporal configuration of these parameters. A promising way to retrieve dust aerosol parameters on the global scale is by space-borne satellite observations. Satellite instruments that are currently used for the operational remote sensing of aerosols can be divided into the following four categories ([25]): (a) multispectral single-viewing-directional radiometer, such as the MODIS (MODerate resolution Imaging Spectro-radiometer); (b) multispectral multi-viewing-directional radiometer, such as the MISR (Multi-angle Imaging Spectro-Radiometer); (c) multispectral single-viewing-directional radiometer and polarimeter, such as the GOME-2 (Global Ozone Monitoring Experiment-2);

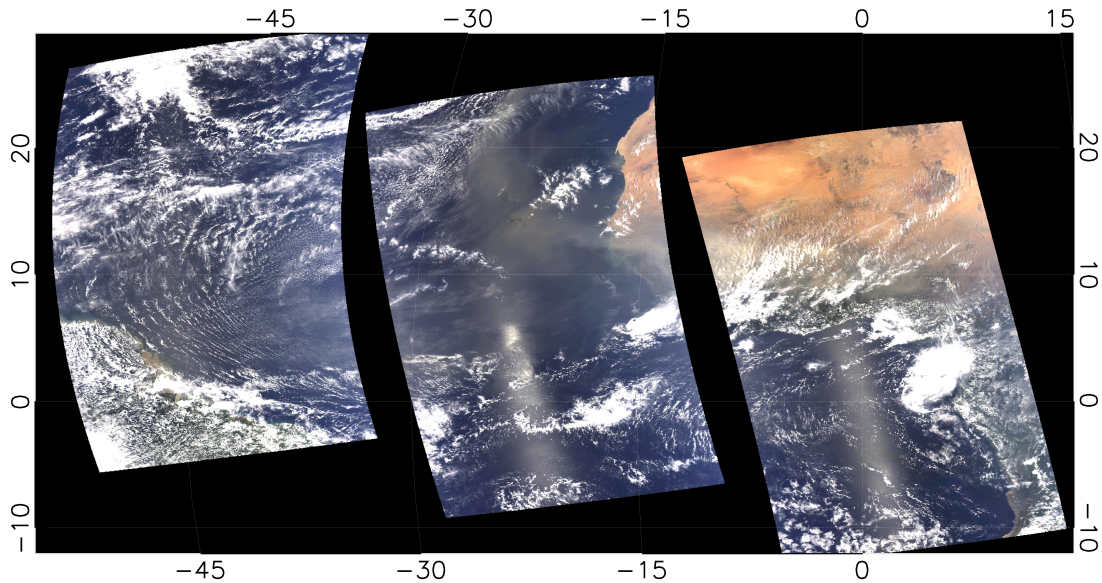


Figure 1.2: Saharan dust aerosols were blown away from the west coast of Africa, traveling over the Atlantic Ocean and reaching the east coast of South America as is observed by the MODIS/Aqua on March 10, 2012.

(d) multispectral multi-viewing-directional radiometer and polarimeter, such as the POLDER (POLarization and Directionality of the Earth's Reflectances).

Two MODISs were launched successively in December 1999 and May 2002 on-board NASA's (National Aeronautics and Space Administration) Terra and Aqua satellites. Both of the MODISs have 36 channels spanning a wide spectral range from 0.41 to 15 μm with various resolutions from 250 m to 1 km. There are two entirely independent algorithms to retrieve dust aerosol parameters over dark surfaces and over bright surfaces for the MODISs. The dark land algorithm, also known as the dark target approach, is applicable only when the surface albedo is smaller than 0.25 at the 2.13 μm band ([41]). In this algorithm, the surface albedo for the 2.13 μm band, where the atmosphere is nearly transparent, is obtained first and then the surface albedos at the visible spectrum are derived based on an empirical relationship. The estimated surface albedos and the measured reflectances are then

input into a LUT (Look-Up-Table) to retrieve dust aerosol optical thicknesses at the 0.47 and 0.66 μm bands. To fill in data gaps of the dark target approach, the Deep Blue algorithm is developed for dust aerosol retrieval over bright surfaces, particularly over desert regions ([21]). At the blue channels, the surface contributions to the reflectances at the TOA (Top Of Atmosphere) are relatively low, which allows for more contrast to separate the dust signals. Before the retrieval process, a land surface reflectivity database is generated using the minimum reflectivity technique, by which the seasonal and regional land surface reflectivity can be determined ([21]). Dust aerosol parameters are then obtained by searching a LUT generated by an empirical dust model and using the maximum likelihood method.

Also onboard the Terra platform, the MISR is viewing the earth at four spectral bands (446, 558, 672 and 866 nm) and nine fixed viewing zenith angles (0° , $\pm 26.1^\circ$, $\pm 45.6^\circ$, $\pm 60.0^\circ$ and $\pm 70.5^\circ$) in the along-track direction with the cross-track ground spatial resolution of 275 m or 1.1 km. The MISR dust aerosol retrieval algorithm is based on a principal component analysis of spatial contrasts of the multispectral and multi-angle measurements, from which EOFs (Empirical Orthogonal Functions) in every view zenith angles are derived to describe the directional surface reflectivities ([31]). The atmospheric path radiances at different optical depths are pre-computed for 74 aerosol models and stored in the SMART (Simulated MISR Ancillary Radiative Transfer) dataset. During the retrieval process, each model with certain optical depth is tested by checking a fit function. Any aerosol model with the corresponding optical depth that passes a minimum criterion is considered to be a successful retrieval.

Despite the success in retrieving the dust aerosol optical depth and particle size, satellite remote sensing of dust aerosols based on radiance measurements alone encounters severe non-uniqueness problem when more aerosol information is involved ([35]). Within the instrumental error, the optimal estimation cannot determine which

aerosol model is the best fit to the measurements among those with different optical thicknesses, refractive indices, effective radii and shapes, especially for aerosol retrieval over a bright land surface. Even with constraints from multi-angular radiance measurements, it is still not sufficient to find a unique solution with a high enough accuracy. However, it is suggested that the combined multi-angular polarization and radiance measurements are able to provide aerosol properties with an accuracy needed for a long-term global climate research, even when the surface properties are unknown ([17]). The reason is that light scattered by atmospheric molecules and dust aerosols are strongly polarized and the angular features are sensitive to the microphysical properties, while light scattered by surfaces are weakly polarized and spectrally gray in visible spectral range ([25]). Thus, the comprehensive multi-spectral multi-angular radiance and polarized measurements provide an unprecedented opportunity to investigate the dust aerosol properties over land.

Launched in December 2004 by the CNES (French Space Agency), the POLDER, onboard the PARASOL (Polarization and Anisotropy of Reflectances for Atmospheric Sciences coupled with Observations from a Lidar), is the only instrument in orbit that provides radiance measurements at nine bands (443, 490, 565, 670, 763, 765, 865, 910 and 1020 nm) and linear polarization at three bands (490, 670 and 865 nm) in up to 16 directions per pixel with a moderate nadir resolution of $6 \text{ km} \times 7 \text{ km}$. The scheme of aerosol retrieval is based on the polarized measurements at the 670 nm or 865 nm bands only, where the polarized light reflected by ground targets is small as is suggested by the ground-based measurements ([8]). Due to the large uncertainties introduced by the low spatial resolution, the polarized measurements are modeled only to the first order by considering the direct reflection of the surface, the single scattering of aerosols and atmospheric molecules. The surface BPDF (Bidirectional Polarization Distribution Function) is approximately calculated

through a semi-empirical model developed by Nadal and Bréon ([38]). Aerosols are assumed to be non-absorbing spherical particles with mono-modal size distributions. The Angstrom exponent and the optical depth are retrieved with the corresponding aerosol model that gives the minimum residual error.

Even though the POLDER/PARASOL has been in orbit for a decade, the development of an inversion scheme, which is capable of an efficient and accurate retrieval of more aerosol parameters that people are interested in, is still an ongoing research task. In the current operational POLDER/PARASOL aerosol retrieval algorithm over land, the following issues are recognized: (a) Over dust aerosol source regions or in a dust storm season, the multiple scattering effect of aerosols may not be ignored; (b) Based on the polarized measurements only, this algorithm lost valuable information of the surface BRDF; (c) The precision of the obtained aerosol characteristics are limited by the semi-empirical surface BPDF model, which introduces more significant error as wavelength becomes shorter or aerosol loading becomes larger; (d) The single-scattering models of dust aerosols are oversimplified by assuming the spherical shape and omitting the imaginary part of the refractive index, which may lead to misinterpretation of the measurements and substantial errors in the retrieved aerosol parameters; (e) Depending significantly on the selection of the limited number of fixed dust aerosol models, the retrieval quality may vary for different seasons and regions, and no continuous aerosol properties can be retrieved.

In this work, we retrieved the dust aerosol properties, including aerosol optical thickness, fine mode mean radius, coarse mode mean radius, aerosol layer height and aerosol aspect ratio, over land with satellite observations, especially over the most challenging dust aerosol source regions. Considering the limitation of the low spatial resolution and narrow spectral range of the POLDER/PARASOL, we used the collocated MODIS/Aqua and POLDER/PARASOL data. In order to make full

use of the capability of multi-spectral multi-angular radiance and polarized measurements, all the available components of Stokes vector (I, Q, U) will be considered in the retrieval process. The aerosol model and Surface BRDF model have also been improved by incorporating a newly developed single-scattering property database of non-spherical dust aerosols and a surface BRDF library, respectively. The traditional LUT based retrieval algorithm has been abandoned and substituted by a new iterative method, which allows for obtaining aerosol parameters as well as surface parameters simultaneously and continuously.

The remaining content of this dissertation is organized as follows: In Section 2, we introduce the numerical simulation for the single-scattering properties of non-spherical dust aerosols. Concepts of light scattering are first given. Specially, we use spheroidal models to account for the non-sphericity of dust aerosols and develop a new algorithm for the computation of spheroidal angle and radial functions as well as their first order derivatives. A newly developed single-scattering property database and the calculation of narrowband bulk scattering properties of dust aerosols that will be used in the following retrieval process is also introduced. In Section 3, the forward model for simulation of radiometric and polarimetric measurements of satellite is discussed. With the adding-doubling technique, we develop an efficient code to solve the VRTE (vector radiative transfer equation) for polarized light propagation in the plane-parallel atmosphere-surface system. The numerical techniques that have been implemented in the code to achieve the high efficiency are also reviewed. Moreover, we introduce a surface BRDF library imbedded in the code to simulate reflection properties of various land and ocean surfaces. In order to further accelerate the code when a moderate precision is acceptable, a fast algorithm based on an icosahedral grid is discussed. In Section 4, we introduce the aerosol retrieval algorithm for non-spherical dust aerosols over land using the col-

located measurements from the MODIS/Aqua and the POLDER/PARASOL. The absorption and Rayleigh scattering of atmospheric molecules are taken into account through the LBLRTM (Line-By-Line Radiative Transfer Model). Instead of using the traditional LUT technique, we introduce an iterative method, which is based on the Levenber-Marquardt method, to solve the nonlinear inverse problem numerically. An application of the retrieval algorithm for the dust aerosol properties over the Sahara Desert is presented at the end. In the last fifth Section, we make a brief summarization and propose some interesting projects that may be considered in the future studies.

2. SINGLE-SCATTERING PROPERTIES OF NON-SPHERICAL DUST AEROSOLS

2.1 Introduction*

As the basis of aerosol remote sensing, light scattering properties of dust aerosols must be known first ([28]). In laboratory studies ([53]), SEM (Scanning Electron Microscope) images have shown that dust aerosols are usually irregular in shape (see Figure 2.1). The particle size of dust aerosols may range from sub-micron to tens of microns and the particle size distribution is approximately in a bi-modal log-normal form (Figure 2.2). By measuring the absorption of dust aerosols, the imaginary part of refractive index can be obtained ([39]). The real part of the refractive index can then be derived through the Kramers-Kronig relations ([45]). In the visible spectral range, the real part of the refractive index is around 1.5 and the particle is almost non-absorbing (see Figure 2.6). However, limited by the experimental technique, the scattering cross-sections and phase matrices of dust aerosols could only be measured at a few fixed wavelengths and in a limited angle range, where the most important forward and backward scattering features are lost (see Figure 2.3). Numerical simulations provide an alternative way to obtain the knowledge of these optical properties. The theory of electromagnetic wave scattering has been well established ([51]). Many computational methods have been developed for specific scattering problems, such as the Lorenz-Mie theory ([3]), the T-matrix method ([33]), the DDA (Discrete Dipole Approximation, [61]), the FDTD (Finite Difference Time Domain method, [58]), the PSTD (Pseudo-Spectral Time Domain Method, [30]), the

*Figures 2.1, 2.2, and 2.3, are reprinted with permission from “Scattering matrices of mineral aerosol particles at 441.6 nm and 632.8 nm,” *Journal of Geophysical Research-Atmospheres* **106**, 17375-17401, Copyright 2001 by John Wiley and Sons.

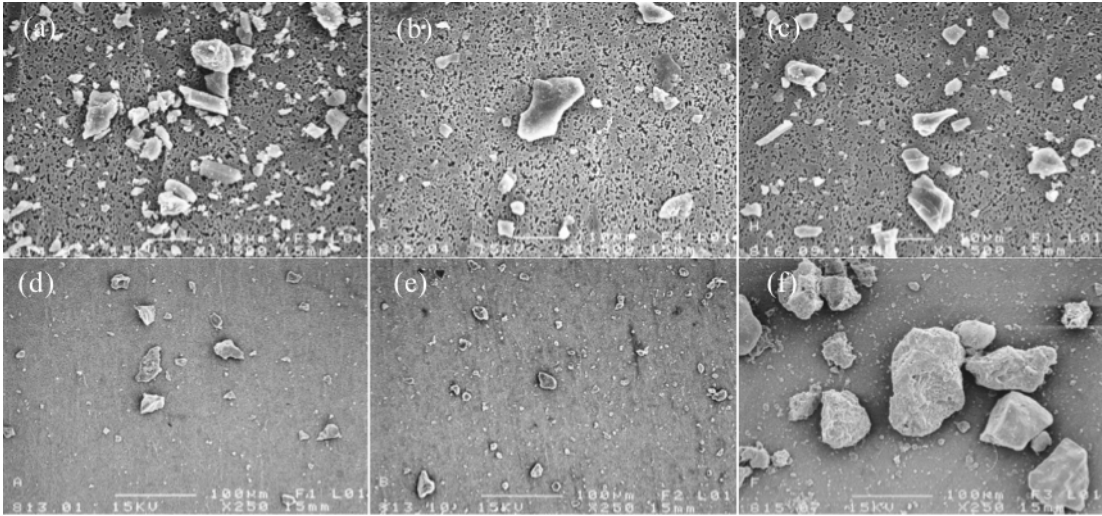


Figure 2.1: SEM images of aerosol samples ([53]). From top-left to bottom-right: (a) feldspar, (b) loess, (c) volcanic ash, (d) quartz, (e) red clay, (f) Saharan dust.

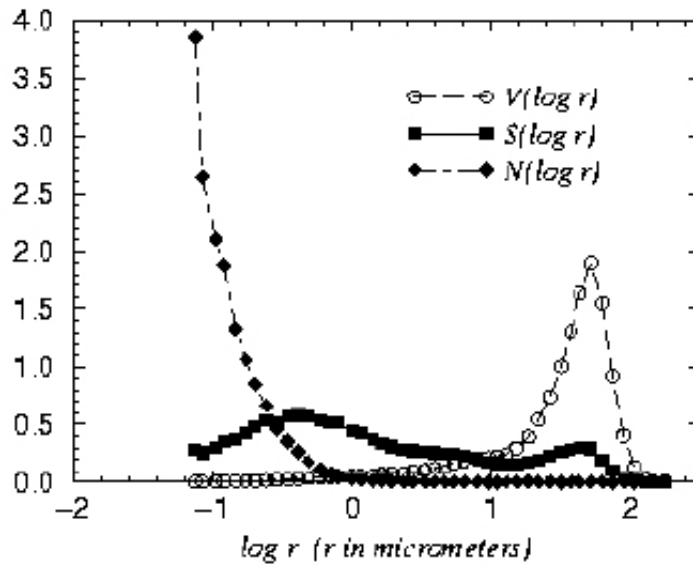


Figure 2.2: Size distribution of the Sahara dust sample versus $\log r$, where the radius r is in μm . V , S , and N denote volume size distribution, surface area size distribution, and number size distribution, respectively ([53]).

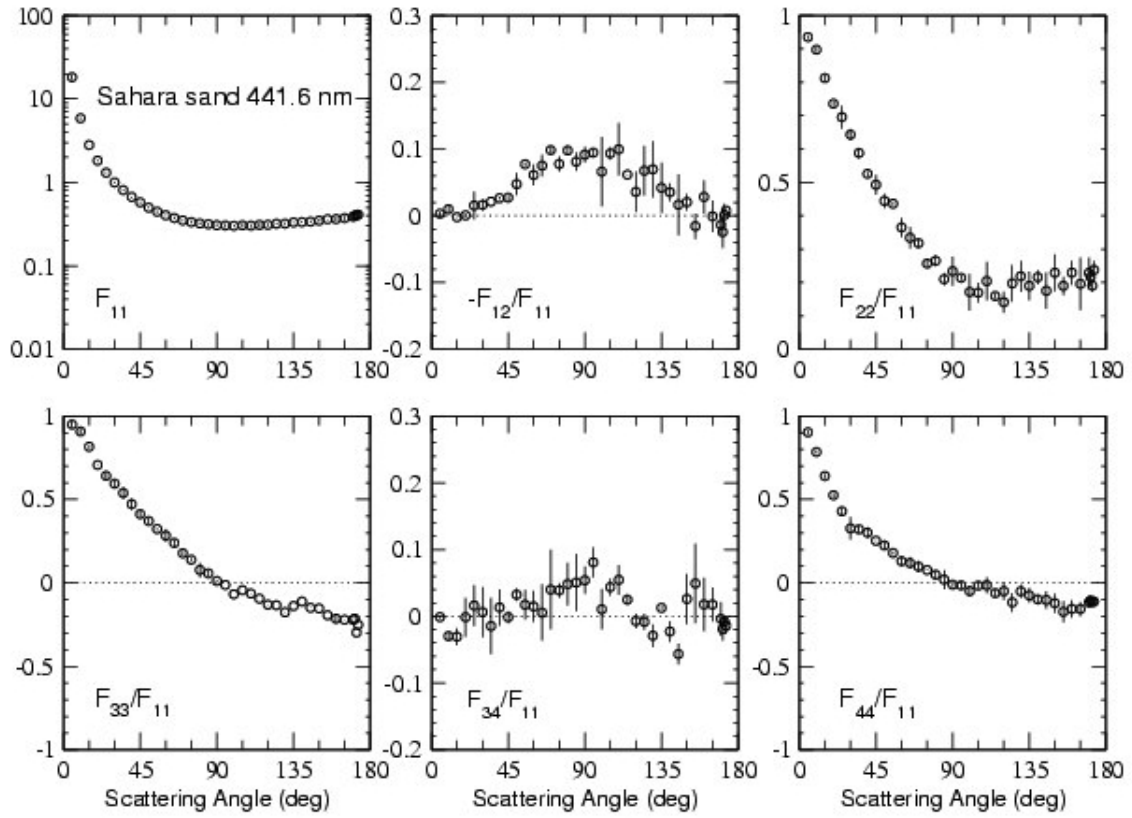


Figure 2.3: Phase matrix of the Sahara sand sample measured with the Helium-Chromium laser at wavelength 441.6 nm ([53]).

IGOM (Improved Geometric Optics Method, [57]), the Rayleigh-Gans approximation ([3]), and the ADT (Anomalous Diffraction Theory, [59]). The Lorenz-Mie theory solves the scattering of a single spherical particle analytically, whose results are usually considered as the benchmark for other methods because of its efficiency and accuracy. Spherical models have been widely used in modeling of various particles in the atmospheric science. However, it has been shown that using the spherical model for irregularly shaped dust aerosols may introduce significant error in the radiative transfer simulation ([60]). Therefore, it is preferred to find a non-spherical dust aerosol model, which is able to be computed with existing methods, to take into account the non-sphericity effect. As approximated methods, the IGOM, the Rayleigh-Gans approximation, and the ADT have their own feasible scopes. For example, the IGOM requires that the size parameter of the particle is larger than 30 ([2]); the Rayleigh-Gans approximation is only valid for small soft particles (refractive index is close to 1, [3]); the ADT may fail if the particle is not large or soft enough ([59]). Considering the fact that the refractive index of dust aerosols is relative large and the size parameter may range from several hundredths to several hundreds in the visible spectrum, these approximated methods may not be appropriate for light scattering simulations of dust aerosols in a general case. On the other hand, numerical methods, including of the DDA, the FDTD, and the PSTD, can be applied to any sized particle in arbitrary shapes, theoretically. Nevertheless, due to the limitation of computation resources, they are seldom used to calculate particles with a size parameter larger than 50 even through parallel computation using a super computer nowadays. As a semi-analytical method, the T-matrix method can roughly cover the size parameter range of dust aerosols in the visible spectrum. Since the T-matrix method is only efficient for particles with the revolution symmetry, the spheroidal model, along with a parameter aspect ratio that is defined as the rotational

symmetric axis (or the polar axis) over the equatorial diameter, has been introduced to model non-spherical dust aerosols ([9]).

Unfortunately, in spite of the success of the T-matrix method for small near-sphere particles, T-matrix method can hardly converge to the correct solution when the aspect ratio becomes larger than 4 or the size parameter exceeds 150 even with the extended precision ([34]). The reason is that most T-matrix codes are implemented in spherical coordinates, which may not fit into the symmetry of the scattering problem. The SVM (Separation of Variables Method) in spheroidal coordinates has already been applied to simulate light scattering of a single spheroidal particle with an extreme high aspect ratio ([12]). It was found that spheroidal coordinates are more suitable for the symmetry of the scattering problem. A semi-analytical T-matrix method in spheroidal coordinates has also been developed ([43]). However, one thing that is limiting the development of solving scattering problems in spheroidal coordinates is that no efficient computation codes of spheroidal functions are available. Therefore, it is worthy to make the effort to develop a new algorithm for spheroidal functions.

Alternatively, it is also possible to use a combination of the available methods and take advantage of the complimentary feasible scopes to cover the whole interested parameter ranges of spheroids. Following this idea, a new database of single-scattering properties of tri-axial ellipsoidal mineral dust aerosols has been developed recently ([32]). By implementing a kernel method ([52]), the database allows for an efficient derivation of the bulk optical properties for a given distribution of particle micro-physical parameters (i.e., refractive index, size parameter and aspect ratio). We adopt the database in our following radiative transfer calculations.

The remaining part of this section is organized as follows: In Subsection 2.2, we review the fundamental theory of electromagnetic scattering by a single particle,

where some concepts and definitions that will be used in the following sections are given. In the third subsection, a new algorithm to calculate the spheroidal functions is introduced. The database of single-scattering properties of tri-axial ellipsoidal mineral dust aerosols is presented in Subsection 2.4. In the fifth subsection, the narrowband bulk scattering properties of dust aerosols for the satellite remote sensing are discussed. A summary of this section is given in the last subsection.

2.2 Fundamental Theory of Single Electromagnetic Scattering

The general light scattering problem of dust aerosols cannot be fully covered in this section, we limit our treatment to the single-scattering of electromagnetic wave. The first assumption here is that particles are widely separated and randomly positioned, so that each particle scatters light independently as if all other particles do not exist, and there are no systematic phase relations between electromagnetic waves scattered by different particles (which means the Stokes vectors of the partial electromagnetic waves can be added incoherently). Second, only the scattering in the far-field region will be considered, where the propagation of the scattered wave is away from the particle, and the scattered field is polarized transverse to the propagation direction and decays inversely with distance from the particles. Third, the scattering is assumed to be elastic so that the scattered light has the same frequency as the incident light. This excludes quantum phenomena such as the Raman scattering or the fluorescence. Fourth, we will consider only time-harmonic monochromatic light by assuming that the complex amplitude of the electric field fluctuates with a frequency much smaller than the frequency in the time factor $\exp(-i\omega t)$. In other words, we will consider only scattering by individual particles within the framework of the Maxwell's equations and linear optics.

The Maxwell equations form the theoretical basis of light scattering problems. In

SI units, the set of the four Maxwell equations is given by

$$\nabla \cdot \mathbf{D}(\mathbf{r}, t) = \rho(\mathbf{r}, t), \quad (2.1)$$

$$\nabla \cdot \mathbf{B}(\mathbf{r}, t) = 0, \quad (2.2)$$

$$\nabla \times \mathbf{E}(\mathbf{r}, t) = -\frac{\partial \mathbf{B}(\mathbf{r}, t)}{\partial t}, \quad (2.3)$$

$$\nabla \times \mathbf{H}(\mathbf{r}, t) = \mathbf{J}(\mathbf{r}, t) + \frac{\partial \mathbf{D}(\mathbf{r}, t)}{\partial t}, \quad (2.4)$$

where \mathbf{D} is the electric displacement, \mathbf{B} is the magnetic induction, \mathbf{E} is the electric field, \mathbf{H} is the magnetic field, and ρ and \mathbf{J} are the macroscopic free charge and current density, respectively.

The vector fields \mathbf{D} , \mathbf{B} , \mathbf{E} , \mathbf{H} in equations (2.1)-(2.4) are related by

$$\mathbf{D}(\mathbf{r}, t) = \epsilon_0 \mathbf{E}(\mathbf{r}, t) + \mathbf{P}(\mathbf{r}, t), \quad (2.5)$$

$$\mathbf{H}(\mathbf{r}, t) = \frac{1}{\mu_0} \mathbf{B}(\mathbf{r}, t) - \mathbf{M}(\mathbf{r}, t), \quad (2.6)$$

where \mathbf{P} is the electric polarization (average electric dipole moment per unit volume) \mathbf{M} is the magnetization (average magnetic dipole moment per unit volume), and ϵ_0 and μ_0 are the electric permittivity and the magnetic permeability of free space, respectively.

To uniquely determine the electric and magnetic fields, equations (2.1)-(2.6) must be supplemented with the so-called constitutive relations:

$$\mathbf{P}(\mathbf{r}, t) = \epsilon_0 \chi(\mathbf{r}) \mathbf{E}(\mathbf{r}, t), \quad (2.7)$$

$$\mathbf{B}(\mathbf{r}, t) = \mu(\mathbf{r}) \mathbf{H}(\mathbf{r}, t), \quad (2.8)$$

$$\mathbf{J}(\mathbf{r}, t) = \sigma(\mathbf{r}) \mathbf{E}(\mathbf{r}, t), \quad (2.9)$$

where χ is the electric susceptibility, μ is the magnetic permeability and σ is the conductivity. Define electric permittivity as

$$\epsilon(\mathbf{r}) = \epsilon_0[1 + \chi(\mathbf{r})] \quad (2.10)$$

so that

$$\mathbf{D}(\mathbf{r}, t) = \epsilon(\mathbf{r})\mathbf{E}(\mathbf{r}, t). \quad (2.11)$$

For linear and isotropic media, χ , μ , σ , and ϵ are scalars independent of the fields.

The Maxwell equations in the differential form (e.g., equations (2.1)-(2.4)) are strictly valid only when constitutive parameters χ , μ , and σ vary continuously. Across the medium interface where constitutive parameters change abruptly, the boundary conditions can be derived from the Maxwell equations in the integral form. The resulting relations for the fields of medium 1 and medium 2 at the interface are

$$\hat{\mathbf{n}} \cdot (\mathbf{B}_2 - \mathbf{B}_1) = 0, \quad (2.12)$$

$$\hat{\mathbf{n}} \cdot (\mathbf{D}_2 - \mathbf{D}_1) = \rho_s, \quad (2.13)$$

$$\hat{\mathbf{n}} \times (\mathbf{E}_2 - \mathbf{E}_1) = 0, \quad (2.14)$$

$$\hat{\mathbf{n}} \times (\mathbf{H}_2 - \mathbf{H}_1) = \mathbf{J}_s. \quad (2.15)$$

where $\hat{\mathbf{n}}$ is a unit vector in the local normal direction to the interface, pointing from medium 1 toward medium 2, ρ_s is the surface charge density, and \mathbf{J}_s is the surface current density.

Assume that all fields and sources are monochromatic. It is possible to represent the real monochromatic fields with the time-independent components of the complex

fields and the time factor $\exp(-i\omega t)$, e.g.,

$$\mathbf{E}(\mathbf{r}, t) = \frac{1}{2}[\mathbf{E}(\mathbf{r}) \exp(-i\omega t) + \mathbf{E}^*(\mathbf{r}) \exp(i\omega t)]. \quad (2.16)$$

Then equations (2.1)-(2.4) yield the following frequency-domain Maxwell equation for the time-independent components of the complex fields:

$$\nabla \cdot [\varepsilon(\mathbf{r}, \omega) \mathbf{E}(\mathbf{r})] = 0, \quad (2.17)$$

$$\nabla \cdot [\mu(\mathbf{r}, \omega) \mathbf{H}(\mathbf{r})] = 0, \quad (2.18)$$

$$\nabla \times \mathbf{E}(\mathbf{r}) = i\omega\mu(\mathbf{r}, \omega) \mathbf{H}(\mathbf{r}), \quad (2.19)$$

$$\nabla \times \mathbf{H}(\mathbf{r}) = -i\omega\varepsilon(\mathbf{r}, \omega) \mathbf{E}(\mathbf{r}), \quad (2.20)$$

where

$$\varepsilon(\mathbf{r}, \omega) = \epsilon(\mathbf{r}, \omega) + i \frac{\sigma(\mathbf{r}, \omega)}{\omega}. \quad (2.21)$$

is the so-called complex permittivity. Note that the constitutive parameters here are also functions of frequency ω if the medium is time-dispersive.

Now we consider the scattering of a monochromatic plane wave by a fixed homogeneous particle immersed in an infinite homogeneous and non-absorbing medium. The frequency-domain monochromatic Maxwell curl equations (2.19) and (2.20) can be written as

$$\left. \begin{aligned} \nabla \times \mathbf{E}(\mathbf{r}) &= i\omega\mu_1 \mathbf{H}(\mathbf{r}) \\ \nabla \times \mathbf{H}(\mathbf{r}) &= -i\omega\varepsilon_1 \mathbf{E}(\mathbf{r}) \end{aligned} \right\} \text{outside the particle,} \quad (2.22)$$

$$\left. \begin{aligned} \nabla \times \mathbf{E}(\mathbf{r}) &= i\omega\mu_2 \mathbf{H}(\mathbf{r}) \\ \nabla \times \mathbf{H}(\mathbf{r}) &= -i\omega\varepsilon_2 \mathbf{E}(\mathbf{r}) \end{aligned} \right\} \text{inside the particle.} \quad (2.23)$$

By assuming that the scattering particle and the host medium are nonmagnetic, i.e., $\mu_2 = \mu_1 = \mu_0$, where μ_0 is the permeability of a vacuum, the vector wave equations (or the vector Helmholtz equations) can be derived from equations (2.23) and (2.23):

$$\nabla^2 \mathbf{E}(\mathbf{r}) + k_1^2 \mathbf{E}(\mathbf{r}) = 0, \quad \text{inside the particle,} \quad (2.24)$$

$$\nabla^2 \mathbf{E}(\mathbf{r}) + k_2^2 \mathbf{E}(\mathbf{r}) = 0, \quad \text{outside the particle,} \quad (2.25)$$

where $k_1 = \omega(\varepsilon_1 \mu_0)^{1/2}$ and $k_2 = \omega(\varepsilon_2 \mu_0)^{1/2}$ are the wave numbers in the host medium and the scattering particle, respectively.

If the scattering particle is not present (e.g. $k_2 = k_1$), the incident plane electromagnetic wave

$$\mathbf{E}^{inc}(\mathbf{r}) = \mathbf{E}_0^{inc} \exp(ik_1 \hat{\mathbf{n}}^{inc} \cdot \mathbf{r}), \quad (2.26)$$

where $\hat{\mathbf{n}}^{inc} \cdot \mathbf{E}^{inc}(\mathbf{r}) = 0$, is just a solution to the equations (2.24) and (2.25); When the scattering particle is present, the scattered field is defined as the difference between the total field and the incident field, i.e.,

$$\mathbf{E}^{sca}(\mathbf{r}) = \mathbf{E}(\mathbf{r}) - \mathbf{E}^{inc}(\mathbf{r}). \quad (2.27)$$

Regarding the boundary conditions, equations (2.12)-(2.15) only require that the tangential components of the total field \mathbf{E} are continuous across the surface of the scattering particle. Moreover, at the infinity, the outgoing wave condition requires that

$$\lim_{r \rightarrow \infty} r \left(\frac{\partial \mathbf{E}^{sca}}{\partial r} - ik_1 \mathbf{E}^{sca} \right) = \mathbf{0}. \quad (2.28)$$

Define the dimensionless size parameter $x = k_1 a$ with a the radius of the cir-

cumsphere of the scattering particle. In the far-field region, where $k_1 r \gg 1$ and $k_1 r \gg x^2/2$, the scattered field \mathbf{E}^{sca} becomes spherical that decays inversely with distance r and is transversely polarized, i.e. $\hat{\mathbf{n}}^{sca} \cdot \mathbf{E}^{sca}(\mathbf{r}) = 0$. Since both of the incident and scattered fields are perpendicular to the propagation directions, we may decompose the fields as

$$\mathbf{E}^{inc}(\mathbf{r}) = E_{\parallel}^{inc}(r, \hat{\mathbf{n}}^{inc})\hat{\mathbf{e}}_{\parallel}^{inc} + E_{\perp}^{inc}(r, \hat{\mathbf{n}}^{inc})\hat{\mathbf{e}}_{\perp}^{inc}, \quad (2.29)$$

$$\mathbf{E}^{sca}(\mathbf{r}) = E_{\parallel}^{sca}(r, \hat{\mathbf{n}}^{sca})\hat{\mathbf{e}}_{\parallel}^{sca} + E_{\perp}^{sca}(r, \hat{\mathbf{n}}^{sca})\hat{\mathbf{e}}_{\perp}^{sca}, \quad (2.30)$$

where $\hat{\mathbf{e}}_{\perp}$ is a unit vector perpendicular to the scattering plane (namely, the plane constructed by the vectors $\hat{\mathbf{n}}^{inc}$ and $\hat{\mathbf{n}}^{sca}$), i.e. $\hat{\mathbf{e}}_{\perp}^{inc/sca} = \hat{\mathbf{n}}^{inc} \times \hat{\mathbf{n}}^{sca}$, and $\hat{\mathbf{e}}_{\parallel}$ is a vector parallel to the scattering plane such that $\hat{\mathbf{n}} = \hat{\mathbf{e}}_{\parallel} \times \hat{\mathbf{e}}_{\perp}$. In the far-field approximation, the scattered wave is related to the incident wave by

$$\begin{bmatrix} E_{\parallel}^{sca} \\ E_{\perp}^{sca} \end{bmatrix} = \frac{\exp(ik_1 r)}{r} \mathbf{S}(\hat{\mathbf{n}}^{sca}, \hat{\mathbf{n}}^{inc}) \begin{bmatrix} E_{\parallel}^{inc} \\ E_{\perp}^{inc} \end{bmatrix}, \quad (2.31)$$

where \mathbf{S} is a 2×2 complex amplitude scattering matrix that linearly transforms the electric field vector components of the incident wave into the electric field vector components of the scattered wave.

Laboratory optical instruments cannot directly measure the electric field of a beam of light but rather measure some quantities related to the energy flux (or irradiance) of the beam that are quadratic combinations of the electric field components. Therefore, the Stokes vector of a monochromatic transverse electromagnetic wave is

introduced as

$$\tilde{\mathbf{I}} = \begin{bmatrix} \tilde{I} \\ \tilde{Q} \\ \tilde{U} \\ \tilde{V} \end{bmatrix} = \frac{1}{2} \sqrt{\frac{\epsilon}{\mu}} \begin{bmatrix} E_{\parallel} E_{\parallel}^* + E_{\perp} E_{\perp}^* \\ E_{\parallel} E_{\parallel}^* - E_{\perp} E_{\perp}^* \\ -E_{\parallel} E_{\perp}^* - E_{\perp} E_{\parallel}^* \\ i(E_{\perp} E_{\parallel}^* - E_{\parallel} E_{\perp}^*) \end{bmatrix}. \quad (2.32)$$

For an monochromatic electromagnetic wave, $\tilde{I}^2 = \tilde{Q}^2 + \tilde{U}^2 + \tilde{V}^2$. For quasi-monochromatic electromagnetic wave that are incoherent mixtures of many monochromatic waves, $\tilde{I}^2 \geq \tilde{Q}^2 + \tilde{U}^2 + \tilde{V}^2$. The ratio $DoLP = \sqrt{(\tilde{Q}^2 + \tilde{U}^2 + \tilde{V}^2)/\tilde{I}^2} \leq 1$ is called the degree of polarization which is equal to unity for fully polarized light, while the ratios $\sqrt{(\tilde{Q}^2 + \tilde{U}^2)/\tilde{I}^2}$ and \tilde{V}/\tilde{I} are called the degrees of linear and circular polarization, respectively. For unpolarized or natural light, $\tilde{Q} = \tilde{U} = \tilde{V} = 0$.

The Stokes vector is always defined with respect to a reference plane, the scattering plane in this case. If the reference plane is rotated through an angle θ in the anticlockwise direction when looking in the direction of propagation, the transformation of the original Stokes vector $\tilde{\mathbf{I}}$ into the new Stokes vector $\tilde{\mathbf{I}}'$ is given by a 4×4 rotation matrix \mathbf{L} :

$$\tilde{\mathbf{I}}' = \mathbf{L}(\theta) \tilde{\mathbf{I}} = \begin{bmatrix} 1 & 0 & 0 & 0 \\ 0 & \cos 2\theta & \sin 2\theta & 0 \\ 0 & -\sin 2\theta & \cos 2\theta & 0 \\ 0 & 0 & 0 & 1 \end{bmatrix} \tilde{\mathbf{I}}. \quad (2.33)$$

Following the definition of the amplitude scattering matrix and the Stokes vector, the transformation of the Stokes vector of the incident plane wave into the scattered spherical wave due to light scattering by a single particle is given by

$$\tilde{\mathbf{I}}^{sca} = \frac{1}{r^2} \tilde{\mathbf{Z}}(\hat{\mathbf{n}}^{sca}, \hat{\mathbf{n}}^{inc}) \tilde{\mathbf{I}}^{inc}, \quad (2.34)$$

where $\tilde{\mathbf{Z}}(\hat{\mathbf{n}}^{sca}, \hat{\mathbf{n}}^{inc})$ is the 4×4 phase matrix whose elements can be expressed in terms of elements of amplitude scattering matrix $\mathbf{S}(\hat{\mathbf{n}}^{inc}, \hat{\mathbf{n}}^{inc})$ as:

$$\tilde{Z}_{11} = \frac{1}{2}(|S_{11}|^2 + |S_{12}|^2 + |S_{21}|^2 + |S_{22}|^2), \quad (2.35)$$

$$\tilde{Z}_{12} = \frac{1}{2}(|S_{11}|^2 - |S_{12}|^2 + |S_{21}|^2 - |S_{22}|^2), \quad (2.36)$$

$$\tilde{Z}_{13} = -\text{Re}(S_{11}S_{12}^* + S_{22}S_{21}^*), \quad (2.37)$$

$$\tilde{Z}_{14} = -\text{Im}(S_{11}S_{12}^* - S_{22}S_{21}^*), \quad (2.38)$$

$$\tilde{Z}_{21} = \frac{1}{2}(|S_{11}|^2 + |S_{12}|^2 - |S_{21}|^2 - |S_{22}|^2), \quad (2.39)$$

$$\tilde{Z}_{22} = \frac{1}{2}(|S_{11}|^2 - |S_{12}|^2 - |S_{21}|^2 + |S_{22}|^2), \quad (2.40)$$

$$\tilde{Z}_{23} = -\text{Re}(S_{11}S_{12}^* - S_{22}S_{21}^*), \quad (2.41)$$

$$\tilde{Z}_{24} = -\text{Im}(S_{11}S_{12}^* + S_{22}S_{21}^*), \quad (2.42)$$

$$\tilde{Z}_{31} = -\text{Re}(S_{11}S_{21}^* + S_{22}S_{12}^*), \quad (2.43)$$

$$\tilde{Z}_{32} = -\text{Re}(S_{11}S_{21}^* - S_{22}S_{12}^*), \quad (2.44)$$

$$\tilde{Z}_{33} = \text{Re}(S_{11}S_{22}^* + S_{12}S_{21}^*), \quad (2.45)$$

$$\tilde{Z}_{34} = \text{Im}(S_{11}S_{22}^* + S_{21}S_{12}^*), \quad (2.46)$$

$$\tilde{Z}_{41} = -\text{Im}(S_{21}S_{11}^* + S_{22}S_{12}^*), \quad (2.47)$$

$$\tilde{Z}_{42} = -\text{Im}(S_{21}S_{11}^* - S_{22}S_{12}^*), \quad (2.48)$$

$$\tilde{Z}_{43} = \text{Im}(S_{22}S_{11}^* - S_{12}S_{21}^*), \quad (2.49)$$

$$\tilde{Z}_{44} = \text{Re}(S_{22}S_{11}^* - S_{12}S_{21}^*). \quad (2.50)$$

In general, only 7 of the phase matrix elements of a single particle are independent.

For randomly oriented particles with each particle a plane of symmetry, the ensemble averaged phase matrix per particle $\langle \tilde{\mathbf{Z}} \rangle$ is invariant with respect to the choice of the scattering plane and depends only on the scattering angle Θ between the inci-

dent and the scattered directions, where $\cos \Theta = \hat{\mathbf{n}}^{sca} \cdot \hat{\mathbf{n}}^{inc}$. Therefore, the scattering matrix has the well-known block-diagonal structure

$$\mathbf{P}(\Theta) = \frac{4\pi}{C_{sca}} \langle \tilde{\mathbf{Z}}(\hat{\mathbf{n}}^{sca}, \hat{\mathbf{n}}^{inc}) \rangle = \begin{bmatrix} a_1(\Theta) & b_1(\Theta) & 0 & 0 \\ b_1(\Theta) & a_2(\Theta) & 0 & 0 \\ 0 & 0 & a_3(\Theta) & b_2(\Theta) \\ 0 & 0 & -b_2(\Theta) & a_4(\Theta) \end{bmatrix}, \quad (2.51)$$

where the ensemble averaged scattering cross-section per particle C_{sca} , which is defined as the total monochromatic power removed from the incident beam resulting solely from light scattering by the particle over the monochromatic incident energy flux, is given by

$$C_{sca} = 2\pi \int_{-1}^{+1} \langle \tilde{Z}_{11}(\Theta) \rangle d(\cos \Theta), \quad (2.52)$$

and the normalization factor $4\pi/C_{sca}$ follows from the conventional normalization condition for the phase function a_1 (or P_{11}):

$$\frac{1}{2} \int_{-1}^{+1} a_1(\Theta) d(\cos \Theta) = 1. \quad (2.53)$$

The ensemble averaged extinction cross-section per particle, C_{ext} , which is defined as the total monochromatic power removed from the incident beam over the monochromatic incident energy flux, is given by

$$C_{ext} = \frac{2\pi}{k} \text{Im}[\langle S_{11}(\hat{\mathbf{n}}, \hat{\mathbf{n}}) \rangle + \langle S_{22}(\hat{\mathbf{n}}, \hat{\mathbf{n}}) \rangle]. \quad (2.54)$$

the ensemble averaged absorption cross-section per particle C_{abs} , which is defined as the total monochromatic power removed from the incident beam resulting solely from absorption of light by the particle over the monochromatic incident energy flux,

is given by

$$C_{abs} = C_{ext} - C_{sca}. \quad (2.55)$$

The ratio of the scattering and extinction cross-sections is called the single-scattering albedo ω , i.e.

$$\omega = \frac{C_{sca}}{C_{ext}}. \quad (2.56)$$

The quantity

$$g = \langle \cos \Theta \rangle = \frac{1}{2} \int_{-1}^1 a_1(\Theta) \cos \Theta d(\cos \Theta), \quad (2.57)$$

is called the asymmetry factor of the phase function.

In order to solve the single-scattering problem and obtain single-scattering properties including the cross-sections, single-scattering albedo and phase matrix of dust aerosols, one needs to solve the vector Helmholtz equation $\nabla^2 \mathbf{E} + k^2 \mathbf{E} = 0$ for the scattered field. The general solution to the equation has three components: \mathbf{L} , $\mathbf{M}^{\mathbf{a}}$, $\mathbf{N}^{\mathbf{a}}$, i.e.,

$$\mathbf{L} = \nabla \psi, \quad (2.58)$$

$$\mathbf{M}^{\mathbf{a}} = \nabla \times (\psi \mathbf{a}), \quad (2.59)$$

$$\mathbf{N}^{\mathbf{a}} = \frac{1}{k} \nabla \times \mathbf{M}^{\mathbf{a}}, \quad (2.60)$$

where \mathbf{a} is either an arbitrary constant unit vector or the position vector $\hat{\mathbf{r}}$ and ψ satisfy the scalar Helmholtz equation

$$\nabla^2 \psi(\mathbf{r}) + k^2 \psi(\mathbf{r}) = 0. \quad (2.61)$$

By considering the fact that the incident plane wave and the scattered wave in the far field region are transversely polarized, the \mathbf{L} term is eliminated.

2.3 Computation of Spheroidal Functions

Despite the simple mathematic form of the scalar Helmholtz equation, the exact analytical computational method only exists for the spherical particle in the three-dimensional space. Mathematically, analytical solutions for spheroidal particles have been obtained in spheroidal coordinates. However, there is no reliable numerical code due to the slow development of the computational algorithm for spheroidal functions. The earliest study of the calculation of spheroidal functions can be dated back to 1947, when Bouwkamp developed a Newton-like-iterative method ([14]). Relying on the initial guess, this method is not stable for extreme and complex parameters, even though it is still widely used to refine the eigenvalues. Hodge (1970, [20]) converted the eigenvalue problem to a tri-diagonal matrix form which is much easier for computational implementation. Nevertheless, this method is still limited to real and small parameters. Li (1998, [27]) derived an empirical estimation and boundary for the eigenvalues, which allows to obtain the exact values using an iterative method. Although this method works for complex parameters, it would fail if parameters become large. Falloon (2003, [11]) generalized the Hodge's method to the whole complex domain and developed a package, which is imbedded in the commercial program Wolfram Mathematica. To the knowledge of the author, this code is the most sophisticate and accurate so far. However, based on the EPC (Extended Precision Calculation) of Mathematica, the code is very slow and is not stable when calculating the spheroidal radial functions as we will see later. As an effort to explore light scattering simulation of spheroidal particles, we present a new efficient and stable computational method for spheroidal angle functions, radial functions of the first kind and the second kind, and their corresponding first order derivatives in this subsection.

2.3.1 Spheroidal Coordinate Systems

In the following definition of the spheroidal coordinates, the z axis of the Cartesian coordinate system is considered as the rotational symmetric axis of the spheroidal coordinates. Let d be the corresponding inter-focal distance. The prolate (e.g. the aspect ratio is greater than 1) spheroidal coordinates (η, ξ, φ) are then related to the Cartesian coordinates by the transformation

$$x = \frac{d}{2}[(1 - \eta^2)(\xi^2 - 1)]^{1/2} \cos \varphi, y = \frac{d}{2}[(1 - \eta^2)(\xi^2 - 1)]^{1/2} \sin \varphi, z = \frac{d}{2}\eta\xi, \quad (2.62)$$

with $-1 \leq \eta \leq 1$, $1 \leq \xi < \infty$, and $0 \leq \varphi \leq 2\pi$. The oblate (e.g. the aspect ratio is smaller than 1) spheroidal coordinates are related to the Cartesian coordinates by the transformation

$$x = \frac{d}{2}[(1 - \eta^2)(\xi^2 + 1)]^{1/2} \cos \varphi, y = \frac{d}{2}[(1 - \eta^2)(\xi^2 + 1)]^{1/2} \sin \varphi, z = \frac{d}{\eta}\xi, \quad (2.63)$$

with $-1 \leq \eta \leq 1$, $0 \leq \xi < \infty$, and $0 \leq \varphi \leq 2\pi$.

2.3.2 Separation of Variables for the Scalar Helmholtz Equation

The scalar Helmholtz equation can be written in prolate spheroidal coordinates as

$$\left[\frac{\partial}{\partial \eta}(1 - \eta^2) \frac{\partial}{\partial \eta} + \frac{\partial}{\partial \xi}(\xi^2 - 1) \frac{\partial}{\partial \xi} + \frac{\xi^2 - \eta^2}{(\xi^2 - 1)(1 - \eta^2)} \frac{\partial^2}{\partial \varphi^2} + c^2(\xi^2 - \eta^2) \right] \psi = 0, \quad (2.64)$$

and in oblate spheroidal coordinates as

$$\left[\frac{\partial}{\partial \eta}(1 - \eta^2) \frac{\partial}{\partial \eta} + \frac{\partial}{\partial \xi}(\xi^2 + 1) \frac{\partial}{\partial \xi} + \frac{\xi^2 + \eta^2}{(\xi^2 + 1)(1 - \eta^2)} \frac{\partial^2}{\partial \varphi^2} + c^2(\xi^2 + \eta^2) \right] \psi = 0, \quad (2.65)$$

where $c = kd/2$. Notice that the equation (2.64) can be converted to the equation (2.65) by applying the transformation $\xi \rightarrow \pm i\xi$, $c \rightarrow \mp ic$. Thus, without losing generality, we will focus on the discussion of prolate spheroidal functions in the following subsections, and the oblates spheroidal functions can be simply obtained with this transformation.

Via the usual procedure of the separation of variables, elementary solutions to the equation (2.64) are expressed in the form of the Lamé products

$$\psi_{omn}^e = S_{mn}(c, \eta) R_{mn}(c, \xi) \frac{\cos m\varphi}{\sin m\varphi}, \quad (2.66)$$

where e and o indicate the even and the odd functions of the azimuth angle φ , respectively. The prolate spheroidal angle function $S_{mn}(c, \eta)$ and the prolate spheroidal radial function $R_{mn}(c, \xi)$ satisfy the differential equations

$$\frac{d}{d\eta} \left[(1 - \eta^2) \frac{d}{d\eta} S_{mn}(c, \eta) \right] + \left[\lambda_{mn} - c^2 \eta^2 - \frac{m^2}{1 - \eta^2} \right] S_{mn}(c, \eta) = 0, \quad (2.67)$$

and

$$\frac{d}{d\xi} \left[(\xi^2 - 1) \frac{d}{d\xi} R_{mn}(c, \xi) \right] - \left[\lambda_{mn} - c^2 \xi^2 + \frac{m^2}{\xi^2 - 1} \right] R_{mn}(c, \xi) = 0, \quad (2.68)$$

where λ_{mn} and m are separation constants. Due to the periodic boundary condition of φ , the eigenvalues of m must be non-negative integers. The eigenvalues of λ_{mn} ($n = m, m + 1, m + 2, \dots$) can be obtained from the condition that the solutions to the differential equation (2.67) are finite at $\eta = \pm 1$.

2.3.3 The Prolate Spheroidal Angle Function

The prolate spheroidal angle function can be expressed as an infinite sum of the associated Legendre functions

$$S_{mn}(c, \eta) = \sum_{r=0,1}^{\infty} {}' d_r^{mn}(c) P_{m+r}^m(\eta), \quad (2.69)$$

where the prime over the summation sign indicates that the summation is over only even values of r when $n - m$ is even, and over only odd values of r when $n - m$ is odd. Substituting the equation (2.69) into the equation (2.64), we obtain the following recursion formula for the expansion coefficients d_r^{mn} :

$$N_r^m = \frac{\beta_r^m}{\gamma_r^m - \lambda_{mn} - N_{r+2}^m}, \quad (2.70)$$

where γ_r^m , β_r^m , N_r^m are defined as

$$\begin{aligned} \gamma_r^m &= (m+r)(m+r+1) \\ &+ \frac{1}{2}c^2 \left[1 - \frac{4m^2 - 1}{(2m+2r-1)(2m+2r+3)} \right] (r \geq 0), \end{aligned} \quad (2.71)$$

$$\beta_r^m = \frac{r(r-1)(2m+r)(2m+r-1)c^4}{(2m+2r-1)^2(2m+2r-3)(2m+2r+1)} (r \geq 2), \quad (2.72)$$

$$N_r^m = \frac{(2m+r)(2m+r-1)c^2}{(2m+2r-1)(2m+2r+1)} \frac{d_r^{mn}}{d_{r-2}^{mn}} (r \geq 2). \quad (2.73)$$

Since $d_r^{mn} = 0 (r < 0)$ and $\lim_{r \rightarrow \infty} d_r^{mn} / d_{r-2}^{mn} = 0$, iterating of equation (2.70), we obtain a transcendental equation between λ_{mn} and c^2 in the form of an infinite

continued fraction

$$\begin{aligned} \gamma_{n-m}^m - \lambda_{mn} - \frac{\beta_{n-m}^m}{\gamma_{n-m-2}^m - \lambda_{mn} - \frac{\beta_{n-m-2}^m}{\gamma_{n-m-4}^m - \lambda_{mn} - \frac{\beta_{n-m-4}^m}{\dots}}} \\ - \frac{\beta_{n-m+2}^m}{\gamma_{n-m-2}^m - \lambda_{mn} - \frac{\beta_{n-m+4}^m}{\gamma_{n-m+4}^m - \lambda_{mn} - \frac{\beta_{n+m+6}^m}{\dots}}} = 0. \end{aligned} \quad (2.74)$$

Traditionally, the solution to the equation (2.74) can be obtained in two steps: First, use a power series of c^2 or some empirical functions to obtain a close enough approximation to the eigenvalue λ_{mn} ; Second, use a Newton-like iterative method to refine the result in the vicinity of the approximated value ([14]). This method works well for small and real values of c^2 . When c^2 becomes large for large-sized or highly eccentric particles or has an imaginary part for absorbing particles, the iteration may fail to converge to the correct answer.

An alternative way to solve the equation (2.74) is to express it in a tridiagonal matrix form ([20]):

$$\begin{pmatrix} B_{0,1}^{mn} & C_{0,1}^{mn} & & & \\ A_{2,3}^{mn} & B_{2,3}^{mn} & C_{2,3}^{mn} & & \\ & A_{4,5}^{mn} & B_{4,5}^{mn} & \ddots & \\ & & \ddots & \ddots & \end{pmatrix} \begin{pmatrix} d_{0,1}^{mn} \\ d_{2,3}^{mn} \\ d_{4,5}^{mn} \\ \vdots \end{pmatrix} = \lambda_{mn} \begin{pmatrix} d_{0,1}^{mn} \\ d_{2,3}^{mn} \\ d_{4,5}^{mn} \\ \vdots \end{pmatrix}, \quad (2.75)$$

where A_r^{mn} , B_r^{mn} , C_r^{mn} are defined as

$$\beta_r^{mn} = A_r^{mn} C_{r-2}^{mn}, \quad (2.76)$$

$$\gamma_r^{mn} = B_r^{mn}, \quad (2.77)$$

$$N_r^{mn} = C_{r-2}^{mn} \frac{d_r^{mn}}{d_{r-2}^{mn}}. \quad (2.78)$$

We followed this idea and proposed a new method based on normalization. For example, define the normalized associate Legendre function as

$$\tilde{P}_{m+r}^m(\eta) = \sqrt{\frac{2m+2r+1}{2}} \sqrt{\frac{r!}{(2m+r)!}} P_{m+r}^m(\eta). \quad (2.79)$$

The expansion of the spheroidal angle function becomes

$$S_{mn}(c, \eta) = \sum_{r=0,1}^{\infty} f_r^{mn}(c) \tilde{P}_{m+r}^m(\eta), \quad (2.80)$$

where

$$f_r^{mn} = \sqrt{\frac{2}{2m+2r+1}} \sqrt{\frac{(2m+r)!}{r!}} d_r^{mn} \quad (2.81)$$

is the eigenvector of the symmetric tridiagonal matrix, i.e.

$$\begin{pmatrix} \tilde{B}_{0,1}^{mn} & \tilde{A}_{0,1}^{mn} & & & \\ \tilde{A}_{0,1}^{mn} & \tilde{B}_{2,3}^{mn} & \tilde{A}_{2,3}^{mn} & & \\ & \tilde{A}_{4,5}^{mn} & \tilde{B}_{4,5}^{mn} & \ddots & \\ & & \ddots & \ddots & \ddots \end{pmatrix} \begin{pmatrix} f_{0,1}^{mn} \\ f_{2,3}^{mn} \\ f_{4,5}^{mn} \\ \vdots \end{pmatrix} = \frac{\lambda_{mn}}{c^2} \begin{pmatrix} f_{0,1}^{mn} \\ f_{2,3}^{mn} \\ f_{4,5}^{mn} \\ \vdots \end{pmatrix}, \quad (2.82)$$

where

$$\tilde{A}_r^{mn} = \frac{\sqrt{(2m+r)(2m+r-1)(r-1)r}}{(2m+2r-1)\sqrt{(2m+2r+1)(2m+2r-3)}}, \quad (2.83)$$

$$\tilde{B}_r^{mn} = \frac{2(m+r)(m+r+1) - 2m^2 - 1}{(2m+2r-1)(2m+2r+3)} + \frac{(m+r)(m+r+1)}{c^2}. \quad (2.84)$$

The eigenvalue problem of a symmetric tridiagonal matrix can be efficiently solved numerically with, say, the QL algorithm with implicit shifts, by which the eigenvector f_r^{mn} can be derived at the meantime. The Euclidean norm of the eigenvector f_r^{mn} is

set to 1 in the QL algorithm, i.e.

$$\sum_{r=0,1}^{\infty} |f_r^{mn}(c)|^2 = 1. \quad (2.85)$$

Compared with previous methods, this new method has advantages in four aspects. First, it can stably converge to the correct eigenvalue for arbitrary c in the whole complex plane. Second, it will not lose precision: if double precision is used in the calculation, all the 15 significant digits of the result will be the same as those of the exact value. Third, computers can handle the normalized Legendre functions more easily than the unnormalized one, since it is less likely to encounter the problem of overflow when dealing with extremely large parameters. Last, the resulting spheroidal angle function $S_{mn}(c, \eta)$ automatically satisfies the orthogonal condition

$$\int_{-1}^1 S_{mn}(c, \eta) S_{m'n'}(c, \eta) d\eta = \delta_{nn'}, \quad (2.86)$$

which makes it convenient to be applied to scattering problems.

2.3.4 The Prolate Spheroidal Radial Function

In the light scattering problem, both of the spheroidal radial functions of the first kind $R_{mn}^{(1)}$ and the second kind $R_{mn}^{(2)}$ are required. Here we impose the normalization conditions so that the asymptotic forms of the spheroidal radial functions are given by

$$R_{mn}^{(1)}(c, \xi) \xrightarrow{c\xi \rightarrow \infty} \frac{1}{c\xi} \cos \left[c\xi - \frac{1}{2}(n+1)\pi \right], \quad (2.87)$$

$$R_{mn}^{(2)}(c, \xi) \xrightarrow{c\xi \rightarrow \infty} \frac{1}{c\xi} \sin \left[c\xi - \frac{1}{2}(n+1)\pi \right]. \quad (2.88)$$

The spheroidal radial function of the first kind can be expressed as a summation of a series of spherical Bessel functions:

$$R_{mn}^{(1)}(c, \xi) = \frac{1}{S_{mn}(c, 0)} \sum_{k=0}^{\infty} i^{m-n+2k} f_{2k}^{mn} \tilde{P}_{m+2k}^m(0) j_{m+2k}[c(\xi^2 - 1)^{1/2}], \quad (2.89)$$

when $(n - m)$ is even;

$$R_{mn}^{(1)}(c, \xi) = \frac{1}{S'_{mn}(c, 0)} \frac{\xi}{(\xi^2 - 1)^{1/2}} \sum_{k=0}^{\infty} i^{m-n+2k+1} f_{2k+1}^{mn} \tilde{P}_{m+2k+1}^m(0) j_{m+2k+1}[c(\xi^2 - 1)^{1/2}], \quad (2.90)$$

when $n - m$ is odd. Notice that the expression (5.3.21) in Flammer's classic book on spheroidal functions ([14]), which is different with the equation (2.90) by a factor of $\xi/(\xi^2 - 1)^{1/2}$, is actually wrong.

Accordingly, the spheroidal radial function of the second kind can be expressed as a summation of a series of spherical Neumann functions:

$$R_{mn}^{(2)}(c, \xi) = \frac{1}{S_{mn}(c, 0)} \sum_{k=0}^{\infty} i^{m-n+2k} f_{2k}^{mn} \tilde{P}_{m+2k}^m(0) y_{m+2k}[c(\xi^2 - 1)^{1/2}], \quad (2.91)$$

when $(n - m)$ is even;

$$R_{mn}^{(2)}(c, \xi) = \frac{1}{S'_{mn}(c, 0)} \frac{\xi}{(\xi^2 - 1)^{1/2}} \sum_{k=0}^{\infty} i^{m-n+2k+1} f_{2k+1}^{mn} \tilde{P}_{m+2k+1}^m(0) y_{m+2k+1}[c(\xi^2 - 1)^{1/2}], \quad (2.92)$$

when $n - m$ is odd. Mathematically, the summations in equations (2.91) and (2.92) are always converged for all ξ in the complex plane. For the numerical concern, however, the summation of the series may fail to converge in the vicinity of $\xi^2 = 1$, due to the bad behavior of the Neumann function at 0. Therefore, it is important to

introduce an alternative summation of series:

$$R_{mn}^{(2)}(c, \xi) = \frac{1}{\sum_{r=0,1}^{\infty} {}'g_r^{mn}(c)} \left(\frac{\xi^2 - 1}{\xi^2}\right)^{m/2} \sum_{r=0,1}^{\infty} {}'i^{m-n+r} g_r^{mn}(c) j_{m+r}(c\xi), \quad (2.93)$$

where

$$g_r^{mn} = \sqrt{\frac{2m + 2r + 1}{2}} \sqrt{\frac{(2m + r)!}{r!}} f_r^{mn}. \quad (2.94)$$

The equation (2.93) converges slowly but will not diverge in the vicinity of $\xi = 1$.

The Wronskian of $R_{mn}^{(1)}$ and $R_{mn}^{(2)}$ can be found directly from the equation (2.68) and the asymptotic forms (2.87) and (2.88). In spite of the complicated forms of $R_{mn}^{(1)}$ and $R_{mn}^{(2)}$, the Wronskian is in a rather simple compact form:

$$W[R_{mn}^{(1)}, R_{mn}^{(2)}] = R_{mn}^{(1)} \frac{dR_{mn}^{(2)}}{d\xi} - R_{mn}^{(2)} \frac{dR_{mn}^{(1)}}{d\xi} = \frac{1}{c(\xi^2 - 1)}, \quad (2.95)$$

which is useful when checking the accuracy of the computation of the spheroidal radial functions.

2.3.5 Results

Based on the new algorithm, we developed a C++ code to compute the spheroidal angle and radial functions as well as their corresponding first order derivatives. Compared with the spheroidal functions implemented in the sophisticated commercial program Wolfram Mathematica, our code is much efficient since the eigenvalue problem is greatly simplified in the form of a symmetric tridiagonal matrix and it does not rely on the extend precision in the calculation.

As for the precision, the comparison between the Mathematica and our new method for the Wronskian and the spheroidal functions as well as their corresponding first order derivatives for regular parameters ($n = 10, m = 5, c = 5\pi$) is shown in

Figure 2.4. It is clear that both of the Mathematica and the new method can obtain the accurate Wronskian with up to 15 significant digits (this value can be further improved if extended precision is used for the new method). Moreover, all the spheroidal functions are agreed perfectly well between the two independent codes. Another comparison for some extreme parameters, e.g. ($n = 100, m = 50, c = 50\pi$), is shown in Figure 2.5. Regarding the spheroidal angle function and its first order derivative, the two methods still agree well with each other. However, when calculating the spheroidal radial function of the first kind and its derivative, the results of the Mathematica diverged after a very long computational period; When calculating the spheroidal radial function of the second kind and its derivative, the Mathematica seemed to be running forever without providing any result. On the other hand, our new method still provided reasonable results as the Wronskian agrees with the analytical result.

The calculation of spheroidal functions with extreme parameters is necessary when considering scattering problems involving large-sized or highly eccentric spheroid. Furthermore, the success of this new method in the whole complex plane makes it applicable to the scattering problem of absorbing particles.

2.4 Single-Scattering Property Database of Mineral Dust Aerosols

Although our new method for the calculation of spheroidal functions has shown its potential in the application to the light scattering problem by spheroidal particles, we still cannot afford the computational burden of the light scattering simulation of spheroidal particles if we have to run the simulation every time we use the single-scattering properties. Instead, we use a newly developed pre-calculated single-scattering property database of mineral dust aerosols.

The database is based on tri-axial ellipsoidal models to simulate the non-sphericity

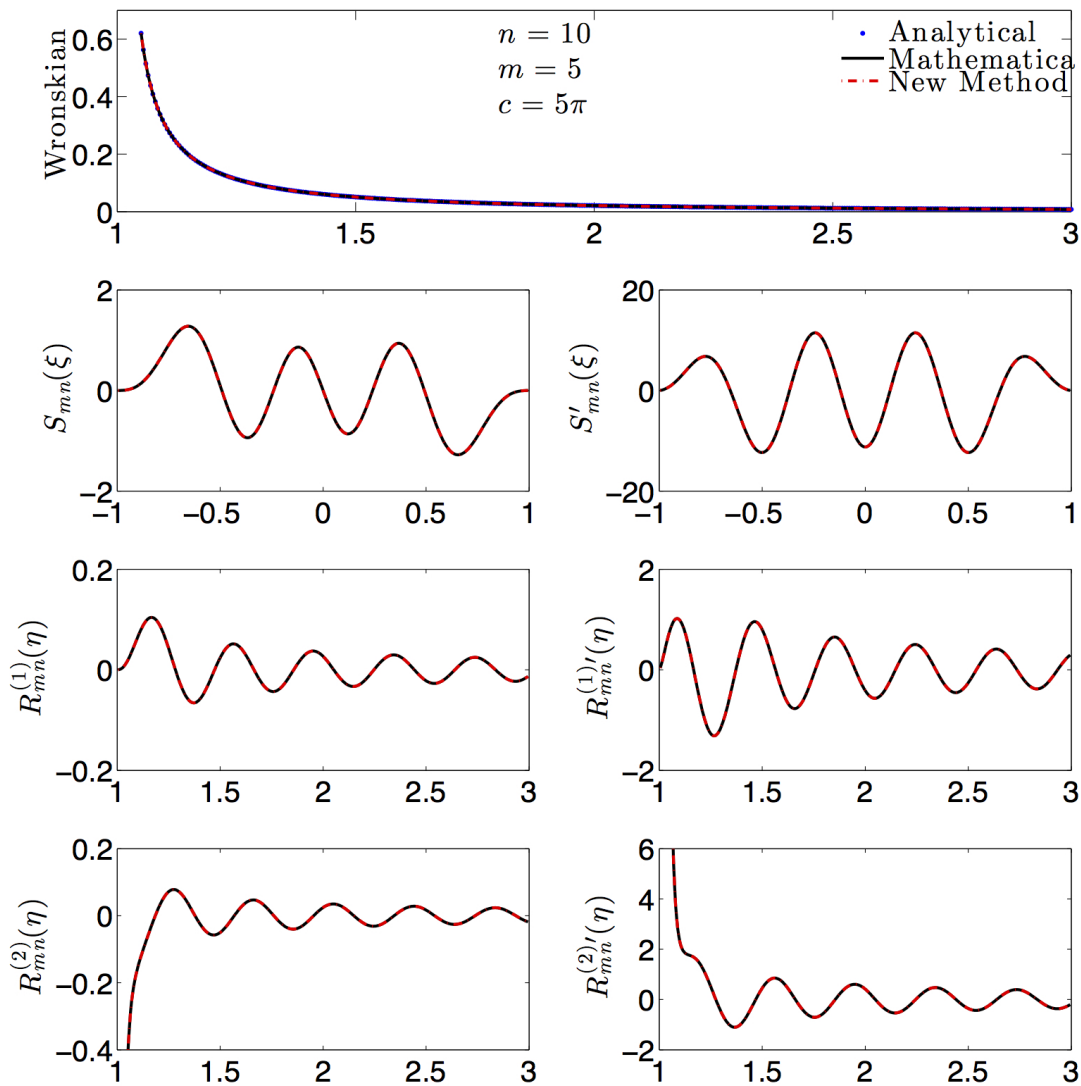


Figure 2.4: Comparison between the analytical result, the results of the spheroidal functions imbedded in the Wolfram Mathematica and the new method for regular parameters ($n = 10, m = 5, c = 5\pi$). The top panel shows the perfectly matched Wronskian for the three methods. The following three plots on the left column show the spheroidal angle function, the radial functions of the first kind and the second kind calculated by the Mathematica and our new method. The other three plots on the right column show the corresponding derivatives of the spheroidal functions.

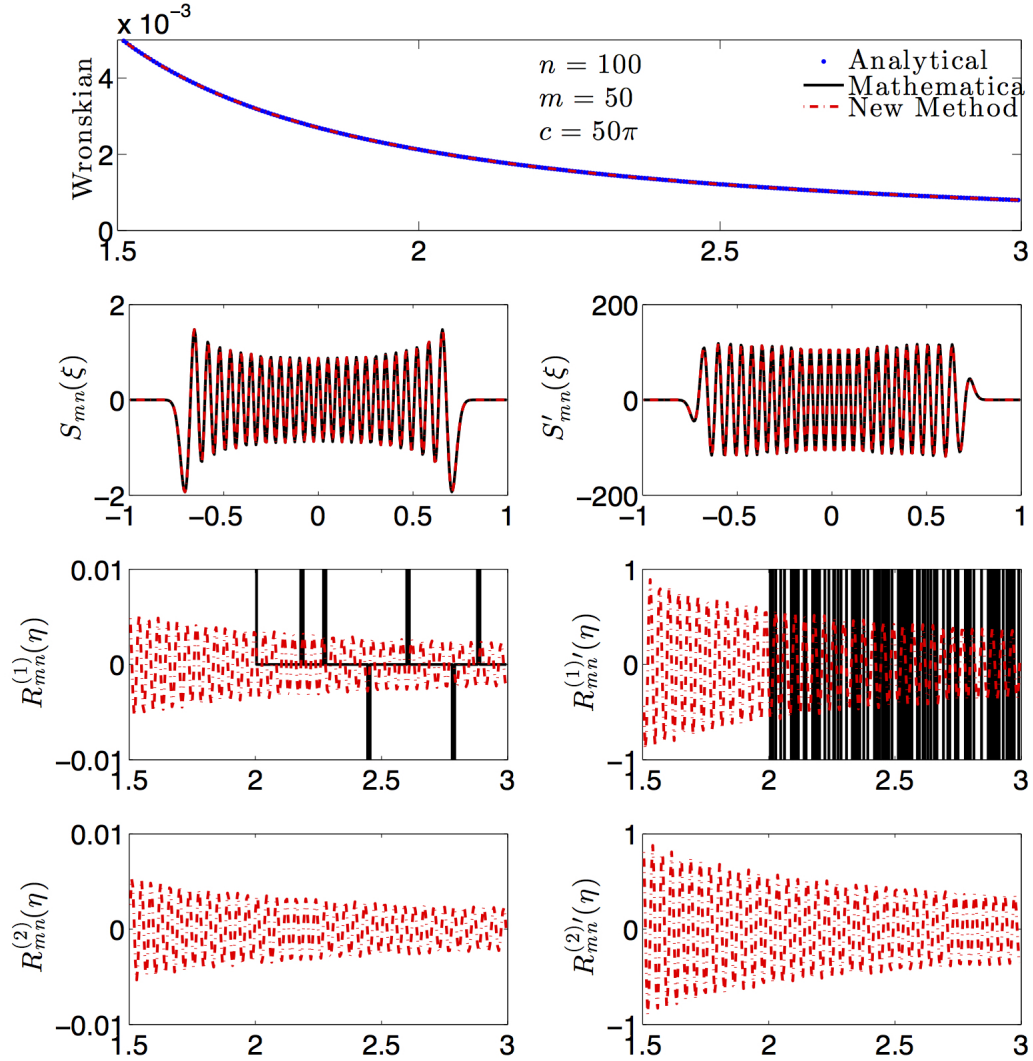


Figure 2.5: Comparison between the analytical result, the results of the spheroidal functions imbedded in the Wolfram Mathematica and the new method for extreme parameters ($n = 100, m = 50, c = 5\pi$). The top panel shows the perfectly matched Wronskian for the analytical method and our new method only, since the Mathematica failed to converge for such large parameters. The following three plots on the left column show the spheroidal angle function, the radial functions of the first kind and the second kind calculated by the Mathematica and our new method. The other three plots on the right column show the corresponding derivatives of the spheroidal functions. In fact, the Mathematica provided completely wrong results for the radial function of the first kind and kept running without providing any result for the radial function of the second kind.

Table 2.1: Ranges of microphysical properties.

| Microphysical Properties | Ranges |
|--|----------------|
| Size Parameter x | 0.025 - 1000.0 |
| Aspect Ratio $\varepsilon_{a/c}$ | 0.3 - 1.0 |
| Aspect Ratio $\varepsilon_{b/c}$ | 0.3 - 1.0 |
| Real Part of Refractive Index m_r | 1.1 - 2.1 |
| Imaginary Part of Refractive Index m_i | 0.0005 - 0.5 |

of dust aerosols. There are five dimensions or microphysical properties considered in the database: one size parameter, two aspect ratio, and two parts of the complex refractive indices. The ranges of those parameters are given by the table 2.1. A combination of the Lorenz-Mie theory, the T-matrix method, the ADDA (Amsterdam Discrete Dipole Approximation), and the IGOM is used to simulate the single-scattering properties of ellipsoidal particles, including of the extinction cross-sections, the single-scattering albedos and the phase matrices, according to the feasibility of each method. The database is featured by formatting the single-scattering properties of ellipsoidal particles in the kernel form to allow for an efficient retrieval. For example, the ensemble averaged single-scattering properties of polydispersed ellipsoidal particles can be retrieved by

$$\langle C_{ext/sca/abs}(m_r, m_i, \varepsilon_{a/c}, \varepsilon_{b/c}, \bar{x}) \rangle = \sum_m \frac{dN(x^m)}{d \ln x} K_{ext/sca/abs}(m_r, m_i, \varepsilon_{a/c}, \varepsilon_{b/c}, x^m), \quad (2.96)$$

$$\langle C_{sca}(m_r, m_i, \varepsilon_{a/c}, \varepsilon_{b/c}, \bar{x}) \rangle \langle P_{ij}(m_r, m_i, \varepsilon_{a/c}, \varepsilon_{b/c}, \bar{x}; \Theta) \rangle = \sum_m \frac{dN(x^m)}{d \ln x} K_{sca}(m_r, m_i, \varepsilon_{a/c}, \varepsilon_{b/c}, x^m) K_{ij}(m_r, m_i, \varepsilon_{a/c}, \varepsilon_{b/c}, x^m; \Theta), \quad (2.97)$$

where $N(x)$ is the particle size distribution, x^m denotes the size parameter at the center of each size bin of the database, and P_{ij} represents an element of the phase matrix

with subscripts $1 \leq i \leq 4$ and $1 \leq j \leq 4$. Here, $K_{ext/sca/abs}(m_r, m_i, \varepsilon_{a/c}, \varepsilon_{b/c}, x)$ and $K_{ij}(m_r, m_i, \varepsilon_{a/c}, \varepsilon_{b/c}, x; \Theta)$ are pre-integrated kernels stored in the database, which are defined as

$$K_{ext/sca/abs}(m_r, m_i, \varepsilon_{a/c}, \varepsilon_{b/c}, x_l) = \int_{\ln x_l}^{\ln x_{l+1}} h_l(x) C_{ext/sca/abs}(m_r, m_i, \varepsilon_{a/c}, \varepsilon_{b/c}, x) d \ln x + \int_{\ln x_{l-1}}^{\ln x_l} g_l(x) C_{ext/sca/abs}(m_r, m_i, \varepsilon_{a/c}, \varepsilon_{b/c}, x) d \ln x, \quad (2.98)$$

$$K_{ij}(m_r, m_i, \varepsilon_{a/c}, \varepsilon_{b/c}, x_l; \Theta) = \int_{\ln x_l}^{\ln x_{l+1}} h_l(x) C_{sca}(m_r, m_i, \varepsilon_{a/c}, \varepsilon_{b/c}, x) P_{ij}(m_r, m_i, \varepsilon_{a/c}, \varepsilon_{b/c}, x; \Theta) d \ln x + \int_{\ln x_{l-1}}^{\ln x_l} g_l(x) C_{sca}(m_r, m_i, \varepsilon_{a/c}, \varepsilon_{b/c}, x) P_{ij}(m_r, m_i, \varepsilon_{a/c}, \varepsilon_{b/c}, x; \Theta) d \ln x, \quad (2.99)$$

where x_l denotes the size parameter at the boundary of each size bin of the database, and $h_l(x)$ and $g_l(x)$ are defined as

$$h_l(x) = \frac{\ln x_{l+1} - \ln x}{\ln x_{l+1} - \ln x_l}, \quad (2.100)$$

$$g_l(x) = \frac{\ln x - \ln x_{l-1}}{\ln x_l - \ln x_{l-1}}. \quad (2.101)$$

2.5 Narrowband Bulk Scattering Properties

The single-scattering properties stored in the database cannot be directly applied to the satellite remote sensing due to the following reasons: First, dust aerosols in nature are not single-sized but polydispersed; Moreover, each channel of the satellite instruments have a spectral bandwidth, and the sensitivity of the instruments as well as the solar spectrum may vary with respect to the wavelength in the bandwidth. Therefore, we use the ensemble averaged single-scattering properties over a particle

size distribution $N(r)$, considering the solar spectrum $S(\lambda)$ at the TOA and the response function $f(\lambda)$ of a satellite instrument, i.e.

$$\langle C_{ext/sca/abs} \rangle = \frac{\int_{\lambda_1}^{\lambda_2} \int_{r_{min}}^{r_{max}} C_{ext/sca/sca}(r, \lambda) N(r) f(\lambda) S(\lambda) dr d\lambda}{\int_{\lambda_1}^{\lambda_2} \int_{r_{min}}^{r_{max}} N(r) f(\lambda) S(\lambda) dr d\lambda}, \quad (2.102)$$

$$\langle \mathbf{P}(\Theta) \rangle = \frac{\int_{\lambda_1}^{\lambda_2} \int_{r_{min}}^{r_{max}} C_{sca}(r, \lambda) \mathbf{P}(\Theta; r, \lambda) N(r) f(\lambda) S(\lambda) dr d\lambda}{\int_{\lambda_1}^{\lambda_2} \int_{r_{min}}^{r_{max}} C_{sca}(r, \lambda) N(r) f(\lambda) S(\lambda) dr d\lambda}. \quad (2.103)$$

These averaged single-scattering properties are the so-called narrowband bulk scattering properties.

Since we are interested in the multi-angular radiance and polarized measurements of the POLDER/PARASOL, the narrowband bulk scattering properties for the three channels that have the polarization capabilities are calculated. The response functions of the three channels, 490P, 670P, and 865P, are shown in Figure 2.6 along with the complex refractive index of Saharan dust aerosols. The particle size distribution is assumed to be in a mono-modal log-normal form,

$$\frac{dN(r)}{d \ln r} = \frac{1}{\delta \sqrt{2\pi}} \exp \left[-\frac{(\ln r - \ln \bar{r})^2}{2\delta^2} \right], \quad (2.104)$$

where \bar{r} is the mean radius and δ is the standard deviation. The sensitivity of satellite channels to dust aerosols can be inferred from the narrowband bulk scattering properties. Figure 2.7 shows elements, the phase function P_{11} and the polarized phase function P_{12} , of the narrowband bulk scattering phase matrix for the POLDER/PARASOL spectral bands 490P, 670P, and 865P, respectively, where the phase function is only shown at large scattering angles, since remote sensing of dust aerosols with space-borne satellite observations is more sensitive to the backward scattering. At backward scattering angles, where $\Theta > 90^\circ$, the bulk scattering phase

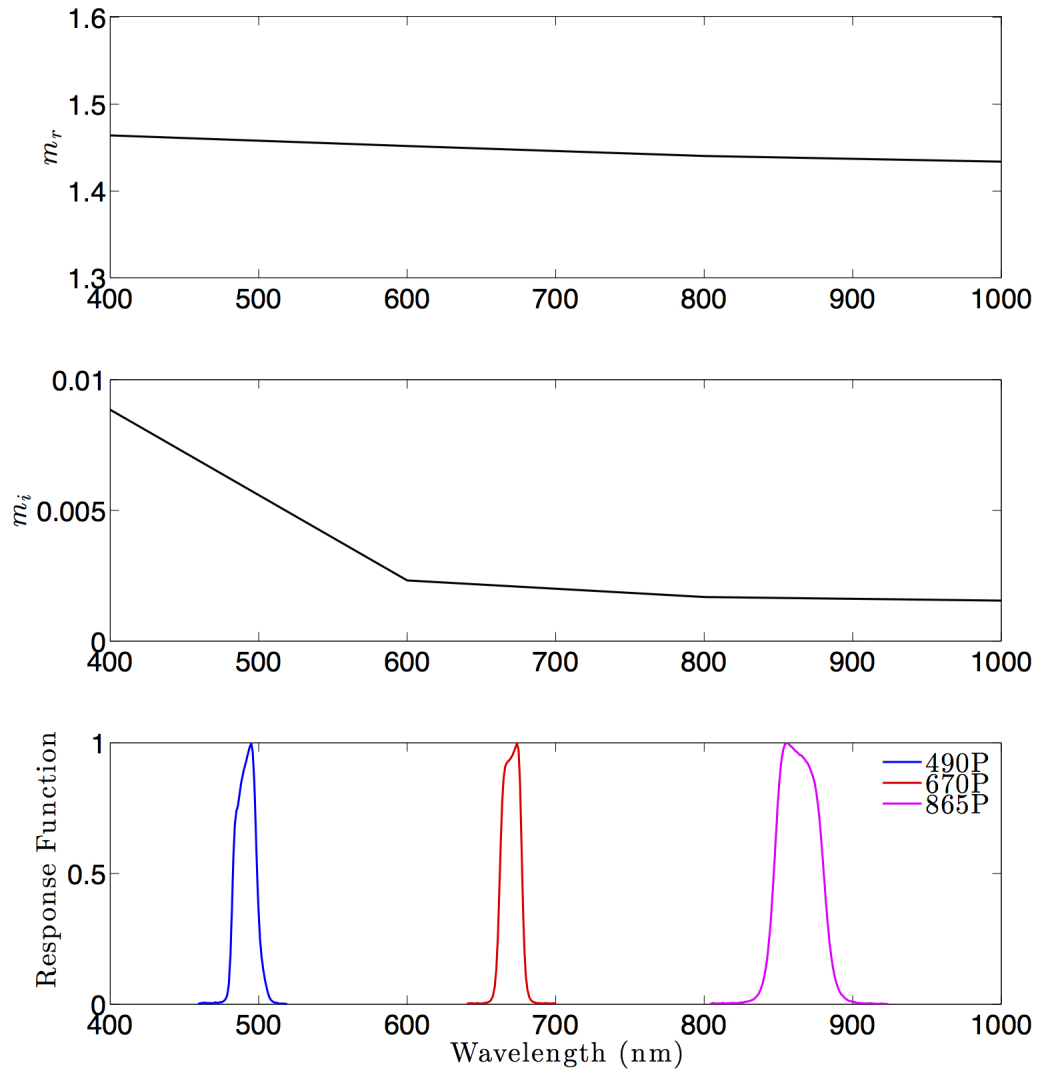


Figure 2.6: Real part and imaginary part of the complex refractive index of Saharan dust aerosol, and the response functions of the POLDER/PARASOL spectral bands 490P, 670P, and 865P versus wavelength. The refractive index data are taken from [49].

function for the band 670P shows significant angular features, which is similar with the scenario of the band 865P, while it is quite featureless for the band 490P. This phenomena is mainly due to the comparatively strong absorption of the Saharan dust aerosol in the near UV (UltraViolet) and deep blue spectrum. Moreover, it is obvious that multi-angular measurements are very sensitive to the microphysical properties including of the particle size and the aspect ratio. Furthermore, the distinguished angular features of the phase function and the polarized phase function implies that the combined multi-angular radiance and polarized measurements may relief the non-uniqueness problem that is facing in front of many satellite retrieval algorithms, and may greatly increase the number of retrievable parameters.

2.6 Summary

In this section, we studied the single-scattering properties of dust aerosols using the spheroidal model. As an effort for solving the problem of light scattering by a single spheroidal particle, we developed a new algorithm for the calculation of spheroidal functions. Using the newly developed single-scattering properties database of mineral dust aerosols, we obtained the narrowband bulk scattering properties of dust aerosols for satellite remote sensing, which would be used in our aerosol retrieval algorithm. When the aerosol optical thickness is large, single-scattering properties cannot be directly applied to aerosol retrieval, since then multiple scattering effects become dominant. In the following section, we will introduce how to take into account the multiple scattering among dust aerosols in the atmosphere with the knowledge of the single-scattering properties.

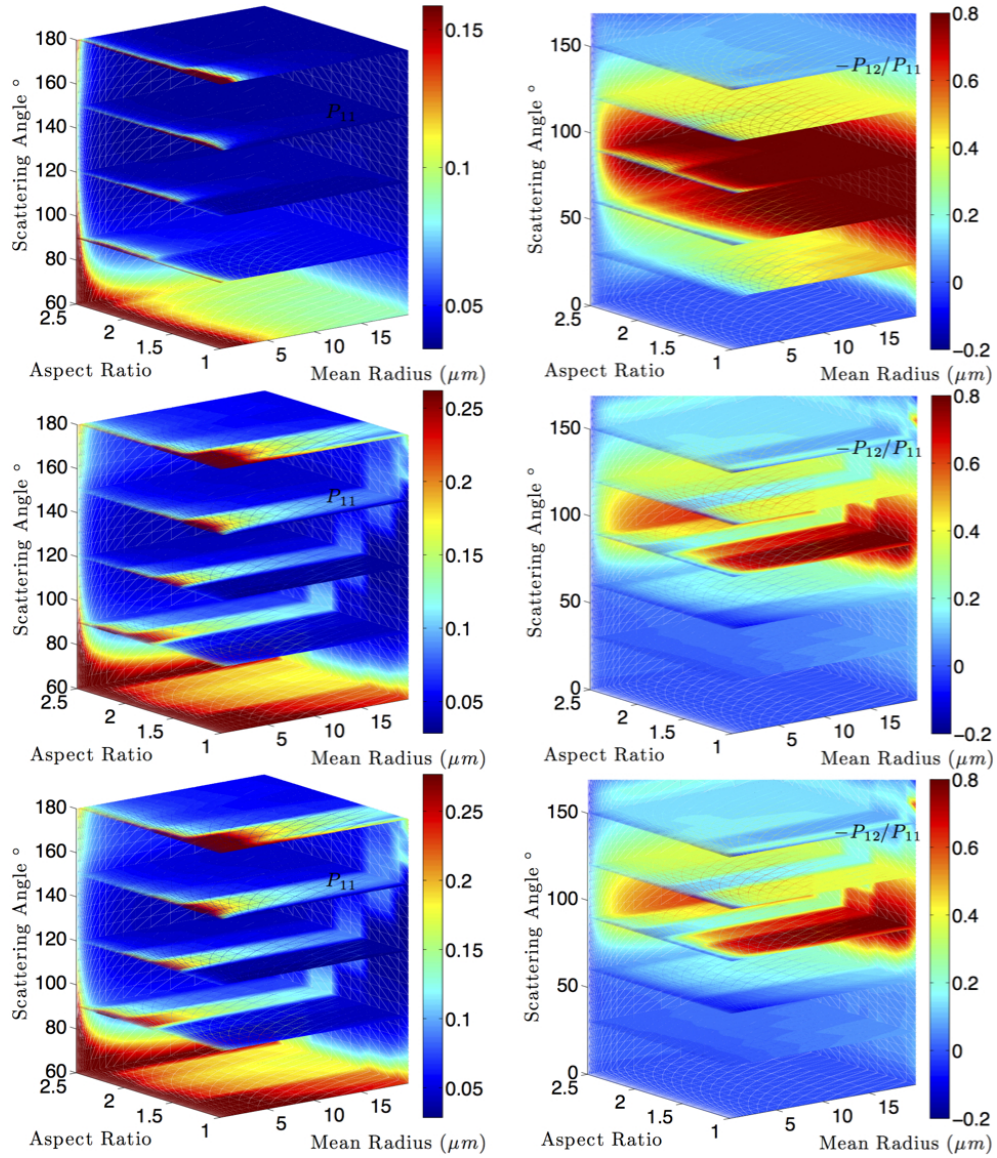


Figure 2.7: Comparison of elements P_{11} and P_{12} of the phase matrix of polydispersed spheroidal dust aerosols with aspect ratio ranged from 1.0 to 2.5 and mean radius ranged from 0.02 to 20.0 μm for the POLDER/PARASOL spectral bands 490P, 670P, and 865P. On the right column, the three panels are showing P_{11} s as functions of the scattering angle, the aspect ratio and the mean radius, for 490P, 670P, and 865P bands from top to bottom, respectively. On the left column, the three panels are showing $-P_{12}/P_{11}$ s as functions of the scattering angle, the aspect ratio and the mean radius, for 490P, 670P, and 865P bands from top to bottom, respectively. For each subgraph of the P_{11} , there are 5 slices at scattering angles of 60° , 90° , 120° , 150° , 180° . For each subgraph of the $-P_{12}/P_{11}$, there are 6 slices at scattering angles of 30° , 60° , 90° , 120° , 150° , 180° .

3. FORWARD RADIATIVE TRANSFER MODEL

3.1 Introduction

For the purpose of simulation of the solar light propagating in the atmosphere and the radiation field observed by a satellite, a forward radiative transfer model is required in the retrieval algorithm. We consider a forward model of a multilayer plane-parallel atmosphere above a surface (see Figure 3.1). Considering multiple scattering among dust aerosols and other atmospheric particles in such a forward model, one needs to solve the VRTE (vector radiative transfer equation). For a thin aerosol layer over ocean, radiation field in the forward model can be easily obtained by using the single-scattering properties of dust aerosols in the single-scattering approximation. Even if it is necessary to consider the multiple scattering, the VRTE can be solved effortlessly, due to the rather rapid convergence of the series expansion of the phase matrix in generalized spherical functions for the regularly shaped and small effective sized maritime aerosols. Moreover, since the ocean surface is dark for the visible channels, usually it can be treated like a black water body. If not, the reflection properties of an ocean surface are well studied and would not introduce many difficulties in the calculation. On the other hand, the simulation for optically thick aerosol layers over land requires considering much higher order-of-scattering terms, which would cost a huge amount of computational time. What is worse, land surface conditions are more complicated and diverse than that of the ocean surface. There is no unified model for reflection properties of the land surface. Lacking of an appropriate forward model for aerosol retrieval over land, many existing retrieval algorithms, which have been successfully applied to retrieve properties of maritime aerosols, encountered problems when applied to continental aerosol retrieval.

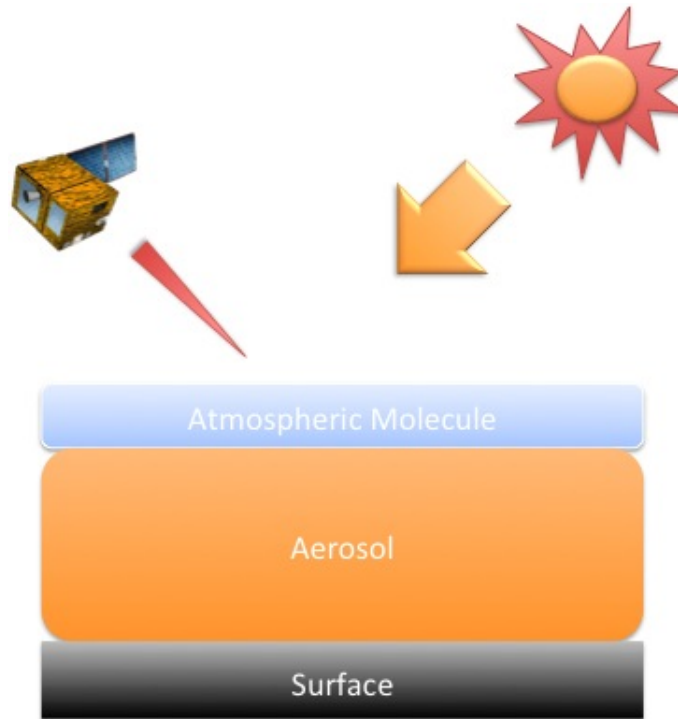


Figure 3.1: Schematic diagram of the forward model.

In this section, we develop a generalized forward radiative transfer model for the aerosol retrieval over land as well as over ocean. In order to address the aforementioned issues, we focus on two aspects: First, several improvements to the adding-doubling technique for efficiently solving the VRTE are studied; Second, a BRDF library is developed and imbedded into the adding-doubling code to account for reflection properties of various land and ocean surfaces.

The remaining part of this section is organized as follows: In the second subsection, the VRTE and other related concepts are introduced. In the third subsection, we provide a thorough introduction to our adding-doubling code from the theory to the numerical implementation. Different surface BRDFs and how to implement these BRDFs efficiently in the framework of the adding-doubling method are discussed in

Subsection 3.4. In the fifth subsection, a fast algorithm based on the icosahedral grid as an alternative to the rigorous adding-doubling method is presented. In the last subsection, we briefly summarize the works in this section.

3.2 Vector Radiative Transfer Equation for Plane-Parallel and Turbid Media

The multiple scattering of light by randomly and sparsely distributed discrete particles is governed by the VRTE. Generally, the VRTE in three dimensional space takes the form of

$$\hat{\mathbf{n}} \cdot \nabla \mathbf{I}(\mathbf{r}, \hat{\mathbf{n}}) = -N(\mathbf{r}) \langle \mathbf{K}(\mathbf{r}, \hat{\mathbf{n}}) \rangle \mathbf{I}(\mathbf{r}, \hat{\mathbf{n}}) + N(\mathbf{r}) \int_{4\pi} d\hat{\mathbf{n}}' \langle \tilde{\mathbf{Z}}(\mathbf{r}, \hat{\mathbf{n}}, \hat{\mathbf{n}}') \rangle \mathbf{I}(\mathbf{r}, \hat{\mathbf{n}}'), \quad (3.1)$$

where $N(\mathbf{r})$ is the number density of particles at position \mathbf{r} , $\hat{\mathbf{n}}$ is a unit vector in the propagation direction of the light, and \mathbf{K} is the 4×4 extinction matrix with the dimension of area, whose elements can be expressed in terms of the elements of the forward amplitude scattering matrix $\mathbf{S}(\hat{\mathbf{n}}^{inc}, \hat{\mathbf{n}}^{inc})$ as

$$\mathbf{K}(\hat{\mathbf{n}}^{inc}) = \frac{2\pi}{k_1} \begin{bmatrix} \text{Im}(S_{11} + S_{22}) & \text{Im}(S_{11} - S_{22}) & -\text{Im}(S_{12} + S_{21}) & -\text{Re}(S_{12} - S_{21}) \\ \text{Im}(S_{11} - S_{22}) & \text{Im}(S_{11} + S_{22}) & -\text{Im}(S_{12} - S_{21}) & -\text{Re}(S_{12} + S_{21}) \\ -\text{Im}(S_{12} + S_{21}) & \text{Im}(S_{12} - S_{21}) & \text{Im}(S_{11} + S_{22}) & -\text{Re}(S_{11} - S_{22}) \\ -\text{Re}(S_{12} - S_{21}) & \text{Re}(S_{12} + S_{21}) & \text{Re}(S_{11} - S_{22}) & \text{Im}(S_{11} + S_{22}) \end{bmatrix}, \quad (3.2)$$

with the wavenumber in the host medium k_1 . The sign $\langle \dots \rangle$ means the ensemble averaged optical characteristics over the varying particle states. Although the definition of the phase matrix $\tilde{\mathbf{Z}}$ keeps the same as that in the previous section, it should be noticed that the no-tilde Stokes vector I here is in the unit of radiance instead of irradiance (or flux), since it is more natural to describe the scattered light in terms of radiance that would not attenuate with a factor of $1/r^2$, e.g. $\mathbf{I}^{sca} = \tilde{\mathbf{Z}}(\hat{\mathbf{n}}^{sca}, \hat{\mathbf{n}}^{inc}) \mathbf{I}^{inc}$

compared to equation (2.34).

The general three-dimensional integro-differential VRTE can hardly be solved with an efficient analytical or numerical method. Fortunately, in order to model polarized light propagating in the atmosphere in the analyses of satellite measurements, several assumptions can be made to simplify the problem. First, considering the distance between the sun and the earth, the sunlight can be assumed to be a parallel beam of light with infinite lateral extent. Second, considering the limitation of the observation geometry of a satellite, we usually take into account only those measurements with viewing zenith angles and the solar zenith angles close to zero (near the local zenith). Thus, the scattering medium, namely the atmosphere, can be assumed to be plane parallel and has an infinite horizontal extent.

Under these assumptions, all properties of the scattering medium and the radiation field vary only in the vertical direction and are independent of the horizontal coordinates. When dealing with the radiation field in such an one-dimensional system, it is convenient to use a laboratory right-handed coordinate system with the z -axis perpendicular to the boundaries of layers of the atmosphere and directed upwards, such that $\hat{\mathbf{n}} = (\sin \theta \cos \phi, \sin \theta \sin \phi, \cos \theta)$. The VRTE is reduced to the one-dimensional form:

$$\begin{aligned} \cos \theta \frac{d\mathbf{I}(z; \theta, \phi)}{dz} = & -N(z)\mathbf{K}(z; \theta, \phi)\mathbf{I}(z; \theta, \phi) \\ & + N(z) \int_0^{2\pi} d\phi' \int_0^\pi d\theta' \sin \theta' \langle \tilde{\mathbf{Z}}(z; \theta, \phi; \theta', \phi') \rangle \mathbf{I}(z; \theta', \phi'), \end{aligned} \quad (3.3)$$

where the Stokes vector \mathbf{I} as well as the phase matrix $\langle \tilde{\mathbf{Z}} \rangle$ are defined with respect to the meridian plane (whose normal vector is perpendicular to the unit vectors $\hat{\mathbf{n}}$ and $\hat{\mathbf{z}}$).

Due to the relatively small size, dust aerosols are usually randomly oriented in

the atmosphere so that the dust aerosol layer can be assumed to be isotropic. For further simplification, it can be assumed that each aerosol particle has a plane of symmetry (which is consistent with the spheroidal model of the dust aerosol). Under this circumstance, the extinction matrix becomes a diagonal matrix with all the four diagonal elements equal to C_{ext} . It is also preferred to introduce the normalized phase matrix in the meridian plane

$$\mathbf{Z}(z; \theta, \theta', \phi - \phi') = \frac{4\pi}{C_{sca}} \langle \tilde{\mathbf{Z}}(z; \theta, \theta', \phi - \phi') \rangle = \frac{4\pi}{\omega C_{ext}} \langle \tilde{\mathbf{Z}}(z; \theta, \theta', \phi - \phi') \rangle. \quad (3.4)$$

Here, the normalized phase matrix in the meridian plane $\mathbf{Z}(\theta, \theta', \phi - \phi')$ is related to the normalized phase matrix $P(\Theta)$ in the scattering plane in the following way

$$\mathbf{Z}(\theta, \theta', \phi - \phi') = \begin{cases} \mathbf{L}(\pi - \sigma_2) \mathbf{P}(\Theta) \mathbf{L}(-\sigma_1) & \text{if } 0 < \phi - \phi' < \pi \\ \mathbf{L}(\sigma_2 - \pi) \mathbf{P}(\Theta) \mathbf{L}(\sigma_1) & \text{if } 0 < \phi' - \phi < \pi \end{cases}, \quad (3.5)$$

where \mathbf{L} is defined in the equation (2.33), and σ_1 and σ_2 are the angles between the scattering plane and the meridian plane at ϕ' and ϕ , respectively. The angles σ_1 , σ_2 , and the scattering angle Θ can be calculated from θ , θ' , ϕ , and ϕ' using spherical trigonometry:

$$\cos \sigma_1 = \frac{\cos \theta - \cos \theta' \cos \Theta}{\sin \theta' \sin \Theta}, \quad (3.6)$$

$$\cos \sigma_2 = \frac{\cos \theta' - \cos \theta \cos \Theta}{\sin \theta \sin \Theta}, \quad (3.7)$$

$$\cos \Theta = \cos \theta \cos \theta' + \sin \theta \sin \theta' \cos(\phi - \phi'). \quad (3.8)$$

Therefore, the VRTE can be further simplified as

$$u \frac{\mathbf{I}(\boldsymbol{\tau}; u, \phi)}{d\boldsymbol{\tau}} = -\mathbf{I}(\boldsymbol{\tau}; u, \phi) + \frac{\omega(\boldsymbol{\tau})}{4\pi} \int_0^{2\pi} d\phi' \int_{-1}^{+1} du' \mathbf{Z}(\boldsymbol{\tau}; u, u', \phi - \phi') \mathbf{I}(\boldsymbol{\tau}; u', \phi'), \quad (3.9)$$

where $u = -\cos\theta \in [-1, +1]$, and

$$\tau(z) = \int_z^\infty dz' N(z') C_{ext}(z'), \quad (3.10)$$

is the so-called dimensionless optical depth (or thickness). If the thermal emission in the atmosphere can be ignored, as is true for the visible spectrum, equation (3.9) forms the standard problem of the atmospheric optics ([37]) by supplementing with the boundary conditions

$$\mathbf{I}(0; u, \phi) = \delta(u - u_0)\delta(\phi - \phi_0)\mathbf{F}_0 \quad \text{for } u > 0, \quad (3.11)$$

$$\mathbf{I}(\tau_B; u, \phi) = \mathbf{0} \quad \text{for } u < 0, \quad (3.12)$$

where \mathbf{F}_0 is the Stokes vector of the incident solar flux, $u_0 > 0$ is equal to the cosine of solar zenith angle and ϕ is the azimuth angle of the sun. Here, we have assumed that the earth surface (or the lower boundary of the scattering medium) at $\tau = \tau_B$ is acting like a black body for simplicity.

In order to solve the integro-differential VRTE, people have been seeking for an efficient algorithm for decades, resulting in many computational methods. For the Rayleigh scattering phase matrix, Chandrasekhar has found the analytical solution to the VRTE in 1960 ([4]). For an arbitrary phase matrix, there is no analytical solution in general. However, some semi-analytical methods have been developed, such as the invariant imbedding method ([1]), the SOS (Successive Order of Scattering method, [64]), and the adding-doubling method ([16]). There are also some numerical methods, such as the Monte-Carlo method ([63]) and the VDISORT (vector discrete ordinate method, [44]). Since our aim is to find a method that is suitable for the repeatedly calculation in an iterative aerosol retrieval algorithm, the time-consuming

numerical methods have to be abandoned even though they are irreplaceable when considering a more complicated problem, such as the three-dimensional VRTE. Although the invariant imbedding method is preferred when generating a LUT for the reason that it can obtain solutions to the VRTE for a series of optical thicknesses τ_B within one run, such an advantage becomes less important for the aerosol retrieval. The SOS is the most widely used solver for the forward model in aerosol retrievals, because the order-of-scattering expansion provides physical insight crucial for understanding the process of multiple scattering. In addition, the order-of-scattering expansion converges rapidly since the usual optical depth of atmospheric aerosol layer is relatively small (e.g., $\tau_B < 1$). However, considering almost non-absorbing dust aerosols in the visible spectrum over the source region or in the dust storm season, the contribution of higher order terms then becomes significant, since the aerosol slab is nearly conservative (e.g., $\omega \simeq 1$) and optically thick (e.g., $\tau_B > 1$). Due to its comparatively high efficiency when dealing with large optical thickness, we adopt the adding-doubling technique to solve the VRTE in this study.

3.3 The Adding-Doubling Technique

It is convenient to use $\mu = |u| \in [0, 1]$ to distinguish the upward radiation field $\mathbf{I}(\tau, -\mu, \phi)$ and the downward radiation field $\mathbf{I}(\tau, \mu, \phi)$. The general solution to the equation (3.9) can then be expressed by

$$\begin{aligned}
\mathbf{I}(\tau; \mu, \phi) &= \exp\left(-\frac{\tau}{\mu}\right)\mathbf{I}(0; \mu, \phi) \\
&+ \frac{1}{\pi} \int_0^{2\pi} d\phi' \int_0^{+1} d\mu' \mu' \mathbf{D}(\tau; \mu, \mu', \phi - \phi') \mathbf{I}(0; \mu', \phi') \\
&+ \frac{1}{\pi} \int_0^{2\pi} d\phi' \int_0^{+1} d\mu' \mu' \mathbf{U}^*(\tau; \mu, \mu', \phi - \phi') \mathbf{I}(\tau_B; -\mu', \phi'),
\end{aligned} \tag{3.13}$$

$$\begin{aligned}
\mathbf{I}(\boldsymbol{\tau}; -\mu, \phi) &= \exp\left(-\frac{\tau_B - \tau}{\mu}\right) \mathbf{I}(\tau_B; -\mu, \phi) \\
&+ \frac{1}{\pi} \int_0^{2\pi} d\phi' \int_0^{+1} d\mu' \mu' \mathbf{U}(\boldsymbol{\tau}; \mu, \mu', \phi - \phi') \mathbf{I}(0; \mu', \phi') \\
&+ \frac{1}{\pi} \int_0^{2\pi} d\phi' \int_0^{+1} d\mu' \mu' \mathbf{D}^*(\boldsymbol{\tau}; \mu, \mu', \phi - \phi') \mathbf{I}(\tau_B; -\mu', \phi'),
\end{aligned} \tag{3.14}$$

where the 4×4 matrices $\mathbf{U}(\boldsymbol{\tau}; \mu, \mu', \phi - \phi')$ and $\mathbf{D}(\boldsymbol{\tau}; \mu, \mu', \phi - \phi')$ describe the response of the atmosphere to the radiation field incident on the upper boundary from above for the downward and upward scattered light, respectively; The 4×4 matrices $\mathbf{U}^*(\boldsymbol{\tau}; \mu, \mu', \phi - \phi')$ and $\mathbf{D}^*(\boldsymbol{\tau}; \mu, \mu', \phi - \phi')$ describe the response of the atmosphere to the radiation field illuminating the bottom boundary from below for the downward and upward scattered light, respectively. The first terms on the right hand side of equations (3.14) and (3.14) describe the direct light, whereas the remaining terms describe the diffused light due to multiple scattering.

The boundary values of \mathbf{U} , \mathbf{U}^* , \mathbf{D} , \mathbf{D}^* are known as the reflection and transmission matrices, which determine the Stokes vectors of the radiation emerging from the atmosphere, i.e.

$$\mathbf{R}(\mu, \mu', \phi - \phi') = \mathbf{U}(0; \mu, \mu', \phi - \phi'), \tag{3.15}$$

$$\mathbf{T}(\mu, \mu', \phi - \phi') = \mathbf{D}(\tau_B; \mu, \mu', \phi - \phi'), \tag{3.16}$$

$$\mathbf{R}^*(\mu, \mu', \phi - \phi') = \mathbf{U}^*(\tau_B; \mu, \mu', \phi - \phi'), \tag{3.17}$$

$$\mathbf{T}^*(\mu, \mu', \phi - \phi') = \mathbf{D}^*(0; \mu, \mu', \phi - \phi'). \tag{3.18}$$

Therefore, the solution to the standard problem where the sunlight is incident at the

top of the planetary atmosphere bottomed by a black surface, takes the form:

$$\begin{aligned} \mathbf{I}(\tau; \mu, \phi) &= \delta(\mu - \mu_0)\delta(\phi - \phi_0) \exp\left(-\frac{\tau}{\mu_0}\right)\mathbf{F}_0 \\ &+ \frac{1}{\pi}\mu_0\mathbf{D}(\tau; \mu, \mu_0, \phi - \phi_0)\mathbf{F}_0, \end{aligned} \quad (3.19)$$

$$\mathbf{I}(\tau; -\mu, \phi) = \frac{1}{\pi}\mu_0\mathbf{U}(\tau; \mu, \mu_0, \phi - \phi_0)\mathbf{F}_0, \quad (3.20)$$

$$\begin{aligned} \mathbf{I}(\tau_B; \mu, \phi) &= \delta(\mu - \mu_0)\delta(\phi - \phi_0) \exp\left(-\frac{\tau_B}{\mu_0}\right)\mathbf{F}_0 \\ &+ \frac{1}{\pi}\mu_0\mathbf{T}(\mu, \mu_0, \phi - \phi_0)\mathbf{F}_0, \end{aligned} \quad (3.21)$$

$$\mathbf{I}(0; -\mu, \phi) = \frac{1}{\pi}\mu_0\mathbf{R}(\mu, \mu_0, \phi - \phi_0)\mathbf{F}_0. \quad (3.22)$$

3.3.1 Adding Equations

The adding-doubling technique is an efficient way to calculate \mathbf{U} , \mathbf{U}^* , \mathbf{D} , \mathbf{D}^* , \mathbf{R} , \mathbf{R}^* , \mathbf{T} , \mathbf{T}^* . For a sketch of the idea of adding-doubling, we consider two plane-parallel atmospheric layers, one with optical depth τ on top of the other one with optical depth $\tau_B - \tau$. For simplicity, define “*” product and the direct transmission matrix \mathbf{E} as

$$\begin{aligned} \mathbf{W}(\mu, \mu', \phi - \phi') &= \frac{1}{\pi} \int_0^{2\pi} d\phi'' \int_0^1 d\mu'' \mu'' \mathbf{X}(\mu, \mu'', \phi - \phi'') \mathbf{Y}(\mu'', \mu', \phi'' - \phi') \\ &= \mathbf{X}(\mu, \mu'', \phi - \phi'') * \mathbf{Y}(\mu'', \mu', \phi'' - \phi'), \\ \mathbf{E}(\tau; \mu, \mu', \phi - \phi') &= \frac{\pi}{\mu'} \delta(\mu - \mu') \delta(\phi - \phi') \exp\left(\frac{\tau}{\mu'}\right) \mathbf{1}. \end{aligned} \quad (3.23)$$

where $\mathbf{1} = \text{diag}(1, 1, 1, 1)$

If the reflection and transmission properties \mathbf{R} , \mathbf{R}^* , \mathbf{T} , \mathbf{T}^* of each of the layers are known, the reflection and transmission properties of the combined layer can be

calculated by the so-called adding method using the adding equations as follows:

$$\mathbf{Q}^{(1)}(\mu, \mu', \phi - \phi') = \mathbf{R}_1^*(\mu, \mu'', \phi - \phi'') * \mathbf{R}_2(\mu'', \mu', \phi'' - \phi'), \quad (3.25)$$

$$\mathbf{Q}^{(p+1)}(\mu, \mu', \phi - \phi') = \mathbf{Q}^{(1)}(\mu, \mu'', \phi - \phi'') * \mathbf{Q}^{(p)}(\mu'', \mu', \phi'' - \phi'), \quad (3.26)$$

$$\mathbf{Q}(\mu, \mu', \phi - \phi') = \sum_{p=1}^{\infty} \mathbf{Q}^{(p)}(\mu, \mu', \phi - \phi'), \quad (3.27)$$

$$\begin{aligned} \mathbf{D}(\tau; \mu, \mu', \phi - \phi') &= \mathbf{T}_1(\mu, \mu', \phi - \phi') \\ &+ \mathbf{Q}(\mu, \mu'', \phi - \phi'') * \mathbf{E}(\tau; \mu'', \mu', \phi'' - \phi') \\ &+ \mathbf{Q}(\mu, \mu'', \phi - \phi'') * \mathbf{T}_1(\mu'', \mu', \phi'' - \phi'), \end{aligned} \quad (3.28)$$

$$\begin{aligned} \mathbf{U}(\tau; \mu, \mu', \phi - \phi') &= \mathbf{R}_2(\mu, \mu'', \phi - \phi'') * \mathbf{E}(\tau; \mu'', \mu', \phi'' - \phi') \\ &+ \mathbf{R}_2(\mu, \mu'', \phi - \phi'') * \mathbf{D}(\tau; \mu'', \mu', \phi'' - \phi'), \end{aligned} \quad (3.29)$$

$$\begin{aligned} \mathbf{U}^*(\tau; \mu, \mu', \phi - \phi') &= \mathbf{R}_1^*(\mu, \mu'', \phi - \phi'') * \mathbf{E}(\tau_B - \tau; \mu'', \mu', \phi'' - \phi') \\ &+ \mathbf{R}_1^*(\mu, \mu'', \phi - \phi'') * \mathbf{T}_2^*(\mu'', \mu', \phi'' - \phi') \\ &+ \mathbf{Q}(\mu, \mu''', \phi - \phi''') * \mathbf{R}_1^*(\mu''', \mu'', \phi''' - \phi'') * \mathbf{E}(\tau_B - \tau; \mu'', \mu', \phi'' - \phi') \\ &+ \mathbf{Q}(\mu, \mu''', \phi - \phi''') * \mathbf{R}_1^*(\mu''', \mu'', \phi''' - \phi'') * \mathbf{T}_2^*(\mu'', \mu', \phi'' - \phi'), \end{aligned} \quad (3.30)$$

$$\begin{aligned} \mathbf{D}^*(\tau; \mu, \mu', \phi - \phi') &= \mathbf{T}_2^*(\mu, \mu'', \phi - \phi'') \\ &+ \mathbf{R}_2(\mu, \mu'', \phi - \phi'') * \mathbf{U}^*(\tau; \mu'', \mu', \phi'' - \phi'), \end{aligned} \quad (3.31)$$

$$\begin{aligned} \mathbf{R}(\mu, \mu', \phi - \phi') &= \mathbf{R}_1(\mu, \mu', \phi - \phi') \\ &+ \mathbf{E}(\tau; \mu, \mu'', \phi - \phi'') * \mathbf{U}(\tau; \mu'', \mu', \phi'' - \phi') \\ &+ \mathbf{T}_1^*(\mu, \mu'', \phi - \phi'') * \mathbf{U}(\tau; \mu'', \mu', \phi'' - \phi'), \end{aligned} \quad (3.32)$$

$$\begin{aligned} \mathbf{T}(\mu, \mu', \phi - \phi') &= \mathbf{E}(\tau_B - \tau; \mu, \mu'', \phi - \phi'') * \mathbf{D}(\tau; \mu'', \mu', \phi'' - \phi') \\ &+ \mathbf{T}_2(\mu, \mu', \phi - \phi') * \mathbf{E}(\tau; \mu'', \mu', \phi'' - \phi') \\ &+ \mathbf{T}_2(\mu, \mu'', \phi - \phi'') * \mathbf{D}(\tau; \mu'', \mu', \phi'' - \phi'), \end{aligned} \quad (3.33)$$

$$\begin{aligned} \mathbf{R}^*(\mu, \mu', \phi - \phi') &= \mathbf{R}_2^*(\mu, \mu', \phi - \phi') \\ &+ \mathbf{E}(\tau_B - \tau; \mu, \mu'', \phi - \phi'') * \mathbf{U}^*(\tau; \mu'', \mu', \phi'' - \phi') \end{aligned} \quad (3.34)$$

$$+ \mathbf{T}_2(\mu, \mu'', \phi - \phi'') * \mathbf{U}^*(\tau; \mu'', \mu', \phi'' - \phi'),$$

$$\begin{aligned} \mathbf{T}^*(\mu, \mu', \phi - \phi') &= \mathbf{E}(\tau; \mu, \mu'', \phi - \phi'') * \mathbf{D}^*(\tau; \mu'', \mu', \phi'' - \phi') \\ &+ \mathbf{T}_1^*(\mu, \mu', \phi - \phi') * \mathbf{E}(\tau_B - \tau; \mu'', \mu', \phi'' - \phi') \end{aligned} \quad (3.35)$$

$$+ \mathbf{T}_1^*(\mu, \mu'', \phi - \phi'') * \mathbf{D}^*(\tau; \mu'', \mu', \phi'' - \phi'),$$

Adding two identical homogeneous layers leads to the so-called doubling method. To calculate the scattering properties of a homogeneous atmospheric layer, we choose the initial layer to be so thin that the reflection and transmission properties can be described with sufficient accuracy by considering the first or second order of scattering only, i.e. using the reflection and transmission matrices of an infinitesimally thin layer with optical depth $\Delta\tau \rightarrow 0$:

$$\mathbf{R}_{\Delta\tau}(\mu, \mu', \phi - \phi') = \frac{\omega\Delta\tau}{4\mu\mu'} \mathbf{Z}(-\mu, \mu', \phi - \phi'), \quad (3.36)$$

$$\mathbf{T}_{\Delta\tau}(\mu, \mu', \phi - \phi') = \frac{\omega\Delta\tau}{4\mu\mu'} \mathbf{Z}(\mu, \mu', \phi - \phi'), \quad (3.37)$$

$$\mathbf{R}_{\Delta\tau}^*(\mu, \mu', \phi - \phi') = \frac{\omega\Delta\tau}{4\mu\mu'} \mathbf{Z}(\mu, -\mu', \phi - \phi'), \quad (3.38)$$

$$\mathbf{T}_{\Delta\tau}^*(\mu, \mu', \phi - \phi') = \frac{\omega\Delta\tau}{4\mu\mu'} \mathbf{Z}(-\mu, -\mu', \phi - \phi'). \quad (3.39)$$

By using the adding equations (3.25)-(3.35) repeatedly, each time we obtain the scattering properties of a layer with the doubled optical thickness until a certain desired optical thickness is reached. It is worthwhile to notice that when applying the adding equations to such homogeneous layers, instead of using the equations (3.35) and (3.35), we may find the \mathbf{R}^* , \mathbf{T}^* through the following symmetry relations

to reduce the computation burden:

$$\mathbf{R}^*(\mu, \mu', \phi - \phi') = \mathbf{R}(\mu, \mu', \phi' - \phi), \quad (3.40)$$

$$\mathbf{T}^*(\mu, \mu', \phi - \phi') = \mathbf{T}(\mu, \mu', \phi' - \phi), \quad (3.41)$$

which are valid if the scattering medium is composed of randomly oriented mirror-symmetric particles. Since the optical depth is increasing exponentially in the doubling process, it is rather efficient to derive the scattering properties of optically thick aerosol layers.

3.3.2 Fourier Transformation

By expanding each function of the azimuthal angle in the adding equations into a Fourier series, integrations over the azimuthal angle can be eliminated. If a matrix $\mathbf{X}(\mu, \mu', \phi - \phi')$ obeys the symmetry relation:

$$\mathbf{X}(\mu, \mu', \phi - \phi') = \mathbf{\Delta} \mathbf{X}(\mu, \mu', \phi' - \phi) \mathbf{\Delta}, \quad (3.42)$$

which is true for any matrices in the adding equations as well as the phase matrix \mathbf{Z} if the particles in the scattering medium are randomly oriented and mirror-symmetric, then the matrix can be expanded as follows:

$$\begin{aligned} \mathbf{X}(\mu, \mu', \phi - \phi') = \frac{1}{2} \sum_{m=0}^{\infty} (2 - \delta_{m,0}) \times & [\mathbf{B}^{+m}(\phi - \phi') \mathbf{X}^m(\mu, \mu') (\mathbf{1} + \mathbf{\Delta}) \\ & + \mathbf{B}^{-m}(\phi - \phi') \mathbf{X}^m(\mu, \mu') (\mathbf{1} - \mathbf{\Delta})], \end{aligned} \quad (3.43)$$

where

$$\mathbf{\Delta} = \text{diag}(1, 1, -1, -1), \quad (3.44)$$

$$\mathbf{B}^{+m}(\phi) = \text{diag}(\cos m\phi, \cos m\phi, \sin m\phi, \sin m\phi), \quad (3.45)$$

$$\mathbf{B}^{-m}(\phi) = \text{diag}(-\sin m\phi, -\sin m\phi, \cos m\phi, \cos m\phi), \quad (3.46)$$

and the m -th Fourier component

$$\mathbf{X}^m(\mu, \mu') = \frac{1}{2\pi} \int_0^{2\pi} d(\phi - \phi') [\mathbf{B}^{+m}(\phi - \phi') + \mathbf{B}^{-m}(\phi - \phi')] \mathbf{X}(\mu, \mu', \phi - \phi'). \quad (3.47)$$

Then the integration over the azimuthal angle in the equation (3.23) disappears after taking the Fourier transformation, and for each component we have

$$\mathbf{W}^m(\mu, \mu') = 2 \int_0^1 d\mu'' \mu'' \mathbf{X}^m(\mu, \mu'') \mathbf{Y}^m(\mu'', \mu'). \quad (3.48)$$

For the phase matrix in meridian plane, the m -th Fourier component can be calculated using an elegant addition theorem for the generalized spherical functions ([16]). For example,

$$\begin{aligned} \mathbf{Z}^m(\pm\mu, \mu') &= \frac{1}{2\pi} \int_0^{2\pi} d(\phi - \phi') [\mathbf{B}^{+m}(\phi - \phi') + \mathbf{B}^{-m}(\phi - \phi')] \mathbf{Z}(\pm\mu, \mu', \phi - \phi') \\ &= (-1)^m \sum_{l=m}^{\infty} \mathbf{P}_m^l(\pm\mu) \mathbf{S}^l \mathbf{P}_m^l(\mu'), \end{aligned} \quad (3.49)$$

where the matrix $\mathbf{P}_m^l(\pm\mu)$ is

$$\mathbf{P}_m^l(\mu) = \begin{pmatrix} P_{m,0}^l(\mu) & 0 & 0 & 0 \\ 0 & \frac{1}{2}[P_{m,-2}^l(\mu) + P_{m,+2}^l(\mu)] & \frac{1}{2}[P_{m,-2}^l(\mu) - P_{m,+2}^l(\mu)] & 0 \\ 0 & \frac{1}{2}[P_{m,-2}^l(\mu) - P_{m,+2}^l(\mu)] & \frac{1}{2}[P_{m,-2}^l(\mu) + P_{m,+2}^l(\mu)] & 0 \\ 0 & 0 & 0 & P_{m,0}^l(\mu) \end{pmatrix}. \quad (3.50)$$

Here, the functions $P_{m,0}^l(\mu)$ and $P_{m,\pm 2}^l(\mu)$ are the generalized spherical functions. The matrix \mathbf{S}^l could be written as

$$\mathbf{S}^l = \begin{pmatrix} \alpha_1^l & \beta_1^l & 0 & 0 \\ \beta_1^l & \alpha_2^l & 0 & 0 \\ 0 & 0 & \alpha_3^l & \beta_2^l \\ 0 & 0 & -\beta_2^l & \alpha_4^l \end{pmatrix}, \quad (3.51)$$

whose elements are the expansion coefficients of the elements of the phase matrix in scattering plane into the generalized spherical functions:

$$a_1(\Theta) = \sum_{l=0}^{\infty} \alpha_1^l P_{0,0}^l(\cos \Theta), \quad (3.52)$$

$$a_2(\Theta) + a_3(\Theta) = \sum_{l=2}^{\infty} (\alpha_2^l + \alpha_3^l) P_{2,+2}^l(\cos \Theta), \quad (3.53)$$

$$a_2(\Theta) - a_3(\Theta) = \sum_{l=2}^{\infty} (\alpha_1^l - \alpha_3^l) P_{2,-2}^l(\cos \Theta), \quad (3.54)$$

$$a_4(\Theta) = \sum_{l=0}^{\infty} \alpha_4^l P_{0,0}^l(\cos \Theta), \quad (3.55)$$

$$b_1(\Theta) = \sum_{l=2}^{\infty} \beta_1^l P_{0,+2}^l(\cos \Theta), \quad (3.56)$$

$$b_2(\Theta) = \sum_{l=2}^{\infty} \beta_2^l P_{0,+2}^l(\cos \Theta). \quad (3.57)$$

Since for a given m and n , the generalized spherical functions $P_{mn}^l(x)$ with $s \geq \max(|m|, |n|)$ form a complete orthonormal set of functions on the interval $x \in [-1, 1]$, the following orthogonality relation is satisfied:

$$\int_{-1}^{+1} d\mu P_{mn}^l(\mu) P_{mn}^{l'}(\mu) = \frac{2}{2l+1} (-1)^{m+n} \delta_{ll'}. \quad (3.58)$$

Therefore, we have the following expression for the elements of \mathbf{S}^l :

$$\alpha_1^l = (l + \frac{1}{2}) \int_{-1}^{+1} d(\cos \Theta) P_{00}^l(\cos \Theta) a_1(\Theta), \quad (3.59)$$

$$\alpha_2^l + \alpha_3^l = (l + \frac{1}{2}) \int_{-1}^{+1} d(\cos \Theta) P_{2,+2}^l(\cos \Theta) [a_2(\Theta) + a_3(\Theta)], \quad (3.60)$$

$$\alpha_2^l - \alpha_3^l = (l + \frac{1}{2}) \int_{-1}^{+1} d(\cos \Theta) P_{2,-2}^l(\cos \Theta) [a_2(\Theta) - a_3(\Theta)], \quad (3.61)$$

$$\alpha_4^l = (l + \frac{1}{2}) \int_{-1}^{+1} d(\cos \Theta) P_{00}^l(\cos \Theta) a_4(\Theta), \quad (3.62)$$

$$\beta_1^l = (l + \frac{1}{2}) \int_{-1}^{+1} d(\cos \Theta) P_{0,+2}^l(\cos \Theta) b_1(\Theta), \quad (3.63)$$

$$\beta_2^l = (l + \frac{1}{2}) \int_{-1}^{+1} d(\cos \Theta) P_{0,+2}^l(\cos \Theta) b_2(\Theta). \quad (3.64)$$

3.3.3 Adding-Doubling in Supermatrices Form

After applying the Fourier transformation, integrations over the azimuthal angle disappear in the adding equations. What remained are those integrations over the polar angle (see the equation (3.48)), which can be evaluated numerically using Gaussian quadrature. If the total number of the considered Gaussian quadrature is n , then

$$\mathbf{W}^m(\mu_i, \mu_j) = 2 \sum_{k=1}^n \mu_k w_k \mathbf{X}^m(\mu_i, \mu_k) \mathbf{Y}^m(\mu_k, \mu_j) \quad \text{for } i, j = 1, 2, \dots, n, \quad (3.65)$$

where μ_i and w_i are the i th Gaussian division point and the corresponding weight on the interval (0,1), respectively.

In the simulation of satellite observations, we want not only the results on the Gaussian division points but also those on the angles for which measurements are available. Let us supplement the Gaussian division points $\{\mu_i, i = 1, 2, \dots, n\}$ with

these interested points $\{\mu_i, i = n, n + 1, \dots, N\}$. Then the equation (3.65) becomes

$$\mathbf{W}^m(\mu_i, \mu_j) = 2 \sum_{k=1}^n \mu_k w_k \mathbf{X}^m(\mu_i, \mu_k) \mathbf{Y}^m(\mu_k, \mu_j) \quad \text{for } i, j = 1, 2, \dots, n, n + 1, \dots, N. \quad (3.66)$$

Now let us introduce the $N \times N$ supermatrix \mathbf{X} with each element in the form of a 4×4 submatrix:

$$\mathbf{X}_{i,j}^m = c_i \mathbf{X}^m(\mu_i, \mu_j) c_j \quad \text{for } i, j = 1, 2, \dots, n, n + 1, \dots, N, \quad (3.67)$$

where

$$c_i = \begin{cases} \sqrt{2w_i \mu_i} & \text{for } i = 1, 2, \dots, n \\ 1 & \text{for } i = n, n + 1, \dots, N \end{cases}. \quad (3.68)$$

Therefore, the equation (3.66) can be written in the form of a multiplication of two supermatrices as follows:

$$\mathbf{W}_{i,j}^m = \sum_{k=1}^n \mathbf{X}_{i,k}^m \mathbf{Y}_{k,j}^m \quad \text{for } i, j = 1, 2, \dots, n, n + 1, \dots, N. \quad (3.69)$$

For simplicity, we omit the summation sign and those subscripts in the equation (3.69), based on which we define the supermatrix product

$$\mathbf{W}^m = \mathbf{X}^m \mathbf{Y}^m. \quad (3.70)$$

Note that the equation (3.70) is not the actual matrix product, but a simplification for the equation (3.69).

The adding equations after Fourier decomposition then can be expressed in terms

of supermatrices. For each Fourier component, we have

$$\mathbf{Q}^{(1)} = \mathbf{R}_1^* \mathbf{R}_2, \quad (3.71)$$

$$\mathbf{Q}^{(p+1)} = \mathbf{Q}^{(1)} \mathbf{Q}^{(p)}, \quad (3.72)$$

$$\mathbf{Q} = \sum_{p=1}^{\infty} \mathbf{Q}^{(p)}, \quad (3.73)$$

$$\mathbf{D} = \mathbf{T}_1 + \mathbf{Q} \mathbf{E}_1 + \mathbf{Q} \mathbf{T}_1, \quad (3.74)$$

$$\mathbf{U} = \mathbf{R}_2 \mathbf{E}_1 + \mathbf{R}_2 \mathbf{D}, \quad (3.75)$$

$$\mathbf{U}^* = \mathbf{R}_1^* \mathbf{E}_2 + \mathbf{R}_1^* \mathbf{T}_2^* + \mathbf{Q} \mathbf{R}_1^* \mathbf{E}_2 + \mathbf{Q} \mathbf{R}_1^* \mathbf{T}_2^*, \quad (3.76)$$

$$\mathbf{D}^* = \mathbf{T}_2^* + \mathbf{R}_2^* \mathbf{U}^*, \quad (3.77)$$

$$\mathbf{R} = \mathbf{R}_1 + \mathbf{E}_1 \mathbf{U} + \mathbf{T}_1^* \mathbf{U}, \quad (3.78)$$

$$\mathbf{T} = \mathbf{E}_2 \mathbf{D} + \mathbf{T}_2 \mathbf{E}_1 + \mathbf{T}_2 \mathbf{D}, \quad (3.79)$$

$$\mathbf{R}^* = \mathbf{R}_2^* + \mathbf{E}_2 \mathbf{U}^* + \mathbf{T}_2 \mathbf{U}^*, \quad (3.80)$$

$$\mathbf{T}^* = \mathbf{E}_1 \mathbf{D}^* + \mathbf{T}_1^* \mathbf{E}_2 + \mathbf{T}_1^* \mathbf{D}^*, \quad (3.81)$$

where $\mathbf{E}_1 = \mathbf{E}(\boldsymbol{\tau})$ and $\mathbf{E}_2 = \mathbf{E}(\boldsymbol{\tau}_B - \boldsymbol{\tau})$ with $\mathbf{E}(\boldsymbol{\tau})$ an $N \times N$ diagonal supermatrix with each element in the form of a 4×4 submatrix

$$\mathbf{E}_{i,j}(\boldsymbol{\tau}) = \delta_{ij} \exp\left(-\frac{\boldsymbol{\tau}}{\mu_j}\right) \mathbb{1} \quad \text{for } i, j = 1, 2, \dots, n, n+1, \dots, N. \quad (3.82)$$

Here we omitted the Fourier index m in every supermatrices.

For a homogeneous layer composed of randomly oriented mirror-symmetric scattering particles, we have the symmetry relations (3.40) and (3.41), which now become

$$\mathbf{R}^{*m} = \boldsymbol{\Delta}_4 \boldsymbol{\Delta}_3 \mathbf{R}^m \boldsymbol{\Delta}_3 \boldsymbol{\Delta}_4, \quad (3.83)$$

$$\mathbf{T}^{*m} = \boldsymbol{\Delta}_4 \boldsymbol{\Delta}_3 \mathbf{T}^m \boldsymbol{\Delta}_3 \boldsymbol{\Delta}_4, \quad (3.84)$$

where the $N \times N$ supermatrices Δ_3 and Δ_4 have elements in the forms of 4×4 submatrices as

$$(\Delta_3)_{ij} = \delta_{ij} \text{diag}(1, 1, -1, 1), \quad (3.85)$$

$$(\Delta_4)_{ij} = \delta_{ij} \text{diag}(1, 1, 1, -1), \quad (3.86)$$

for $i, j = 1, 2, \dots, n, n+1, \dots, N$.

By introducing the Fourier transformation and the supermatrix formalism, all the integrations in the adding equations are substituted by matrix multiplications. Since matrix manipulations can be rapidly realized with some linear algebra packages on computer, the supermatrix-form adding-doubling code is much more efficient than traditional adding-doubling codes. In this study, we used the BLAS (Basic Linear Algebra Subroutine) to handle all the matrix multiplications. To show the efficiency of the new supermatrix-form adding-doubling code with the BLAS, we calculated the upward and downward radiation of a three-layer atmosphere composed of atmospheric molecules and coarse mode dust aerosols. As is shown in Figure 3.2, the new code with the BLAS always requires less computational time compared to the code developed by Chowdhary ([6]), to reach the same precision for the serial calculation using the same computer. With the increasing number of Gaussian division points, the new code becomes increasingly efficient. When the number of Gaussian division points reaches 128, the new code is over ten times faster than Chowdhary's code.

3.3.4 Separation of Single-Scattering

For dust aerosols, the size parameter in the visible spectrum can reach up to several hundreds. In this case, the phase matrix would show a strong forward scattering peak, which may result in a slow convergence of the expansion coefficients in the

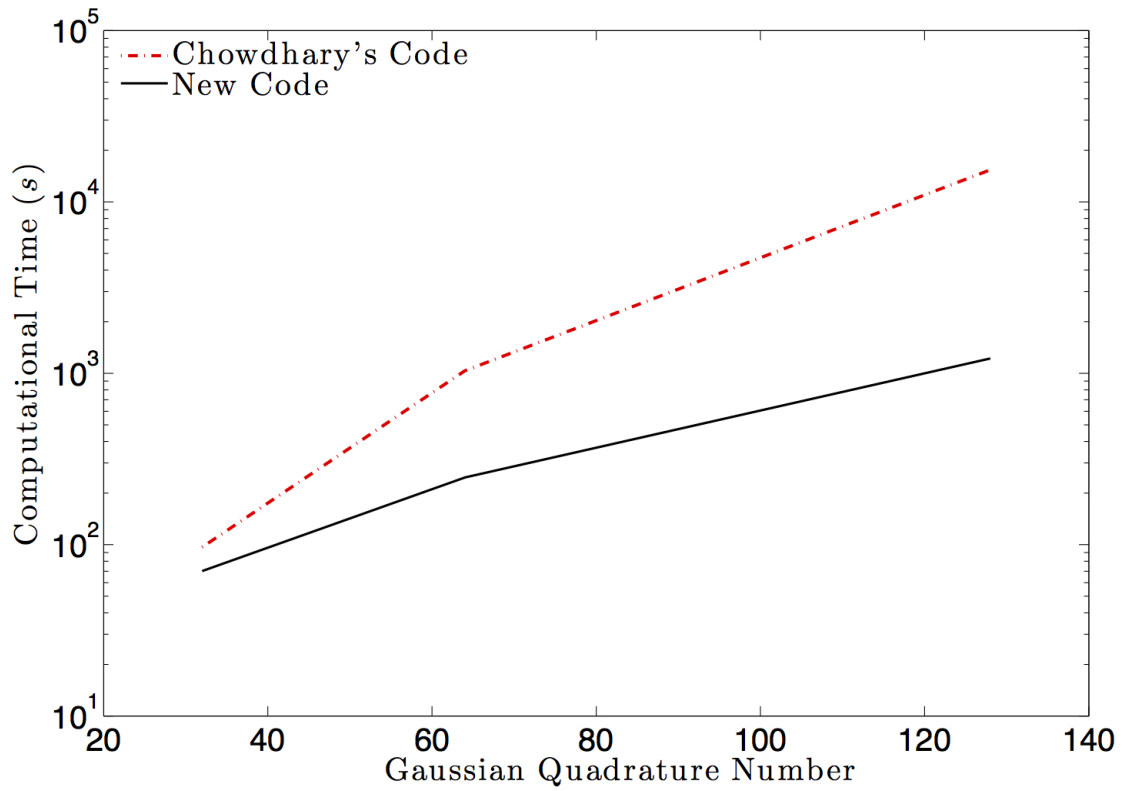


Figure 3.2: Comparison of the computational time versus the number of used Gaussian division points between Chowdhary's code and the new code to reach the same precision (e.g. 10^{-6}) on the same computer. The model considered here is a three-layer atmosphere composed of atmospheric molecules and coarse mode dust aerosols.

generalized spherical functions and thus a slow convergence of the Fourier expansion series. It has been found that the singular forward scattering feature tends to be washed out by the multiple scattering and the contribution of the high order Fourier terms is mainly due to the single scattering. Therefore, if the single-scattering contribution is separated from the reflection and transmission matrices, the number of Fourier terms required in the calculation as well as the computational time can be significantly reduced. In addition, when the first order scattering is separated, the doubling method may start with the second order scattering matrices, which can greatly increase the optical depth of the initial thin layer and decrease the doubling times. For this purpose, instead of using the equation (3.43), the Fourier expansions of the reflection and transmission matrices can be written as

$$\begin{aligned} \mathbf{R}(\mu, \mu', \phi - \phi') &= \mathbf{R}^{(1)}(\mu, \mu', \phi - \phi') + \frac{1}{2} \sum_{m=0}^{\infty} (2 - \delta_{m,0}) \\ &\quad \times \{ \mathbf{B}^{+m}(\phi - \phi') [\mathbf{R}^m(\mu, \mu') - \mathbf{R}^{(1)m}(\mu, \mu')] (\mathbb{1} + \mathbf{\Delta}) \\ &\quad + \mathbf{B}^{-m}(\phi - \phi') [\mathbf{R}^m(\mu, \mu') - \mathbf{R}^{(1)m}(\mu, \mu')] (\mathbb{1} - \mathbf{\Delta}) \}, \end{aligned} \quad (3.87)$$

$$\begin{aligned} \mathbf{T}(\mu, \mu', \phi - \phi') &= \mathbf{T}^{(1)}(\mu, \mu', \phi - \phi') + \frac{1}{2} \sum_{m=0}^{\infty} (2 - \delta_{m,0}) \\ &\quad \times \{ \mathbf{B}^{+m}(\phi - \phi') [\mathbf{T}^m(\mu, \mu') - \mathbf{T}^{(1)m}(\mu, \mu')] (\mathbb{1} + \mathbf{\Delta}) \\ &\quad + \mathbf{B}^{-m}(\phi - \phi') [\mathbf{T}^m(\mu, \mu') - \mathbf{T}^{(1)m}(\mu, \mu')] (\mathbb{1} - \mathbf{\Delta}) \}, \end{aligned} \quad (3.88)$$

where $\mathbf{R}^{(1)}(\mu, \mu', \phi - \phi')$ and $\mathbf{T}^{(1)}(\mu, \mu', \phi - \phi')$ are the first order scattering matrices for the whole atmosphere. For an atmosphere consisting of L homogeneous layers,

$$\mathbf{R}^{(1)}(\mu, \mu', \phi - \phi') = \sum_{l=1}^L \exp \left[-\frac{\Gamma_l^+}{\mu} - \frac{\Gamma_l^+}{\mu'} \right] \mathbf{R}_l^{(1)}(\mu, \mu', \phi - \phi'), \quad (3.89)$$

$$\mathbf{T}^{(1)}(\mu, \mu', \phi - \phi') = \sum_{l=1}^L \exp \left[-\frac{\Gamma_l^+}{\mu} - \frac{\Gamma_l^-}{\mu'} \right] \mathbf{T}_l^{(1)}(\mu, \mu', \phi - \phi'), \quad (3.90)$$

where $\Gamma_l^{+/-}$ denote the optical thickness between the upper/lower boundary of the atmosphere and the upper/lower boundary of the layer l , i.e.

$$\Gamma_l^+ = \sum_{l'=l+1}^L \tau_{l'}, \quad (3.91)$$

$$\Gamma_l^- = \sum_{l'=1}^{l-1} \tau_{l'}, \quad (3.92)$$

with the assumption that the count of layers is from the bottom to the top of the atmosphere. Here, the first order scattering matrices for the l th homogeneous layer with optical thickness τ_l , $\mathbf{R}_l^{(1)}(\mu, \mu', \phi - \phi')$ and $\mathbf{T}_l^{(1)}(\mu, \mu', \phi - \phi')$, can be calculated with

$$\begin{aligned} \mathbf{R}_l^{(1)}(\mu, \mu', \phi - \phi') &= \frac{\omega}{4(\mu + \mu')} \left[1 - \exp\left(-\frac{\tau_l}{\mu} - \frac{\tau_l}{\mu'}\right) \right] \\ &\times \mathbf{Z}(-\mu, \mu', \phi - \phi'), \end{aligned} \quad (3.93)$$

$$\begin{aligned} \mathbf{T}_l^{(1)}(\mu, \mu', \phi - \phi') &= \frac{\omega}{4(\mu - \mu')} \left[\exp\left(-\frac{\tau_l}{\mu}\right) - \exp\left(-\frac{\tau_l}{\mu'}\right) \right] \\ &\times \mathbf{Z}(\mu, \mu', \phi - \phi') \quad \text{if } \mu \neq \mu', \end{aligned} \quad (3.94)$$

$$\mathbf{T}_l^{(1)}(\mu, \mu', \phi - \phi') = \frac{\omega\tau_l}{4\mu^2} \exp\left(-\frac{\tau_l}{\mu}\right) \mathbf{Z}(\mu, \mu', \phi - \phi') \quad \text{if } \mu = \mu'. \quad (3.95)$$

3.3.5 Truncation of Phase Matrix

In addition to the separation of the first order scattering, truncation of the phase matrix is another important technique to accelerate the code when dealing with large dust aerosols. The delta-M method ([56]), following the delta-Eddington approximation, is a well-known truncation method for a phase function when solving the scalar radiative transfer equation. Although many other improved truncation methods have been developed afterwards, such as the delta-fit method ([22]), geo-

metrical truncation method ([23]), etc., the delta-M method is still preferred under most circumstances due to its simple mathematical form and the automatically guaranteed flux conservation. The delta-M method for the phase function can be easily extended to all the elements of a phase matrix. Supposing that we want to truncate the phase function to the order of M and a delta function can well approximate the contribution of the higher order terms, we then have

$$a_1(\Theta) = \sum_{l=0}^{\infty} \alpha_1^l P_{0,0}^l(\cos \Theta) \simeq 2f\delta(1 - \cos \Theta) + (1 - f) \sum_{l=0}^M \alpha_1^l P_{0,0}^l(\cos \Theta), \quad (3.96)$$

where $f = \alpha_1^{M+1}/(2M + 3)$ represents the fraction of energy contained in the truncated forward scattering peak. The elements of the truncated phase matrix $\tilde{\mathbf{P}}$ can be determined as follows:

$$\tilde{a}_1(\Theta) = \sum_{l=0}^M \tilde{\alpha}_1^l P_{0,0}^l(\cos \Theta), \quad (3.97)$$

$$\tilde{a}_2(\Theta) = \tilde{a}_1(\Theta) + \frac{a_2(\Theta) - a_1(\Theta)}{1 - f}, \quad (3.98)$$

$$\tilde{a}_3(\Theta) = \tilde{a}_1(\Theta) + \frac{a_3(\Theta) - a_1(\Theta)}{1 - f}, \quad (3.99)$$

$$\tilde{a}_4(\Theta) = \tilde{a}_1(\Theta) + \frac{a_4(\Theta) - a_1(\Theta)}{1 - f}, \quad (3.100)$$

$$\tilde{b}_1(\Theta) = \frac{b_1(\Theta)}{1 - f}, \quad (3.101)$$

$$\tilde{b}_2(\Theta) = \frac{b_2(\Theta)}{1 - f}, \quad (3.102)$$

where

$$\tilde{\alpha}_1^l = \frac{\alpha_1^l - (2l + 1)f}{1 - f} \quad \text{for } l = 0, \dots, M. \quad (3.103)$$

Accordingly, the single-scattering albedo and the optical thickness of the dust

aerosol need to be adjusted based on the so-called similarity principle:

$$\tilde{\omega} = \frac{(1-f)\omega}{1-\omega f}, \quad (3.104)$$

$$\tilde{\tau} = (1-\omega f)\tau. \quad (3.105)$$

In order to make the calculation consistent, the required number of Gaussian division points n is related to the highest order of the truncated phase matrix M by Chandrasekhar's criterion $4n - 1 > 2M$ ([4]). As a result, with the delta-M truncation, not only the required order of Fourier terms but also the required number of Gaussian division points can be greatly reduced, while the introduced error is controllable, which implies that the speed and precision of the code is adjustable according to the given computational time and the error of measurements.

3.4 The Atmosphere-Surface System

In previous subsections, we limited ourself to the standard problem with a black surface at the bottom of the atmosphere. In fact, the surface contribution to measurements can be ignored only in occasional cases, such as dust aerosol retrieval over ocean using the near-infrared channel. Over land, especially over the dust aerosol source region, the signal from the surface is so strong for the visible channels that is comparable to or exceed the signal from dust aerosols. Therefore, we have to consider the radiative transfer process in such a coupled atmosphere-surface system to separate the surface contribution.

The reflection properties of a surface can be described by a 4×4 BRDF \mathbf{R}_{srf} as

$$\mathbf{I}(\mu, \phi) = \frac{1}{\pi} \int_0^{2\pi} d\phi' \int_0^1 d\mu' \mu' \mathbf{R}_{srf}(\mu, \phi; \mu', \phi') \mathbf{I}_0(\mu', \phi'), \quad (3.106)$$

where $\mathbf{I}_0(\mu, \phi)$ is the Stokes vector of the radiance incident on the surface and $\mathbf{I}(\mu, \phi)$

is the Stokes vector of the reflected radiance. If there is no atmosphere and the solar flux \mathbf{F}_0 in direction (μ_0, ϕ_0) is directly incident on the surface, the equation (3.106) becomes the most frequently seen form:

$$\mathbf{I}(\mu, \phi) = \frac{\mu_0}{\pi} \mathbf{R}_{srf}(\mu, \phi; \mu_0, \phi_0) \mathbf{F}_0. \quad (3.107)$$

3.4.1 BRDF Models

In order to study aerosols over various surface conditions, many surface BRDF models have been proposed ([29]). The most famous one is the Lambertian surface (namely the ideal diffusely reflecting surface), for which the reflected radiance is isotropic. The 4×4 BRDF is written as

$$\mathbf{R}_L(\mu, \mu', \phi - \phi') = \begin{pmatrix} A & 0 & 0 & 0 \\ 0 & 0 & 0 & 0 \\ 0 & 0 & 0 & 0 \\ 0 & 0 & 0 & 0 \end{pmatrix} \quad (3.108)$$

where A is the reflectivity (or surface albedo) of the surface. The Lambertian surface is usually used when the knowledge about the actual surface reflection properties is missing.

However, for the multi-angular observations, the isotropic Lambertian surface may introduce significant error. To correctly characterize the directional feature of the surface reflection, the kernel-driven model was developed to replace the isotropic surface reflectance ([55]). The most common kernel-driven model uses a linear combination of three kernels f_{iso} , f_{vol} , and f_{geom} , which are representing isotropic, volumetric, and geometric-optics components of the surface scattering, respectively. Instead

of a constant surface reflectivity, the reflectivity of the surface becomes a function of the incident and viewing angles, i.e.

$$A_{Ross-Li}(\mu, \mu', \phi - \phi') = f_{iso} + k_{vol} f_{vol}(\mu, \mu', \phi - \phi') + k_{geom} f_{geom}(\mu, \mu', \phi - \phi'). \quad (3.109)$$

The volumetric scattering kernel f_{vol} is derived in the single-scattering approximation from the radiative transfer theory for a layer of randomly oriented and randomly positioned facets with fixed reflectance and transmittance, which has the form

$$f_{vol}(\mu, \mu', \phi - \phi') = \frac{(\pi/2 - \Theta) \cos \Theta + \sin \Theta}{\mu + \mu'} - \frac{\pi}{4}, \quad (3.110)$$

where Θ is the scattering angle,

$$\cos \Theta = -\mu\mu' + (1 - \mu^2)^{1/2}(1 - \mu'^2)^{1/2} \cos(\phi - \phi'). \quad (3.111)$$

The geometric-optics kernel f_{geom} takes into account the geometric structure of reflectors as well as the shadowing by reflectors. The often used geometric-optics kernel is the Li-sparse kernel given by

$$f_{geom}(\mu, \mu', \phi - \phi') = O(\mu, \mu', \phi - \phi') + \frac{1 - 2 \cos \tilde{\theta} - 2 \cos \tilde{\theta}' - \cos \tilde{\Theta}}{\cos \tilde{\theta} \cos \tilde{\theta}'}, \quad (3.112)$$

where the $\tilde{\theta}$ and $\tilde{\theta}'$ are defined as

$$\tilde{\theta} = \tan^{-1} \left(\frac{b}{r} \tan |\theta| \right), \quad (3.113)$$

$$\tilde{\theta}' = \tan^{-1} \left(\frac{b}{r} \tan |\theta'| \right), \quad (3.114)$$

and

$$O(\mu, \mu', \phi - \phi') = \frac{(t - \sin t)(\cos \tilde{\theta} + \cos \tilde{\theta}')}{\pi \cos \tilde{\theta} \cos \tilde{\theta}'}, \quad (3.115)$$

$$\cos t = \frac{h}{b} \frac{\cos \tilde{\theta} \cos \tilde{\theta}'}{\cos \tilde{\theta} + \cos \tilde{\theta}'} \sqrt{D^2 + \tan^2 \tilde{\theta} \tan^2 \tilde{\theta}' \sin^2(\phi - \phi')}, \quad (3.116)$$

$$D = \sqrt{\tan^2 \tilde{\theta} + \tan^2 \tilde{\theta}' + 2 \tan \tilde{\theta} \tan \tilde{\theta}' \cos(\phi - \phi')}, \quad (3.117)$$

$$\cos \tilde{\Theta} = -\cos \tilde{\theta} \cos \tilde{\theta}' + \sin \tilde{\theta} \sin \tilde{\theta}' \cos(\phi - \phi'). \quad (3.118)$$

In the equation (3.116), if the obtained $\cos t$ is greater than 1, then set $\cos t$ equal to 1; if $\cos t$ is less than -1, then set $\cos t$ equal to -1. Here, h/b and b/r are two fixed parameters. For example, the Li-sparse kernel used in the MODIS BRDF retrieval algorithm chose $h/b = 2$ and $b/r = 1$ ([47]).

Over ocean, the reflection of the air-water interface can also be modeled with a BRDF. If the ocean surface is flat, the reflection properties can be simply described with the Fresnel equations. For a windy-ruffled ocean surface, the BRDF can be calculated analytically in the Kirchhoff approximation ([51]), which is given by

$$\mathbf{R}_{ocn}(\mu, \mu', \phi - \phi') = \frac{|\mathbf{k}_d^4|}{4\mu\mu'|\hat{\mathbf{n}} \times \hat{\mathbf{n}}'|^4 k_{dz}^4} \exp \left[-\frac{k_{dx}^2 + k_{dy}^2}{2s^2 k_{dz}^2} \right] \mathbf{M}(\mu, \mu', \phi - \phi'), \quad (3.119)$$

where

$$\hat{\mathbf{n}} = ((1 - \mu^2)^{1/2} \cos \phi, (1 - \mu^2)^{1/2} \sin \phi, \mu), \quad (3.120)$$

$$\hat{\mathbf{n}}' = ((1 - \mu'^2)^{1/2} \cos \phi', (1 - \mu'^2)^{1/2} \sin \phi', -\mu'), \quad (3.121)$$

$$\mathbf{k}_d = k(\hat{\mathbf{n}}' - \hat{\mathbf{n}}) = k_{dx}\hat{\mathbf{x}} + k_{dy}\hat{\mathbf{y}} + k_{dz}\hat{\mathbf{z}}, \quad (3.122)$$

k is the free space wavenumber and s is the root mean square slope of the ocean surface. According to the Cox and Munk slope distribution for a rough ocean surface

([7]), $2s^2 = 0.003 + 0.00512 \times W$, where W is the wind speed at the ocean surface in the units of m/s . The elements of the 4×4 matrix $\mathbf{M}(\mu, \mu', \phi - \phi')$ are given by

$$M_{11} = \frac{1}{2}[|f_{\theta\theta}|^2 + |f_{\theta\phi}|^2 + |f_{\phi\theta}|^2 + |f_{\phi\phi}|^2], \quad (3.123)$$

$$M_{12} = \frac{1}{2}[|f_{\theta\theta}|^2 - |f_{\theta\phi}|^2 + |f_{\phi\theta}|^2 - |f_{\phi\phi}|^2], \quad (3.124)$$

$$M_{13} = -\text{Re}[f_{\theta\theta}f_{\phi\phi}^* + f_{\phi\theta}f_{\theta\phi}^*], \quad (3.125)$$

$$M_{14} = -\text{Im}[f_{\theta\theta}f_{\theta\phi}^* + f_{\phi\theta}f_{\phi\phi}^*], \quad (3.126)$$

$$M_{21} = \frac{1}{2}[|f_{\theta\theta}|^2 + |f_{\theta\phi}|^2 - |f_{\phi\theta}|^2 - |f_{\phi\phi}|^2], \quad (3.127)$$

$$M_{22} = \frac{1}{2}[|f_{\theta\theta}|^2 - |f_{\theta\phi}|^2 - |f_{\phi\theta}|^2 + |f_{\phi\phi}|^2], \quad (3.128)$$

$$M_{23} = -\text{Re}[f_{\theta\theta}f_{\theta\phi}^* - f_{\phi\theta}f_{\phi\phi}^*], \quad (3.129)$$

$$M_{24} = -\text{Im}[f_{\theta\theta}f_{\theta\phi}^* - f_{\phi\theta}f_{\phi\phi}^*], \quad (3.130)$$

$$M_{31} = -\text{Re}[f_{\theta\theta}f_{\phi\theta}^* + f_{\theta\phi}f_{\phi\phi}^*], \quad (3.131)$$

$$M_{32} = -\text{Re}[f_{\theta\theta}f_{\phi\theta}^* - f_{\theta\phi}f_{\phi\phi}^*], \quad (3.132)$$

$$M_{33} = \text{Re}[f_{\theta\theta}f_{\phi\phi}^* + f_{\theta\phi}f_{\phi\theta}^*], \quad (3.133)$$

$$M_{34} = \text{Im}[f_{\theta\theta}f_{\phi\phi}^* - f_{\theta\phi}f_{\phi\theta}^*], \quad (3.134)$$

$$M_{41} = \text{Im}[f_{\theta\theta}f_{\phi\theta}^* + f_{\theta\phi}f_{\phi\phi}^*], \quad (3.135)$$

$$M_{42} = \text{Im}[f_{\theta\theta}f_{\phi\theta}^* - f_{\theta\phi}f_{\phi\phi}^*], \quad (3.136)$$

$$M_{43} = -\text{Im}[f_{\theta\theta}f_{\phi\phi}^* + f_{\theta\phi}f_{\phi\theta}^*], \quad (3.137)$$

$$M_{44} = \text{Re}[f_{\theta\theta}f_{\phi\phi}^* - f_{\theta\phi}f_{\phi\theta}^*], \quad (3.138)$$

where

$$f_{\theta\theta} = (\hat{\phi}' \cdot \hat{\mathbf{n}})(\hat{\phi} \cdot \hat{\mathbf{n}}')R_{\perp} + (\hat{\theta}' \cdot \hat{\mathbf{n}})(\hat{\theta} \cdot \hat{\mathbf{n}}')R_{\parallel}, \quad (3.139)$$

$$f_{\theta\phi} = -(\hat{\theta}' \cdot \hat{\mathbf{n}})(\hat{\phi} \cdot \hat{\mathbf{n}}')R_{\perp} + (\hat{\phi}' \cdot \hat{\mathbf{n}})(\hat{\theta} \cdot \hat{\mathbf{n}}')R_{\parallel}, \quad (3.140)$$

$$f_{\phi\theta} = -(\hat{\phi}' \cdot \hat{\mathbf{n}})(\hat{\theta} \cdot \hat{\mathbf{n}}')R_{\perp} + (\hat{\theta}' \cdot \hat{\mathbf{n}})(\hat{\phi} \cdot \hat{\mathbf{n}}')R_{\parallel}, \quad (3.141)$$

$$f_{\phi\phi} = (\hat{\theta}' \cdot \hat{\mathbf{n}})(\hat{\theta} \cdot \hat{\mathbf{n}}')R_{\perp} + (\hat{\phi}' \cdot \hat{\mathbf{n}})(\hat{\phi} \cdot \hat{\mathbf{n}}')R_{\parallel}. \quad (3.142)$$

In the equations (3.139)-(3.142), the unit vectors $\hat{\phi}$ and $\hat{\theta}$ are defined as

$$\hat{\phi} = \frac{\hat{\mathbf{z}} \times \hat{\mathbf{n}}}{|\hat{\mathbf{z}} \times \hat{\mathbf{n}}|}, \quad (3.143)$$

$$\hat{\theta} = \hat{\phi} \times \hat{\mathbf{n}}, \quad (3.144)$$

and R_{\perp} and R_{\parallel} are the coefficients of the Fresnel reflection for the perpendicular and the parallel polarized light, respectively, which are given by

$$R_{\perp} = \frac{\cos \theta - \sqrt{m^2 - 1 + \cos^2 \theta}}{\cos \theta + \sqrt{m^2 - 1 + \cos^2 \theta}}, \quad (3.145)$$

$$R_{\parallel} = \frac{m^2 \cos \theta - \sqrt{m^2 - 1 + \cos^2 \theta}}{m^2 \cos \theta + \sqrt{m^2 - 1 + \cos^2 \theta}}, \quad (3.146)$$

where m is the complex refractive index of the ocean water and the incident angle θ is given by

$$\cos \theta = \frac{\hat{\mathbf{n}}' \cdot (\hat{\mathbf{n}}' - \hat{\mathbf{n}})}{|\hat{\mathbf{n}}' - \hat{\mathbf{n}}|}. \quad (3.147)$$

If the viewing zenith angle or the incident angle is large, e.g. μ or μ' close to 0, we have to take into account the shadowing effect ([51]) of the surface wave by multiplying the $\mathbf{R}_{ocn}(\mu, \mu', \phi - \phi')$ by a bidirectional shadowing function $S(\mu, \mu')$ given by

$$S(\mu, \mu') = \frac{1}{1 + \Lambda(\mu) + \Lambda(\mu')}, \quad (3.148)$$

where

$$\Lambda(\mu) = \frac{\sqrt{2s^2(1-\mu^2)}}{2\sqrt{\pi}\mu} \exp\left[-\frac{\mu^2}{2s^2(1-\mu^2)}\right] - \frac{1}{2} \operatorname{erfc}\left[\frac{\mu}{\sqrt{2s^2(1-\mu^2)}}\right], \quad (3.149)$$

and $\operatorname{erfc}(x)$ is the complementary error function.

For the purpose of simulation of reflection properties of different surface types, we build a surface BRDF library to include all these surface BRDF models. The library is imbedded into our adding-doubling code with the following algorithm.

3.4.2 Implementing Surface BRDFs in Adding-Doubling

When a surface BRDF is added to the standard problem, it changes the lower boundary condition (3.12) of the vector radiative transfer equation to

$$\mathbf{I}(\tau_B; -\mu, \phi) = \frac{1}{\pi} \int_0^{2\pi} d\phi' \int_0^{+1} d\mu' \mu' \mathbf{R}_{surf}(\mu, \mu', \phi - \phi') \mathbf{I}(\tau_B; \mu', \phi'), \quad (3.150)$$

To correctly account for the surface contribution, we have to fully consider the interaction between the atmosphere and the surface. Following Subsection 3.3, the reflection matrix of the coupled atmosphere-surface system can be easily calculated through the following adding equations:

$$\mathbf{Q}^{(1)}(\mu, \mu', \phi - \phi') = \mathbf{R}_{atm}^*(\mu, \mu'', \phi - \phi'') * \mathbf{R}_{surf}(\mu'', \mu', \phi'' - \phi'), \quad (3.151)$$

$$\mathbf{Q}^{(p+1)}(\mu, \mu', \phi - \phi') = \mathbf{Q}^{(1)}(\mu, \mu'', \phi - \phi'') * \mathbf{Q}^{(p)}(\mu'', \mu', \phi'' - \phi'), \quad (3.152)$$

$$\mathbf{Q}(\mu, \mu', \phi - \phi') = \sum_{p=1}^{\infty} \mathbf{Q}^{(p)}(\mu, \mu', \phi - \phi'), \quad (3.153)$$

$$\begin{aligned} \mathbf{D}_{atm+surf}(\tau; \mu, \mu', \phi - \phi') &= \mathbf{T}_{atm}(\mu, \mu', \phi - \phi') \\ &+ \mathbf{Q}(\mu, \mu'', \phi - \phi'') * \mathbf{E}(\tau_B; \mu'', \mu', \phi'' - \phi') \\ &+ \mathbf{Q}(\mu, \mu'', \phi - \phi'') * \mathbf{T}_{atm}(\mu'', \mu', \phi'' - \phi'), \end{aligned} \quad (3.154)$$

$$\begin{aligned} \mathbf{U}_{atm+surf}(\boldsymbol{\tau}_B; \mu, \mu', \phi - \phi') &= \mathbf{R}_{surf}(\mu, \mu'', \phi - \phi'') * \mathbf{E}(\boldsymbol{\tau}_B; \mu'', \mu', \phi'' - \phi') \\ &+ \mathbf{R}_{surf}(\mu, \mu'', \phi - \phi'') * \mathbf{D}_{atm+surf}(\boldsymbol{\tau}_B; \mu'', \mu', \phi'' - \phi'), \end{aligned} \quad (3.155)$$

$$\begin{aligned} \mathbf{R}_{atm+surf}(\mu, \mu', \phi - \phi') &= \mathbf{R}_{atm}(\mu, \mu', \phi - \phi') \\ &+ \mathbf{E}(\boldsymbol{\tau}_B; \mu, \mu'', \phi - \phi'') * \mathbf{U}_{atm+surf}(\boldsymbol{\tau}_B; \mu'', \mu', \phi'' - \phi'). \quad (3.156) \\ &+ \mathbf{T}_{atm}^*(\mu, \mu'', \phi - \phi'') * \mathbf{U}_{atm+surf}(\boldsymbol{\tau}_B; \mu'', \mu', \phi'' - \phi'), \end{aligned}$$

Unlike the atmosphere-only case, we are not interested in the transmission matrix of the atmosphere-surface system $\mathbf{T}_{atm+surf}(\mu, \mu', \phi - \phi')$, but the downward radiation matrix just above the surface $\mathbf{D}_{atm+surf}(\boldsymbol{\tau}_B; \mu, \mu', \phi - \phi')$.

For the speed concern, we also expand the surface BRDF into Fourier series and separate the single-scattering contribution, i.e.

$$\begin{aligned} \mathbf{R}_{atm+surf}(\mu, \mu', \phi - \phi') &= \mathbf{R}_{atm+surf}^{(1)}(\mu, \mu', \phi - \phi') + \frac{1}{2} \sum_{m=0}^{\infty} (2 - \delta_{m,0}) \\ &\times \{ \mathbf{B}^{+m}(\phi - \phi') [\mathbf{R}^m(\mu, \mu') - \mathbf{R}^{(1)m}(\mu, \mu')] (\mathbf{1} + \boldsymbol{\Delta}) \\ &+ \mathbf{B}^{-m}(\phi - \phi') [\mathbf{R}^m(\mu, \mu') - \mathbf{R}^{(1)m}(\mu, \mu')] (\mathbf{1} - \boldsymbol{\Delta}) \}, \end{aligned} \quad (3.157)$$

where

$$\begin{aligned} \mathbf{R}_{surf}^m(\mu, \mu') &= \frac{1}{2\pi} \int_0^{2\pi} d(\phi - \phi') [\mathbf{B}^{+m}(\phi - \phi') \\ &+ \mathbf{B}^{-m}(\phi - \phi')] \mathbf{R}_{surf}(\mu, \mu', \phi - \phi'), \end{aligned} \quad (3.158)$$

$$\begin{aligned} \mathbf{R}_{atm+surf}^{(1)}(\mu, \mu', \phi - \phi') &= \mathbf{R}_{atm}^{(1)}(\mu, \mu', \phi - \phi') \\ &+ \exp \left[-\frac{\boldsymbol{\tau}_B}{\mu} - \frac{\boldsymbol{\tau}_B}{\mu'} \right] \mathbf{R}_{surf}(\mu, \mu', \phi - \phi'). \end{aligned} \quad (3.159)$$

3.4.3 Validation of the Adding-Doubling Code

In order to validate our adding-doubling code, we calculated the Stokes vector of upward radiance at the TOA using the RayXP ([62]), the Monte-Carlo code ([63]), and our new adding-doubling code. To make sure the code is capable of simulating radiance of multi-layer optically thick dust aerosols above a highly reflective land surface like a desert, we choose the model to be a bi-layer atmosphere of fine mode dust aerosols with the total aerosol optical depth equal to 1.0 above a Lambertian surface with surface albedo 0.8. As is shown in Figure 3.3, good agreements are found for all the absolute values of the components calculated by all the three codes at all angles. The only difference between the Monte-Carlo results and our results is a minus sign for the V component, which is due to the different definitions of the circular polarization. The RayXP results cannot consistently agree with any of the other two results for components Q, U, V in the meridian planes at azimuthal angles equal to 0° and 90° . It suggests that our method is accurate and self-consistent, but one should be careful about the definitions of polarization when comparing results of our code with others.

To demonstrate the capability of our adding-doubling code to deal with large dust aerosols, we fix the atmosphere model but substitute the fine mode dust aerosols with coarse mode dust aerosols. As is shown in Figure 3.4, results of all the three codes agree very well with each other for components I and U . For the component Q , besides the sign problem, it is found that the errors in the absolute values of RayXP become significant at large viewing angles (e.g. larger than 50°), but our results still agree with the Monte-Carlo results. Despite of the small value of the component V , it still can be seen that errors of the Monte-Carlo method appear at large viewing zenith angles (e.g. larger than 70°) in the meridian planes at azimuthal angles equal

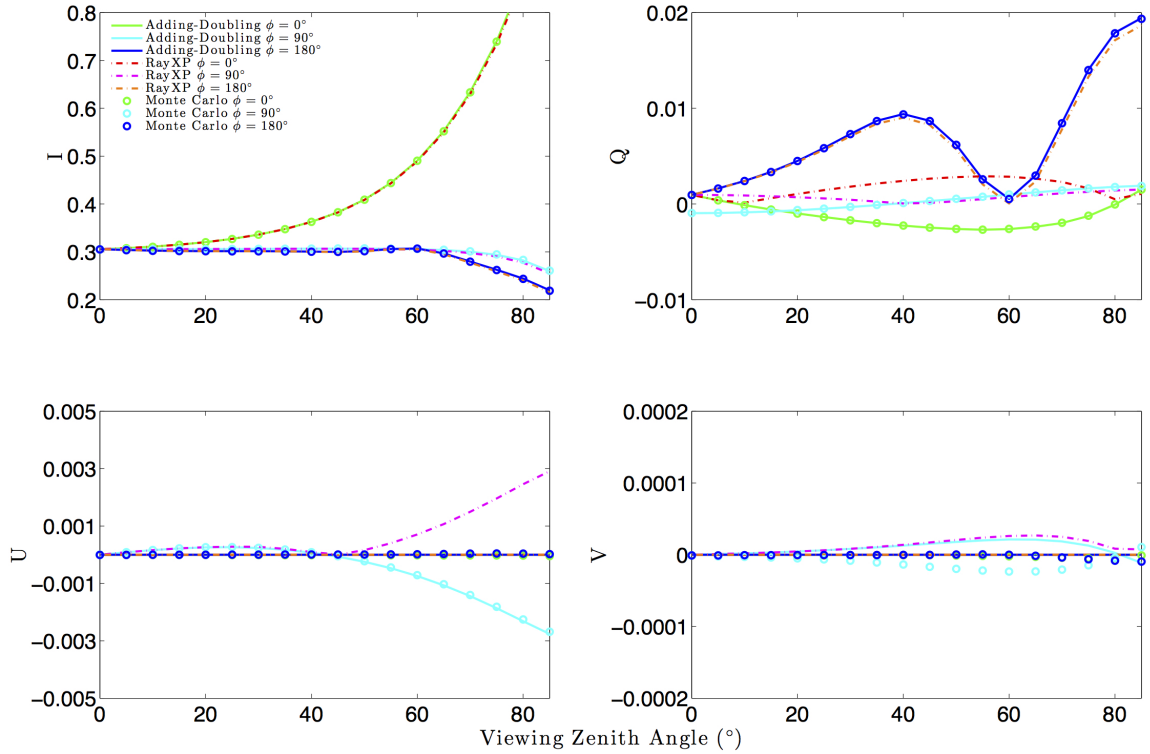


Figure 3.3: Comparison of the Stokes vectors (I, Q, U, V) of upward radiances at the TOA calculated by our new adding-doubling code, the RayXP, and the Monte-Carlo method. The model here is a bi-layer atmosphere of fine mode dust aerosols with the total aerosol optical depth equal to 1.0 above a Lambertian surface with the surface albedo 0.8. The solar zenith angle is 60° . The Stokes vectors in three meridian planes at azimuthal angles equal to 0° , 90° , and 180° are plotted.

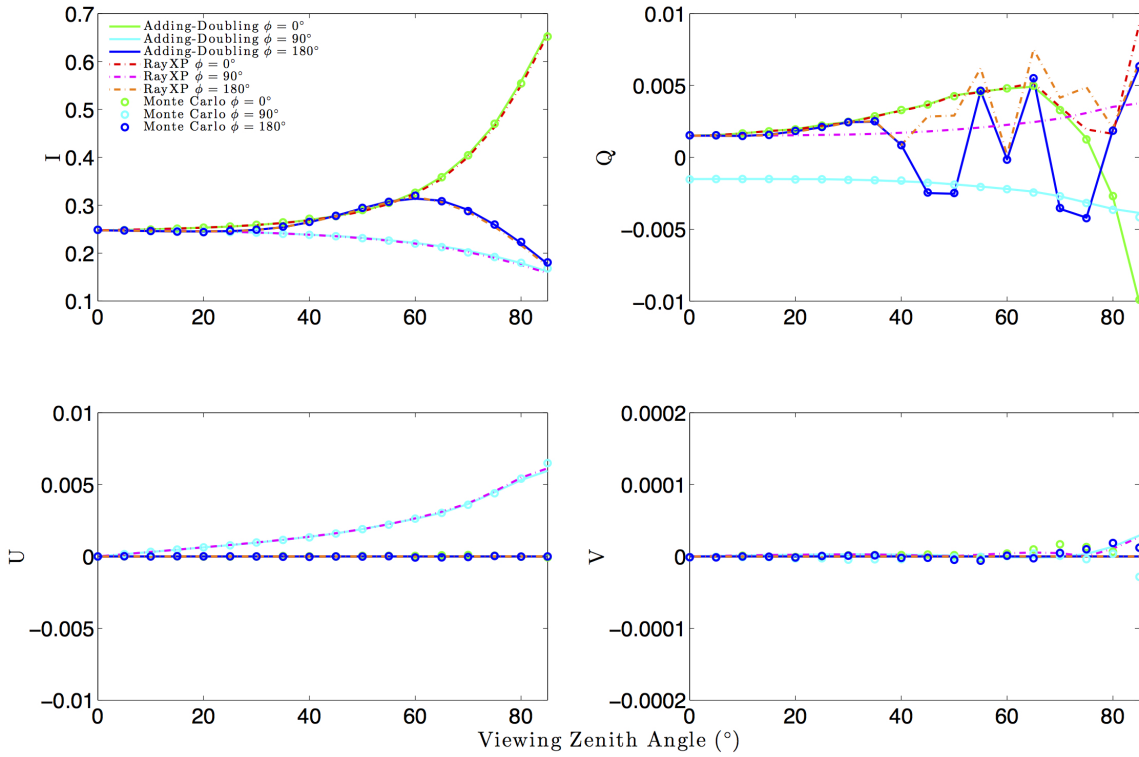


Figure 3.4: Comparison of the Stokes vectors (I, Q, U, V) of upward radiances at the TOA calculated by our new adding-doubling code, the RayXP, and the Monte-Carlo method. The model here is a bi-layer atmosphere of coarse mode dust aerosols with the total aerosol optical depth equal to 1.0 above a Lambertian surface with the surface albedo 0.8. The solar zenith angle is 60° . The Stokes vectors in three meridian planes at azimuthal angles equal to 0° , 90° , and 180° are plotted.

to 0° and 180° , since the exact theoretical results as well as our results give 0.

As a validation of our adding-doubling code for the system of a atmosphere coupled with a user-defined surface, we compare our results with the RayXP results (see Figure 3.5). The atmosphere-surface system considered here is a thin Rayleigh layer with optical depth equal to 0.1 above a windy-ruffled ocean surface with the wind speed at ocean surface equal to $10.0m/s$. It is found that our results perfectly resemble the RayXP results for all the components at all angles, in spite of the fact that different approximations for the windy-ruffled ocean surface BRDF models are

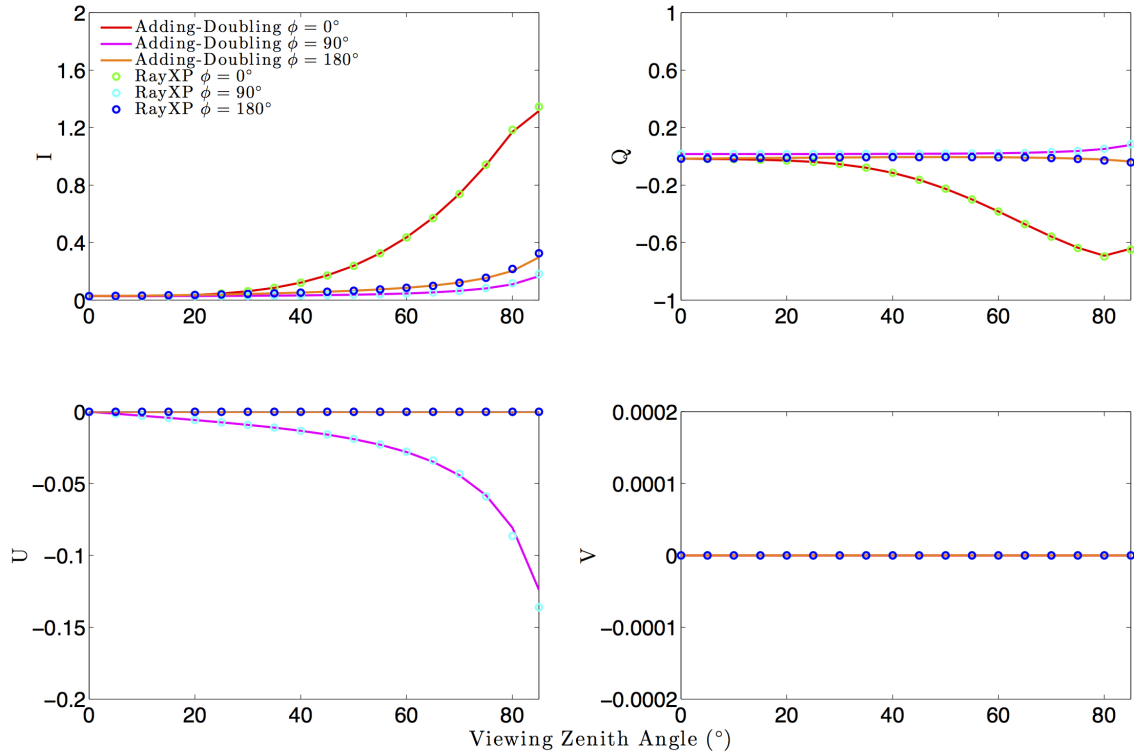


Figure 3.5: Comparison of the Stokes vectors (I, Q, U, V) of upward radiances at the TOA calculated by our new adding-doubling code and the RayXP. The model here is a thin Rayleigh layer with the optical depth equal to 0.1 above a windy-ruffled ocean surface with the wind speed at ocean surface equal to $10.0m/s$. The solar zenith angle is 60° . The Stokes vectors in three meridian planes at azimuthal angles equal to $0^\circ, 90^\circ$, and 180° are plotted.

used in the two codes, e.g. the geometric-optics approximation in RayXP and the Kirchhoff approximation in our adding-doubling code.

3.5 A Fast Algorithm Based on Icosahedral Grid

As an alternative method to circumvent huge supermatrices due to the large number of required Gaussian division points and the slow convergent Fourier series when considering a medium composed of large scattering particles, all the integrations in the adding equations (3.25-3.35) can be performed numerically on an icosahedral

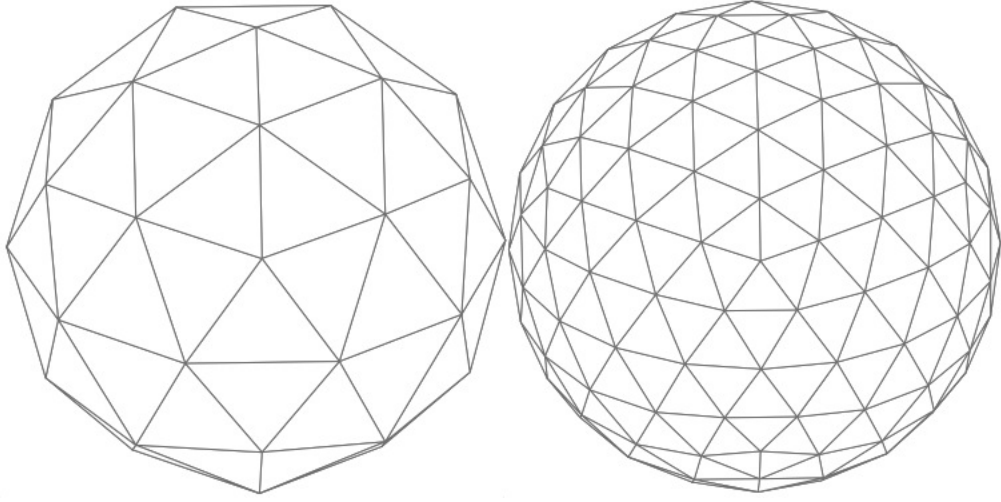


Figure 3.6: Icosahedral grid of level 2 consisting of 40 triangular faces on the left and icosahedral grid of level 4 consisting of 160 triangular faces on the right.

mesh. This technique has already been successfully applied to solve the shallow-water equations and the scalar radiative transfer equation ([19], [54]). The icosahedral grid can be generated by recursively bisecting the 20 triangular faces of the original simple regular icosahedron and projecting bisection points onto the circumsphere. The number of recursive refinements is referred to as grid level L . Figure 3.6 shows the icosahedral grids of level $L = 2$ and level $L = 4$. The number of triangular faces is given by $F = 20L^2$.

Instead of performing Fourier transformation and calculating each term through Gaussian quadrature, we approximate the integral in equation (3.23) with the following summation

$$\mathbf{X}(\mu, \phi; \mu'', \phi'') * \mathbf{Y}(\mu'', \phi''; \mu', \phi') = \frac{2}{S} \sum_{i=1}^n \mathbf{X}(\mu, \phi; \mu_i, \phi_i) \mathbf{Y}(\mu_i, \phi_i; \mu', \phi') A_i, \quad (3.160)$$

with

$$S = \sum_{i=1}^n A_i \quad (3.161)$$

where A_i is the area of the i th triangular face, and the summation is performed over the top half icosahedral grid, e.g. $n = F/2$, since the integral is over the top hemisphere in the adding equations. μ_i and ϕ_i can be determined by the position vector \mathbf{r}_i at the center of the i th triangular face as

$$\mu_i = \frac{r_{iz}}{|\mathbf{r}_i|}, \quad (3.162)$$

$$\phi_i = \arctan \frac{r_{iy}}{r_{ix}}. \quad (3.163)$$

Then, by following the standard adding equations (3.25)-(3.35), the reflection and transmission matrix can be solved. In practice, we use supermatrices and the BLAS to realize the fast computation. The procedure is identical to that of Subsection 3.3.3, except that we need to change the definition of the supermatrix \mathbf{X} . For example, let us define the $N \times N$ supermatrix \mathbf{X} with each element in the form of a 4×4 submatrix as

$$\mathbf{X}_{i,j} = c_i \mathbf{X}(\mu_i, \phi_i; \mu_j, \phi_j) c_j \quad \text{for } i, j = 1, 2, \dots, n, n+1, \dots, N, \quad (3.164)$$

where

$$c_i = \begin{cases} \sqrt{\frac{2A_i\mu_i}{S}} & \text{for } i = 1, 2, \dots, n \\ 1 & \text{for } i = n, n+1, \dots, N \end{cases}. \quad (3.165)$$

Similarly, the indices $i = n, n+1, \dots, N$ are for the interested observation directions that are not on the grid points. With the redefined supermatrices, the VRTE can be solved by following the equations (3.69)-(3.86) without considering each Fourier term.

As is shown in Figure 3.7, we compared the results of the fast model with those of the adding-doubling using the rigorous procedure for dust aerosols over a black surface. It is found that the fast model results agree well with the rigorous results for the component I and Q. However, there are discrepancies for the components U and V at large viewing zenith angles (e.g. $> 50^\circ$). The exact value for U and V should be 0 at any viewing angles. The difference between zero and the value of U or V of the fast model can be regarded as the error of the fast model. It is clear that the error is increasing with the viewing zenith angle. For large viewing zenith angles, where the error is on the order of magnitude of 10^{-6} , it is still much smaller than the usual error of a radiometer onboard a satellite. Therefore, the fast model can be appropriately used in the following circumstances: (1) only the radiance is concerned; (2) the viewing angle is not so large; (3) the required precision is moderate.

3.6 Summary

As a study to improve the present forward model in aerosol retrieval, an adding-doubling code is developed to solve the VRTE. Many efforts have been made to improve the efficiency of the code so that it is applicable to an iterative retrieval algorithm with affordable computational time: (a) The adding equations are realized in the supermatrix form and supermatrix multiplications are handled with the BLAS; (b) The first order scattering is separated in the multiple scattering calculation to accelerate the convergence of Fourier series; (c) The expansion of phase matrices of dust aerosols in the generalized spherical functions can be truncated using delta-M method if necessary; (c) If a moderate precision is acceptable, all the integrations can be conducted on an icosahedral grid to further speed up the code. For the purpose of simulating reflection properties of diverse land and ocean surfaces, a surface BRDF library is embedded into the code. In the following work on the retrieval of non-

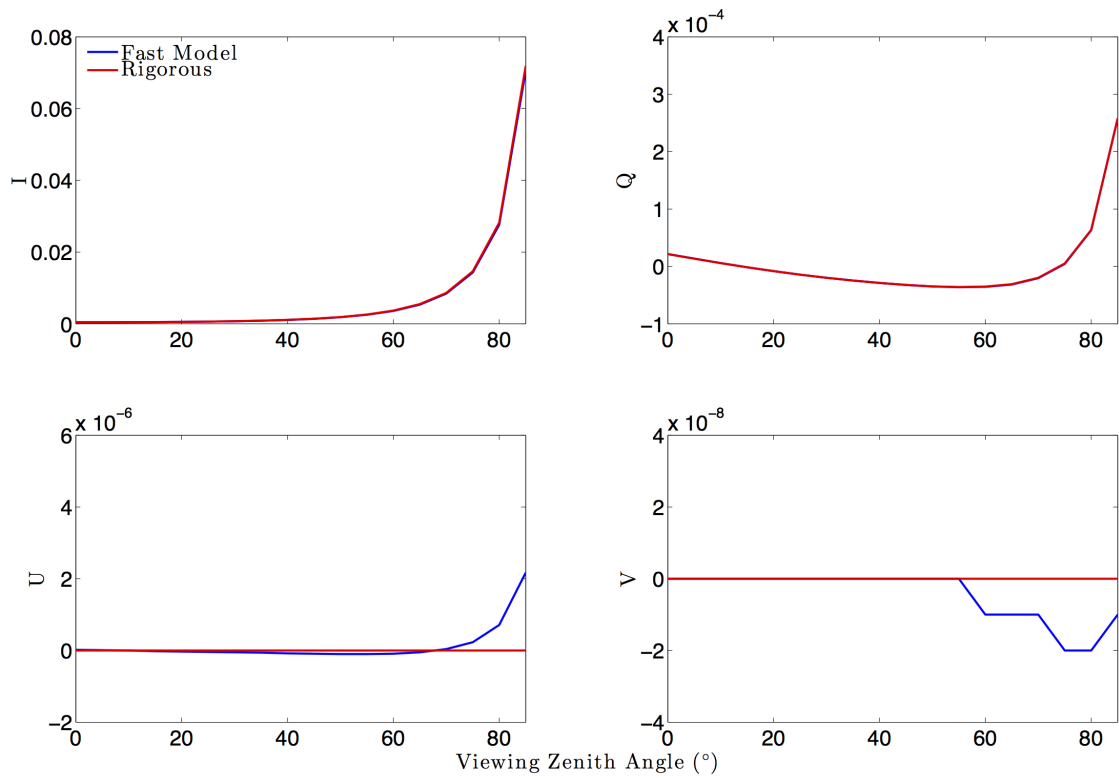


Figure 3.7: Comparison of the Stokes vectors (I,Q,U,V) of upward radiances at the TOA calculated by the fast model and the rigorous adding-doubling method. The model here is a thin dust aerosol layer above a black surface. The solar zenith angle is 60° and the relative azimuthal angle is 0° .

spherical dust aerosols, this forward model would be used to simulate the radiance and polarized measurements of satellites at the TOA.

4. RETRIEVAL OF NON-SPHERICAL DUST AEROSOL PROPERTIES USING COLLOCATED POLDER/PARASOL-MODIS/AQUA MEASUREMENTS

4.1 Introduction

The multi-angular radiance and polarized measurements from the POLDER/PARASOL provide an unprecedented opportunity to retrieve information of non-spherical dust aerosols. The abundant measurements are capable of retrieving more interested aerosol properties uniquely with a higher precision ([36]). At the mean time, the MODIS/Aqua has proved its capability for detection of dusty pixels and cloud masking with its relative high spatial resolution and wide spectral range. Some technical information about the POLDER/PARASOL and the MODIS/Aqua are listed in the table 4.1. The complimentary features of the two instruments suggest that the use of the collocated MODIS/Aqua and POLDER/PARASOL product may bring us a more accurate retrieval.

What comes together with the opportunity brought by the multi-angular radiance and polarized measurements is a challenge to the widely used LUT technique in the retrieval. Traditionally, the number of the retrievable parameters is limited and the precision of the retrieval results is low. The dimension of the corresponding LUT

Table 4.1: Technical features of POLDER/PARASOL and MODIS/Aqua.

| | POLDER/PARASOL | MODIS/Aqua |
|--------------------|--------------------------------|-------------------|
| Viewing Directions | up to 16 directions | single direction |
| Polarization | linear polarization at 3 bands | no polarization |
| Spatial Resolution | 6 × 6 km | 1 × 1 km |
| Spectral Range | 0.443-0.908 μm | 0.4-15 μm |

is small and affordable. Considering the capability of the POLDER/PARASOL, the dimensions of the high-resolution LUT are so huge that makes the required storage volume tremendous. For example, suppose that we want to retrieve only 5 parameters at the same time, then the dimension of the LUT would be 5 plus 3 (that is the number of angles related to the viewing and solar geometries). If the resolution for each dimension is only 100 points, we end up with a astronomical figure 100^{5+3} . Therefore, in the new retrieval algorithm, we substitute the traditional LUT technique with an iterative Levenberg-Marquardt method. Using the aforementioned efficient and accurate forward model and the Levenberg-Marquardt method, it is possible to retrieve surface properties as well as dust aerosol properties, such as the aerosol optical depth, the multi-mode particle size distribution, and the shape of dust aerosol, simultaneously and continuously.

The remaining part of this section is organized as follows. In Subsection 4.2, we introduce a detection algorithm for dusty pixels, which would be used in the following study, using MODIS/Aqua measurements. In Subsection 4.3, we present a sensitivity study of multi-angular radiance and polarized measurements of the POLDER/PARASOL. In Subsection 4.4, a detailed description of our aerosol retrieval algorithm is provided. The atmospheric gaseous correction is first given. As the core algorithm, the Levenberg-Marquardt method is then introduced. All the procedures of the retrieval process are shown, followed by a test of the retrieval algorithm. Some interesting results of the retrieved non-spherical dust aerosol properties over the Sahara Desert are presented. In the last Subsection, we briefly summarize the main features of the new aerosol retrieval algorithm.

4.2 Detection of Dusty Pixels with MODIS/Aqua

The first step for the retrieval of dust aerosols is to detect dusty pixels from satellite observations. Considering the limited spatial resolution and spectral range of the POLDER/PARASOL, we collocate the MODIS/Aqua data with the POLDER/PARASOL data, and use the former for dusty pixel detection.

Over ocean, the detection can be achieved by using the MODIS level 1B Calibrated Geo-located Radiances and level 2 Cloud Mask products. The following parameters of MODIS/Aqua data are used to discriminate dusty pixels from others via a QDA (quadratic discriminant analysis) based statistical method: the standard deviation of channel 5, brightness temperature difference of channel 29 and 31, brightness temperature difference of channel 31 and 32, NDDI index, NDVI index, and reflectance ratio between channel 3 and channel 1 ([5]). As is shown in Figure 4.1, dust aerosols that are blown away from the west coast area of North Africa and clearly observed in the MODIS RGB image, are successfully recognized by this algorithm.

Over land, the above dusty pixel detection algorithm is not valid, since the signal from the complicated high reflective land surface may blur the signal from the dust aerosols. On the other hand, it has been found that the land surface is quite dark in the MODIS Deep Blue channels due to the relatively strong absorption of dust aerosols in the near UV and the blue spectrum. Therefore, we use the MODIS Deep Blue aerosol product to discriminate dusty pixels over land. Figure 4.2 shows the aerosol optical depth derived in the MODIS Deep Blue product over the Sahara Desert compared with the corresponding MODIS RGB image, where a strong dust storm can be observed around 2° East and 12° north.

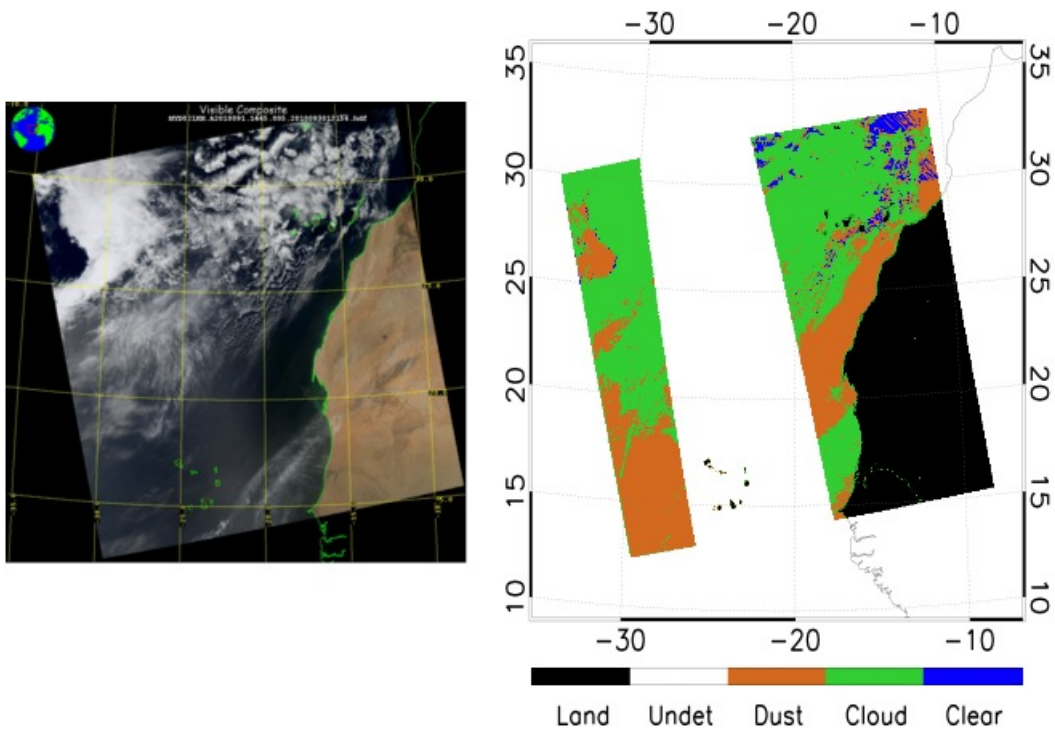


Figure 4.1: Comparison between the MODIS RGB image (left panel) and the result of dusty pixel detection (right panel) for the west coast area of North Africa on April 1, 2010. The white gap in the right panel is due to the sun glint.

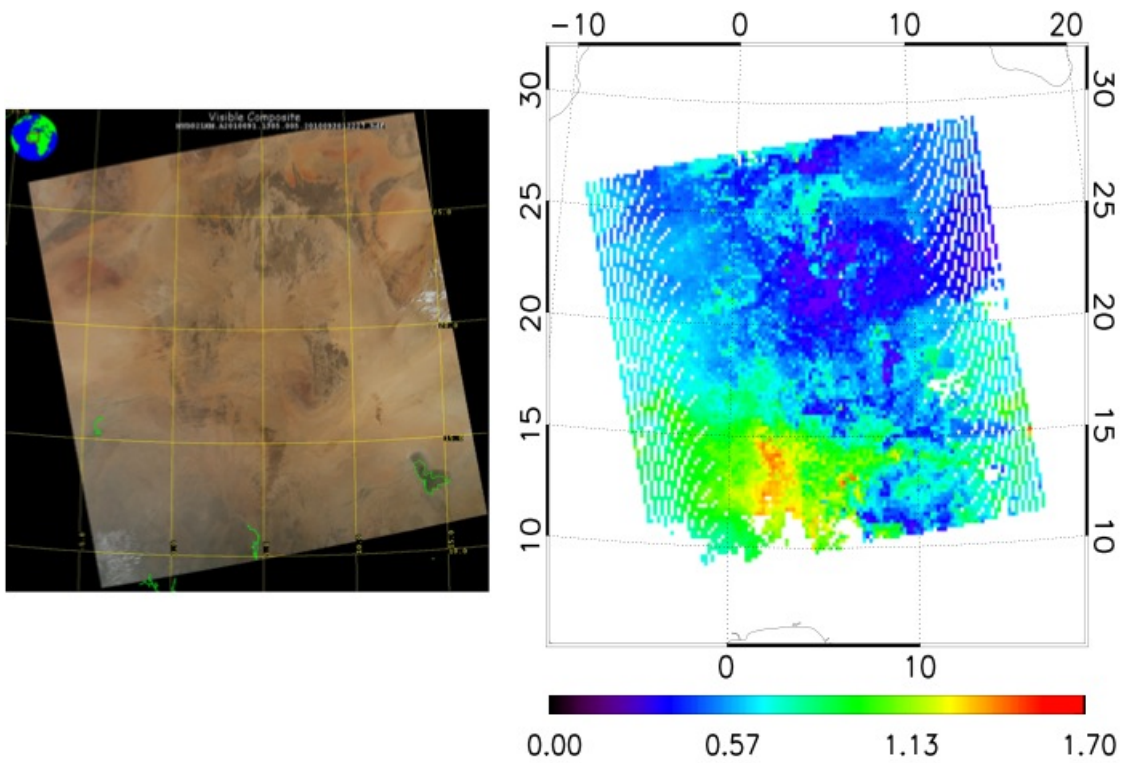


Figure 4.2: Comparison between the MODIS RGB image (left panel) and aerosol optical depth derived in the MODIS Deep Blue product (right panel) over the Sahara Desert on April 1, 2010.

4.3 Sensitivity of Multi-Angular Radiance and Polarized Measurements of POLDER/PARASOL

With the detected dusty pixels, the sensitivity of multi-viewing-directional polarized measurements of the POLDER/PARASOL to the microphysical properties of dust aerosols can be studied. For this purpose, we consider the normalized radiance $R(\theta_v, \theta_s, \phi)$ and the normalized polarized radiance $R_p(\theta_v, \theta_s, \phi)$ in the POLDER/PARASOL level 2 Earth Radiation Budget, Water Vapor and Clouds product. The definition of the two parameters are given by:

$$R(\theta_v, \theta_s, \phi) = \frac{\pi I(\theta_v, \theta_s, \phi)}{F_0}, \quad (4.1)$$

$$R_p(\theta_v, \theta_s, \phi) = \text{sgn} \frac{\pi \sqrt{Q^2 + U^2} \cos \theta_s + \cos \theta_v}{F_0 \cos \theta_s}, \quad (4.2)$$

where θ_v is the viewing zenith angle, θ_s is the solar zenith angle, ϕ is the relative azimuthal angle between the solar and viewing directions, and F_0 is the incident solar flux at the TOA. In the equation (4.2) the sgn is determined by the angle between the direction of the polarization and the normal direction of the scattering plane ξ : If $\xi \in [0, \pi/4] \cup [3\pi/4, \pi]$, $\text{sgn} = +1$; Otherwise, $\text{sgn} = -1$.

For dust aerosols over ocean, we consider the measurements of the channel 865P, where the signal from the ocean can be ignored. As is shown in Figure 4.3, the spheroidal model of dust aerosol can properly reproduce the angular feature of normalized radiance measured by the POLDER/ PARASOL over the global ocean on April 1, 2010, while the simulation results using spherical model deviate from the measurements at large scattering angles (e.g. $> 150^\circ$). In Figure 4.4, a similar situation is found for the polarization. It is worthwhile to notice that the spheroidal model can even correctly predict the position of the neutral point of the polarization

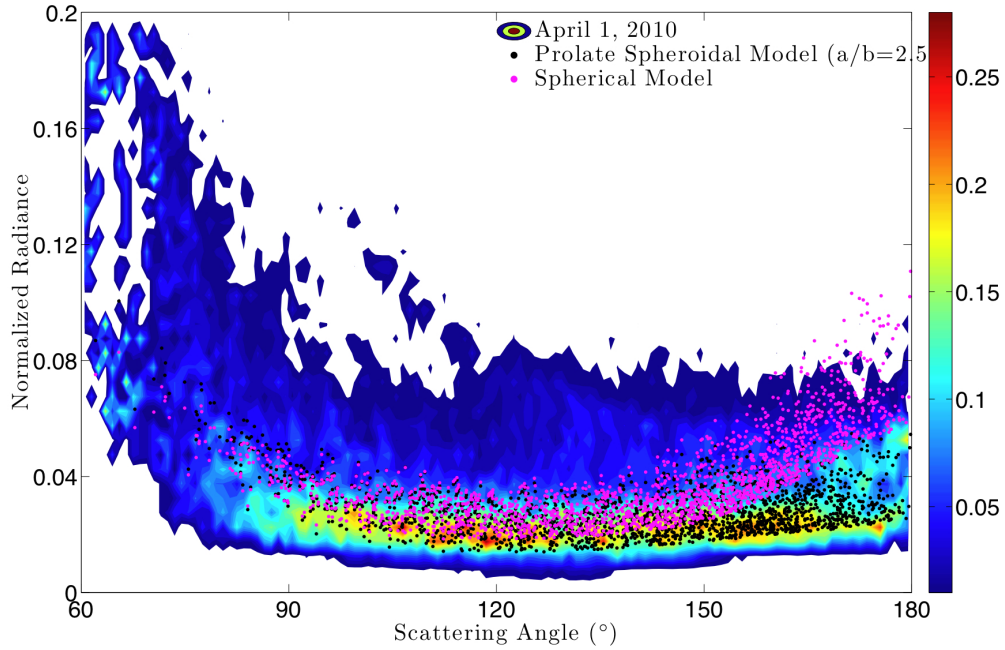


Figure 4.3: Comparison between simulations of normalized radiance using the spherical model and the spheroidal model with the aspect ratio 2.5. The contour is obtained from the actual measurements from the POLDER/PARASOL over global ocean on April 1, 2010, with the value defined as the number of observations at the particular scattering angle and with the particular value of normalized radiance divided by the total number of observations at the particular scattering angle.

around 160° .

The measurements of the channel 670P are used for dust aerosol retrieval over land. In Figure 4.5, it is shown that the normalized radiances measured by the POLDER/PARASOL over the Sahara Desert on April 1, 2010 are almost angular-independent with a large dispersion in the vertical axis, since radiance is very sensitive to different surface properties and optical depths of different pixels. On the other hand, the measurements of normalized polarized radiance shows a strong angular dependence, which is very sensitive to the shape (aspect ratio) of dust aerosol but is less sensitive to aerosol optical depth (see Figure 4.6 and Figure 4.7). Moreover,

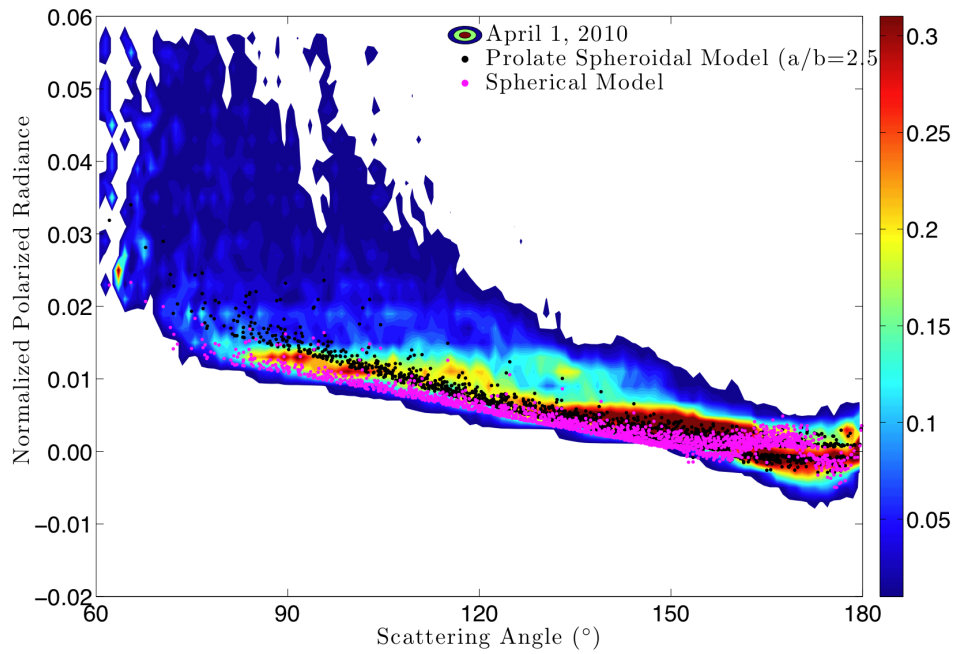


Figure 4.4: Comparison between simulations of normalized polarized radiance using the spherical model and the spheroidal model with the aspect ratio 2.5. The contour is obtained from the actual measurements from the POLDER/PARASOL over global ocean on April 1, 2010 with the value defined as the number of observations at the particular scattering angle and with the particular value of normalized polarized radiance divided by the total number of observations at the particular scattering angle.

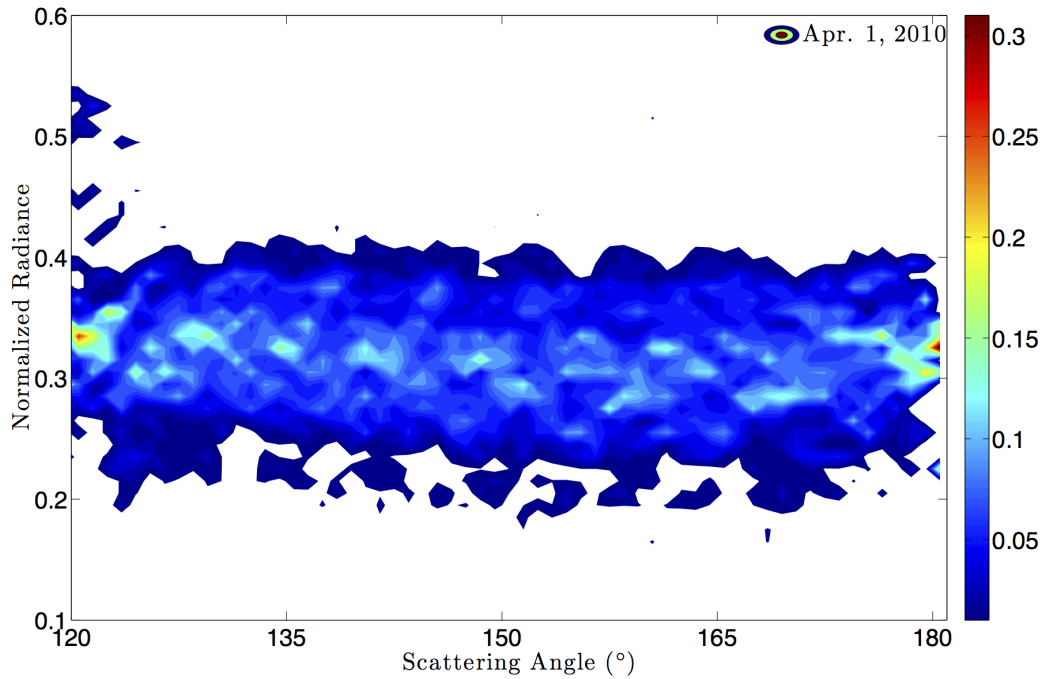


Figure 4.5: Angular dependence of normalized radiances measured by the POLDER/PARASOL over the Sahara Desert on April 1, 2010.

the normalized polarized radiance shows little sensitivity to the land surface albedo. When we doubled the surface albedo in the simulation, the results almost perfectly overlap those simulated with actual surface albedos (see Figure 4.8).

4.4 The Aerosol Retrieval Algorithm

4.4.1 Scattering and Absorption of Atmospheric Molecules

For those channels of the POLDER/PARASOL in the visible spectrum, the absorption and Rayleigh scattering due to atmospheric molecules are small but may not be ignored. It is well known that the contribution of the Rayleigh scattering to the polarized measurements is significant due to the small size of these molecules, while the influence of the molecule absorption is uncertain. In the retrieval algorithm, we exactly take into account of these effects with the LBLRTM. The high-

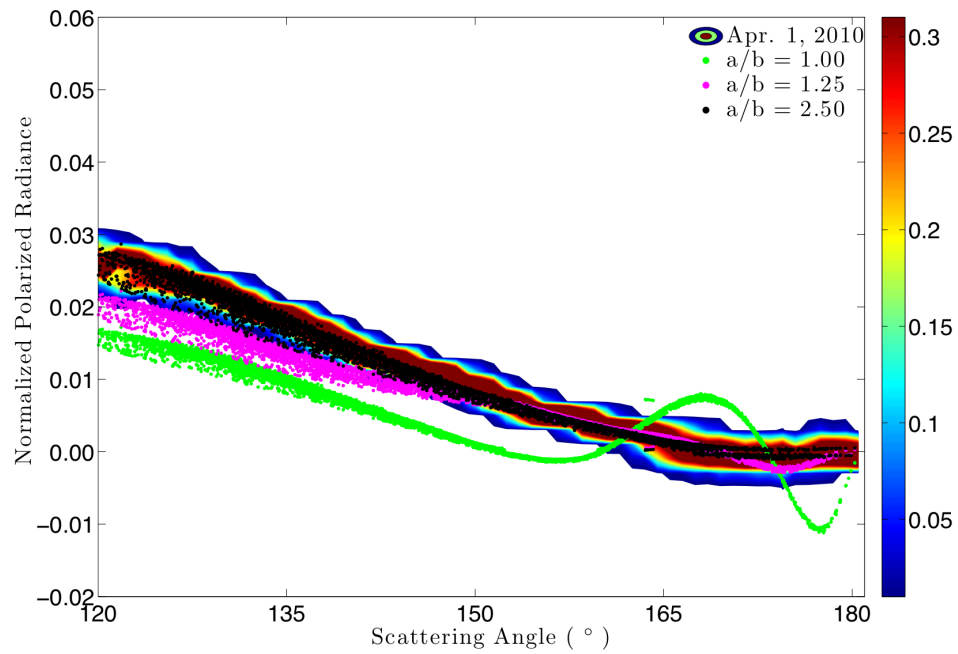


Figure 4.6: Comparison between simulations of normalized polarized radiance using spheroidal models with the aspect ratios 1.0,1.25, and 2.5. The contour is obtained from the actual measurements of the POLDER/PARASOL over the Sahara Desert on April 1, 2010.

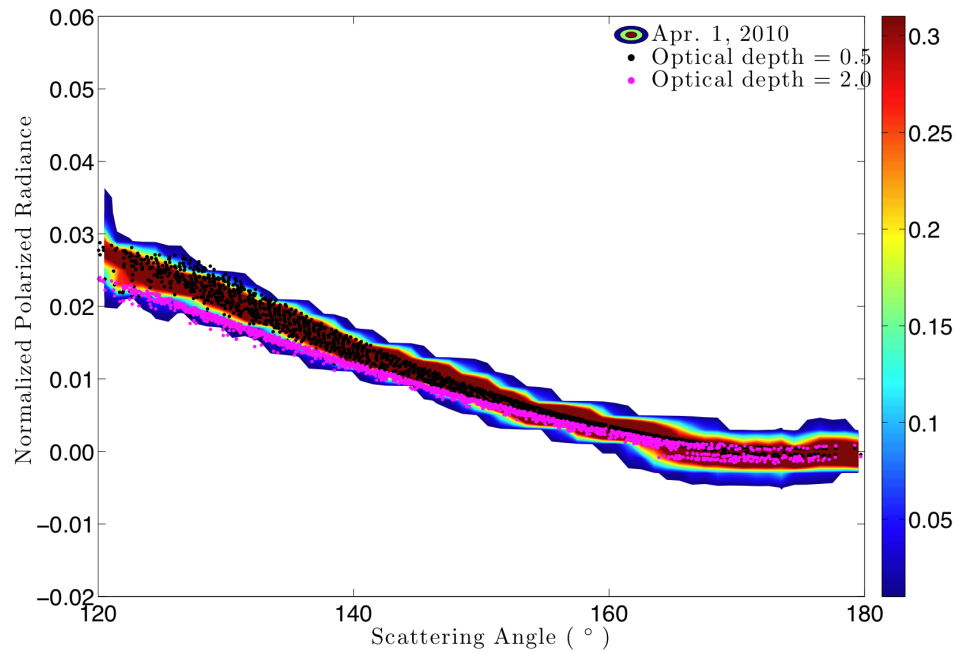


Figure 4.7: Comparison between simulations of normalized polarized radiance using the optical depths 0.5 and 2.0. The spheroidal models of dust aerosol with the aspect ratio 2.5 is adopted in these calculations. The contour is obtained from the actual measurements of the POLDER/PARASOL over the Sahara Desert on April 1, 2010.

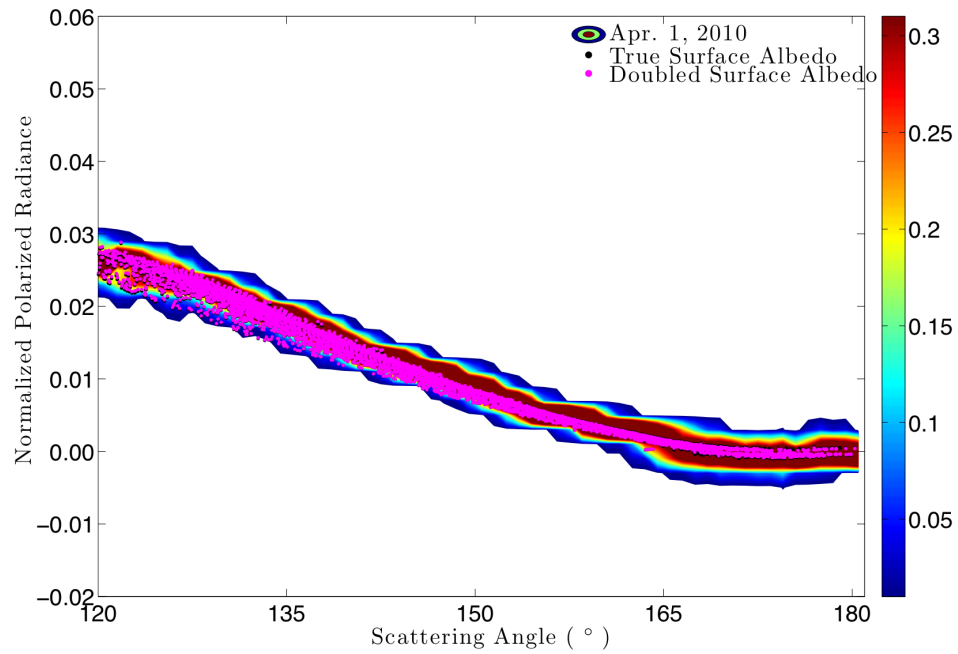


Figure 4.8: Comparison between simulations of normalized polarized radiance using the actual surface albedos and the doubled surface albedos. The spheroidal models of dust aerosol with the aspect ratio 2.5 is adopted in these calculations. The contour is obtained from the actual measurements of the POLDER/PARASOL over the Sahara Desert on April 1, 2010.

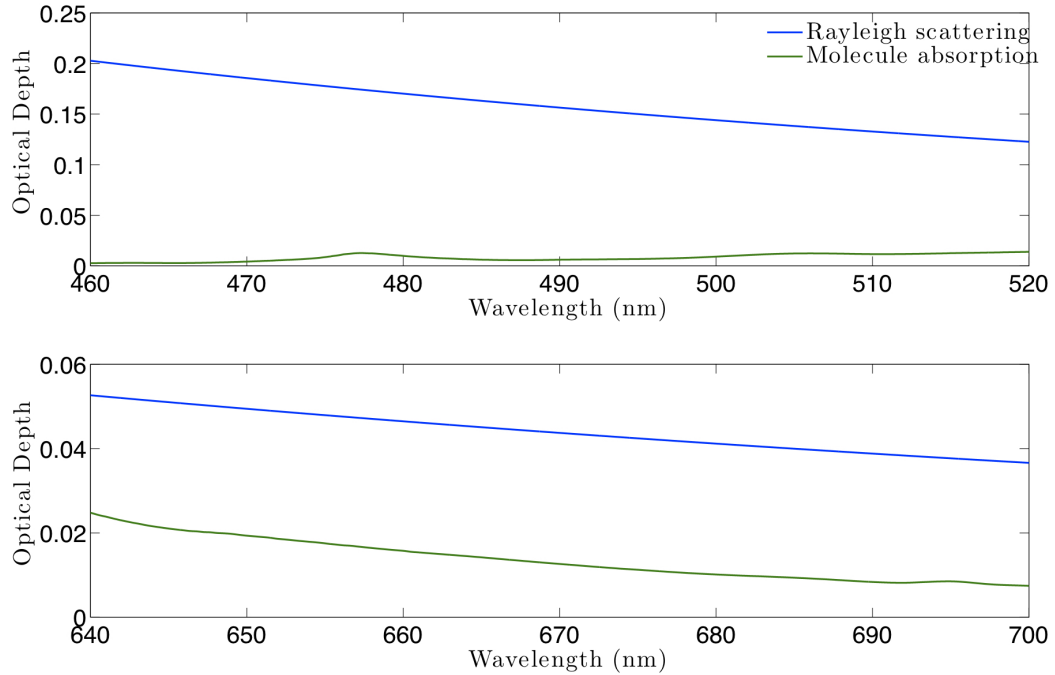


Figure 4.9: High-spectral-resolution optical depth of the Rayleigh scattering and molecule absorption around the channel 490P (top) and the channel 670P (bottom).

spectral-resolution molecule absorption and Rayleigh scattering optical thicknesses are calculated from the standard atmospheric profiles by considering 39 major atmospheric gases, such as H_2O , O_2 , O_3 , etc. The data of spectral lines are obtained from the HITRAN (High-resolution TRANsmission molecular AbsorptionN database, [13]).

As is shown in Figure 4.9, the optical depth of the Rayleigh scattering shows the dependence on wavelength⁻⁴. The value is around 0.15 for the channel 490P and 0.04 for the channel 670P. On the other hand, the absolute value of the optical depth of molecule absorption is on the order of magnitude of 0.01, which is negligible for the channel 490P, but becomes comparable to the optical depth of Rayleigh scattering for the channel 670P.

The narrow band optical depth for a particular channel of the POLDER/PARASOL, which is used in the forward radiative transfer model, can be obtained approximately from the integration of the high-spectral-resolution transmittance weighted by the response function $f(\lambda)$ of the channel:

$$\bar{\tau}_{\text{Rayleigh/absorption}} = -\log \left(\frac{\int \exp(-\tau_{\text{Rayleigh/absorption}}(\lambda)) f(\lambda) d\lambda}{\int f(\lambda) d\lambda} \right). \quad (4.3)$$

4.4.2 The Levenberg-Marquardt Method

Essentially, the aerosol retrieval is a non-linear inverse problem. Suppose the number of all the interested parameters of dust aerosols is n , and the number of the available multi-angular radiance and polarized measurements of the POLDER/PARASOL is m , then we can use an n -dimensional column vector \mathbf{x} and an m -dimensional column vector \mathbf{y} to represent these parameters and measurements, respectively. The objective of the aerosol retrieval is to find the solution \mathbf{x} to the equation

$$\mathbf{y} = \mathbf{F}(\mathbf{x}), \quad (4.4)$$

where $\mathbf{F}(\mathbf{x})$ denotes the forward radiative transfer model. Generally, $\mathbf{F}(\mathbf{x})$ is an m -dimensional non-linear vector function of \mathbf{x} and it is very difficult to find the inverse function $\mathbf{F}^{-1}(\mathbf{y})$ so that

$$\mathbf{x} = \mathbf{F}^{-1}(\mathbf{y}). \quad (4.5)$$

Alternatively, we define a scalar error function $S(\mathbf{x})$ as

$$S(\mathbf{x}) = \frac{\sum_{i=1}^m w_i [y(\theta_{s,i}, \theta_{v,i}, \phi_i) - F(\theta_{s,i}, \theta_{v,i}, \phi_i; \mathbf{x})]^2}{\sum_{i=1}^m w_i}, \quad (4.6)$$

where w_i is equal to the inverse squared error of the i th measurement. Then the

inverse problem becomes a least square super-curve fitting problem: Given a set of pairs $\{[(\theta_{s,i}, \theta_{v,i}, \phi_i), y_i], i = 1, \dots, m\}$, we optimize the parameters $\{x_i, i = 1, \dots, n\}$ of the modeled super-curve $F(\theta_{s,i}, \theta_{v,i}, \phi_i; \mathbf{x})$ so that the function $S(\mathbf{x})$ becomes minimal.

In mathematics, the Levenberg-Marquardt algorithm provides a numerical solution to such minimization problem. Given an initial guess that is sufficiently close to the final solution of the parameter vector, the final solution can be obtained iteratively. Supposing that the current parameter vector is \mathbf{x} , a correction $\Delta\mathbf{x}$ that would result in a better estimation $\mathbf{x} + \Delta\mathbf{x}$, is given by

$$(\mathbf{J}^T \mathbf{J} + \lambda \mathbf{D}) \Delta \mathbf{x} = \mathbf{J}^T [\tilde{\mathbf{y}} - \tilde{\mathbf{F}}(\mathbf{x})], \quad (4.7)$$

where λ is the so-called damping factor that is adjustable to facilitate fast convergence; the superscript “ T ” denotes the transpose of the matrix; the elements of the m -dimensional vector $\tilde{\mathbf{y}}$, $\tilde{\mathbf{F}}$ are given by

$$\tilde{y}_i = \sqrt{\frac{w_i}{\sum_{i=1}^m w_i}} y_i, \quad (4.8)$$

$$\tilde{F}_i = \sqrt{\frac{w_i}{\sum_{i=1}^m w_i}} F_i, \quad (4.9)$$

for $i = 1, \dots, m$. Here the \mathbf{J} is the $m \times n$ Jacobian matrix with elements

$$J_{ij} = \frac{\partial \tilde{F}_i(\mathbf{x})}{\partial x_j}, \quad \text{for } i = 1, \dots, m \text{ and } j = 1, \dots, n. \quad (4.10)$$

\mathbf{D} is a diagonal $n \times n$ matrix with elements

$$D_{ij} = \delta_{ij} (\mathbf{J}^T \mathbf{J})_{ij}, \quad \text{for } i = 1, \dots, m \text{ and } j = 1, \dots, n. \quad (4.11)$$

If $m > n$, the inverse problem is an ill-conditioned problem. In this circumstance, the Levenberg-Marquart method suffers from the multiple minima (or non-uniqueness) problem, and may not provide the correct solution. When using the multi-angular radiance and polarized measurements, the number of viewing directions is up to 16 and for each direction there are 3 components of the Stokes vector (I, Q, U) available. At the mean time, the number of interested aerosol parameters is usually smaller than 10. Therefore, $n \gg m$ so that the non-uniqueness problem is greatly relieved.

In the aerosol retrieval, in order to accelerate the convergence of the iteration and prevent the non-uniqueness problem, we usually impose constraint for each parameter. For example, if it is required to satisfy conditions $x_i \in [x_i^{\text{MIN}}, x_i^{\text{MAX}}]$ for $i = 1, \dots, n$, we define a new unconstrained parameter vector $\tilde{\mathbf{x}}$ with elements

$$\tilde{x}_i = \tan \left[\pi \left(\frac{x_i - x_i^{\text{MIN}}}{x_i^{\text{MAX}} - x_i^{\text{MIN}}} - \frac{1}{2} \right) \right], \quad \text{for } i = 1, \dots, n. \quad (4.12)$$

Then the Jacobian matrix \mathbf{J} in the equation (4.7) becomes $\tilde{\mathbf{J}}$ with elements defined as

$$\tilde{J}_{ij} = \frac{\partial \tilde{F}_i(\tilde{\mathbf{x}})}{\partial \tilde{x}_j}, \quad \text{for } i = 1, \dots, m \text{ and } j = 1, \dots, n. \quad (4.13)$$

4.4.3 A Description of the New Aerosol Retrieval Algorithm

With all the previous efforts, we finally develop a new aerosol retrieval algorithm for non-spherical dust aerosols. The flow chart is shown in Figure 4.10. For a pixel, the optical depths of Rayleigh scattering and absorption due to atmospheric molecules are almost invariant with time. Before the retrieval process, these properties are pre-calculated using the LBLRTM from the HITRAN considering a standard atmospheric profile for each channel of the POLDER/PARASOL. We start the re-

trieval algorithm with the MODIS Deep Blue aerosol product. We first collocate the MODIS Deep Blue product with the POLDER/PARASOL level 1 product and perform the cloud masking to exclude cloud-contaminated pixels and to detect dusty pixels. Meanwhile, the aerosol optical thickness and the surface reflectance provided by the MODIS Deep Blue product with other randomly generated aerosol parameters are chosen as the initial guess to the iteration. In the iterative retrieval process, with these parameters related to the aerosol properties, the narrowband bulk scattering properties of the bi-modal non-spherical dust aerosols could be generated from the incorporated single-scattering database for each satellite channel; With these parameters related to the surface properties, the surface BRDF could be calculated from the imbedded surface BRDF library. All these information are then imported to the forward radiative transfer model where the multi-angular Stokes vectors of the reflected radiance at the TOA are simulated using the adding-doubling method to compare with the corresponding measurements in the POLDER/PARASOL level 1 product. If the minimum of the error function is reached or a required precision is achieved, the process stops and all the retrieved aerosol and surface properties are obtained simultaneously. Otherwise, we use the Levenberg-Marquardt method to calculate corrections to all the parameters and repeat this process until the criteria is satisfied. Usually, it takes only a few steps to obtain the convergent retrieved results. To reduce the major computational time that is spent on the calculation of the Jacobian matrix, less Gaussian quadrature could be used because it is more the sign than the magnitude of the derivatives that matters for the correction.

4.4.4 Test of the Aerosol Retrieval Algorithm

Before applying the retrieval algorithm to deal with the real satellite data, we test the capability of the retrieval algorithm using “measurements” generated by the

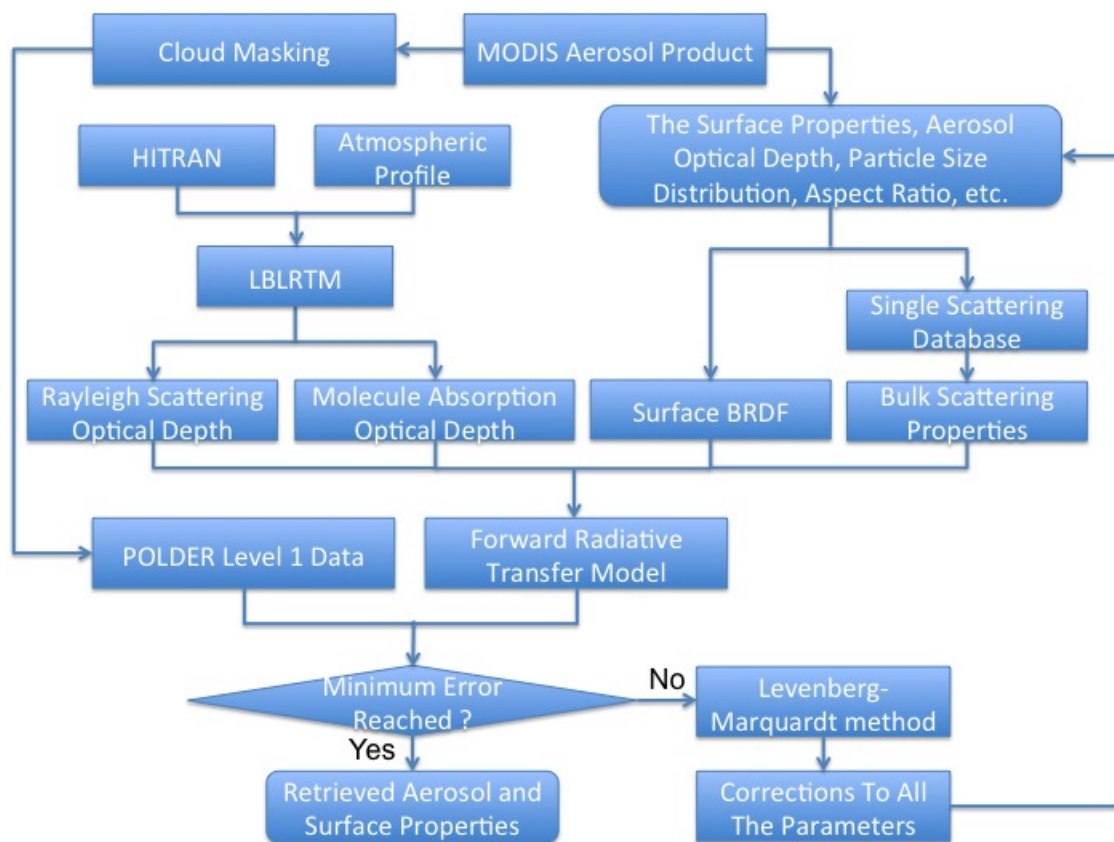


Figure 4.10: Flow chart of the new retrieval algorithm for non-spherical dust aerosols.

Table 4.2: Test of new retrieval algorithm.

| | Measurements | Initial Guess | Retrieved Results |
|----------------------------|--------------|---------------|-------------------|
| τ_{Rayleigh} | 0.05 | 0.05 | - |
| $\tau_{\text{absorption}}$ | 0.00 | 0.00 | - |
| τ_{aerosol} | 0.50 | 0.25 | 0.50 |
| A_{surface} | 0.50 | 0.25 | 0.50 |
| \bar{r} | 0.10 | 0.30 | 0.10 |
| δ | 0.30 | 0.30 | - |
| m | 1.50+0.001i | 1.50+0.001i | - |
| a/b | 1.67 | 1.00 | 1.60 |

forward radiative model of a supposed dust aerosols layer. The results are shown in the table 4.2, where τ_{Rayleigh} is the Rayleigh scattering optical depth, $\tau_{\text{absorption}}$ is the molecule absorption optical depth, τ_{aerosol} is the dust aerosol optical depth, A_{surface} is the surface albedo, \bar{r} is the mean radius of dust aerosols, δ is the standard deviation of the dust aerosol radii, m is the complex refractive index, a/b is the mean aspect ratio of dust aerosols. Notice that the surface albedo chosen in the forward model is 0.5 which is much large than the usual reflectance of the land. It implies that the signal from the land surface is so strong that it would make the aerosol retrieval much more difficult. Nevertheless, the retrieval algorithm still successfully recovers all these aerosol and surface properties with sufficient accuracy, which proves the capability of the retrieval algorithm for aerosol retrieval over the challenging source regions of dust aerosols.

4.4.5 Results

The new retrieval algorithm has been applied to investigate dust aerosol properties over the Sahara Desert. With the MODIS Deep Blue product, we found there are 320 dusty pixels with large optical depths (e.g. larger than 0.8) over this dust aerosol source region on April 1, 2010 (see Figure 4.2). After collocating the MODIS

data with the POLDER/PARASOL data, we obtain up to 15360 measurements. The statistical properties of the retrieved coarse mode size (e.g., larger than $0.5 \mu m$), fine mode size (e.g., smaller than $0.5 \mu m$), aspect ratio and single-scattering albedo are shown in Figure 4.11. There is a strong and broad peak in the histogram of coarse mode size around 4 microns that agrees with laboratory measurements using diffraction laser ([53]). For the fine mode size, a strong peak is found at the lower boundary of the parameter space (e.g. $0.002 \mu m$). This feature is not an artifact and could usually be observed in a particle number size distribution ([53]). If the volume size distribution were plotted, the peak would be diminished. The shape of the histogram of the retrieved aspect ratio is strange with two unusual peaks centered at 1.5 and 1.8, respectively. In fact, the range of aspect ratio is presumed to be from 1.0 to 3.0 in the retrieval process as is suggested by laboratory studies ([24]). It is still under investigation of the reason why most retrieval results ended with the two particular aspect ratios. A reasonable possibility is that the scattering properties are so undistinguishable in the region between aspect ratio 1.5 and 1.8 that the iteration would stop once it enters this region. Nevertheless, it is able to determine that the dust aerosol aspect ratio must be within the region bounded by 1.5 and 1.8 over the Sahara Desert. The retrieved single-scattering albedo is around 0.9, which also agrees with previous work ([10]).

The retrieved parameters are first validated by examining the errors between the simulated multi-angular radiances and polarizations with the measurements of the POLDER/PARASOL. The angular distribution of the relative errors of the simulated radiances is small (mostly within $\pm 2\%$, see Figure 4.12). The angular variation of errors of polarization shows two-branches feature: one branch agrees with measurements within an error of ± 0.01 , while the other branch deviates from the zero at smaller scattering angles with errors as large as 0.03 (see Figure 4.13). The rea-

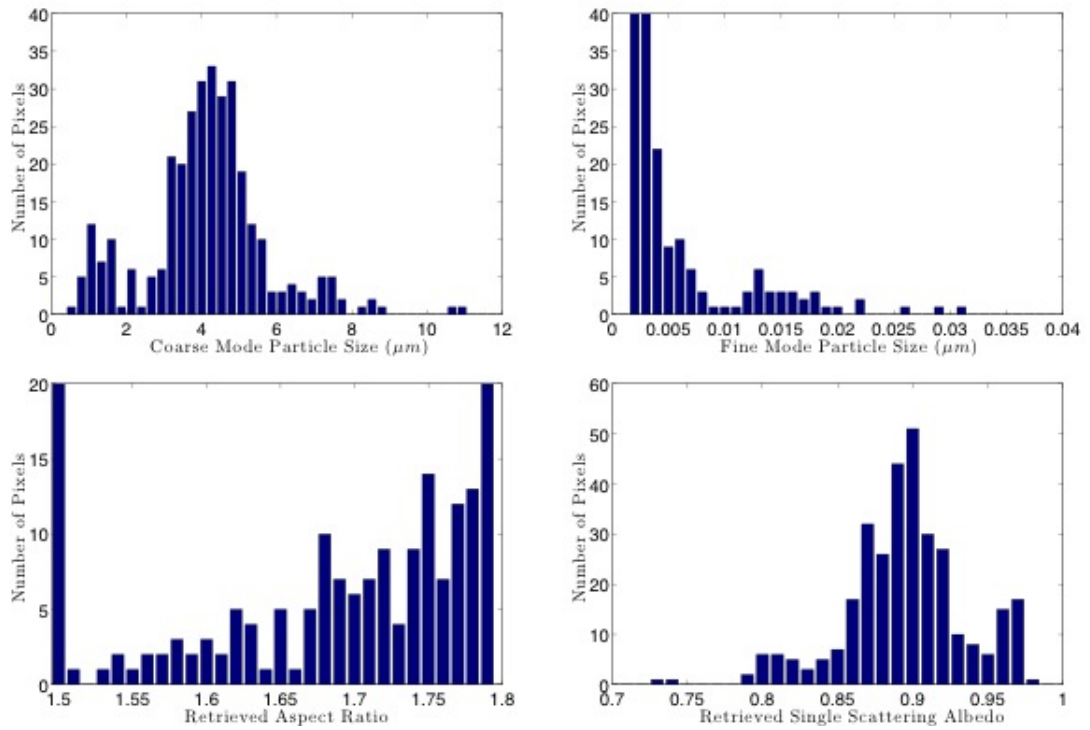


Figure 4.11: Histograms of the retrieved mean radius of the coarse mode dust aerosols, mean radius of the fine mode dust aerosols, aspect ratio, and single-scattering albedo.

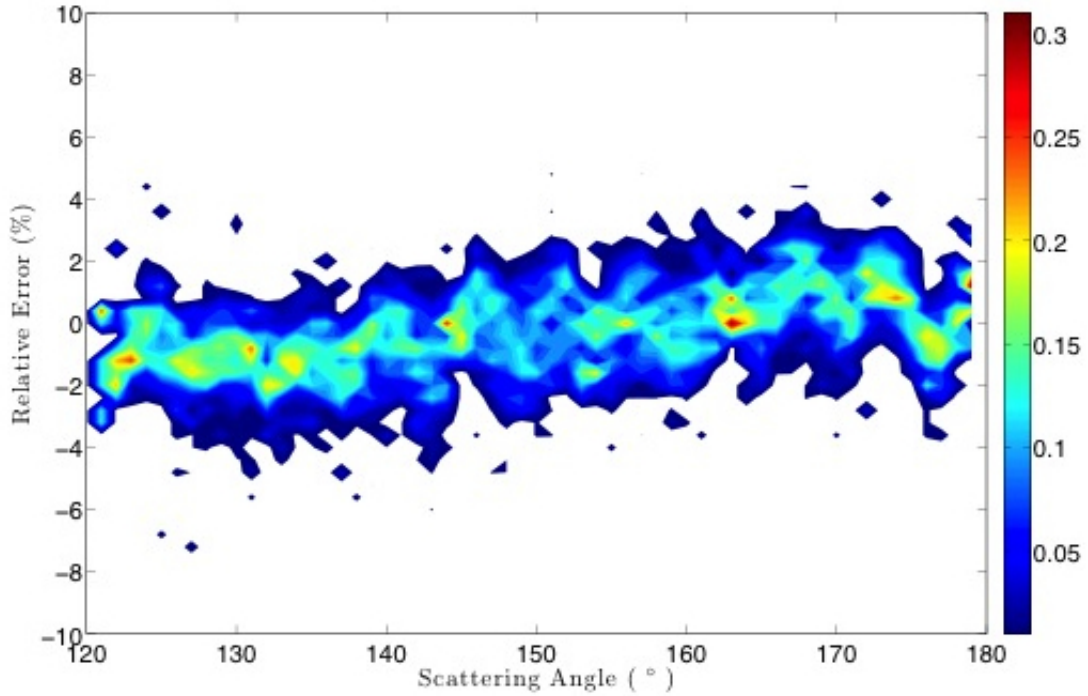


Figure 4.12: Angular variation of the relative errors of radiance, for example, $(I_{\text{simulation}} - I_{\text{measurement}})/I_{\text{measurement}}$.

son for this strange behavior is still unknown so far. An interpretation is that the spatial inhomogeneity of the atmospheric layers breaks the plane-parallel system assumption in the forward radiative transfer model. In spite of the appearance of the discrepancy, the general error of the simulation is still smaller than or comparable to the instrumental error ([15]). It implies that the retrieved dust aerosol properties are accurate at least to the extent of the instrumental precision.

It is also interesting to compare the MODIS Deep Blue product, which is based on multi-spectral single-directional radiance measurements, with our retrieved results that is based on single-wavelength multi-angular radiance and polarized measurements. As is shown in Figure 4.14, there is a strong correlation between surface reflectances retrieved from the POLDER/PARASOL and the MODIS/Aqua using

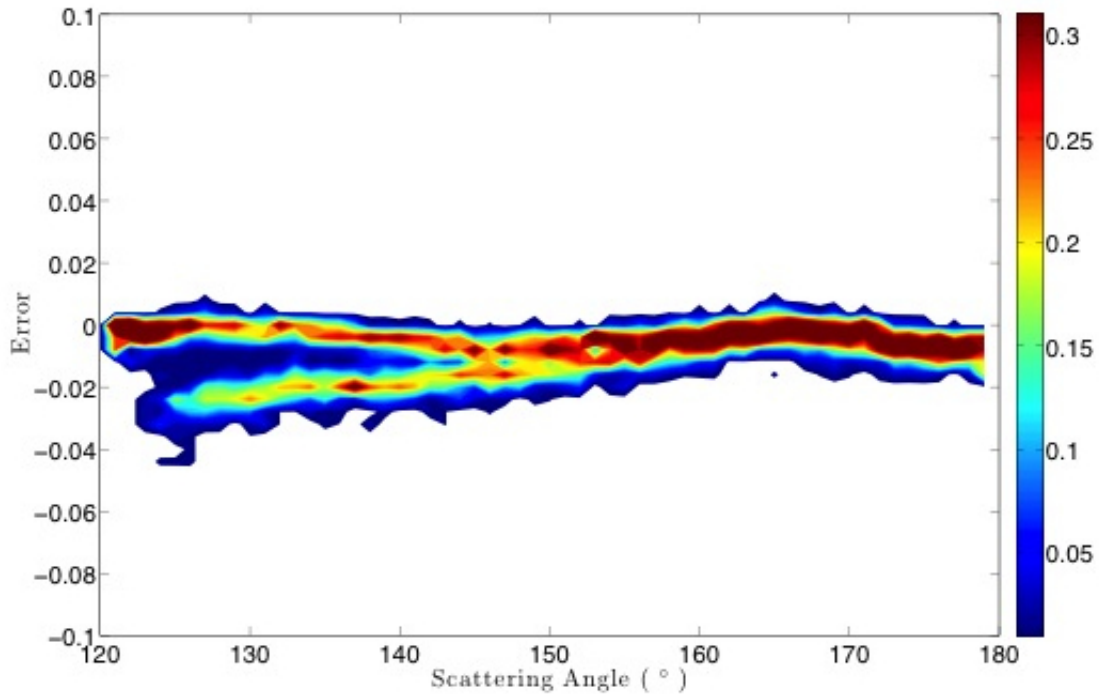


Figure 4.13: Angular variation of the errors of DoLP, for example, $DoLP_{\text{simulation}} - DoLP_{\text{measurement}}$.

completely different aerosol retrieval algorithms and sets of observables. Weaker correlation is found for the retrieved aerosol optical thickness. However, it should be noticed that we selected those optically thick dusty pixels only, where the quality of the MODIS Deep Blue product is comparatively poor, as is well known that the error bar increases with the increasing aerosol optical thickness. Besides, the range of the retrieved aerosol optical thickness is too narrow (e.g. only from 0.9 to 1.2) to represent the overall behavior. The trend of the scattered points suggests that the MODIS Deep Blue aerosol retrieval algorithm may overestimate surface reflectance and underestimate the aerosol optical thickness.

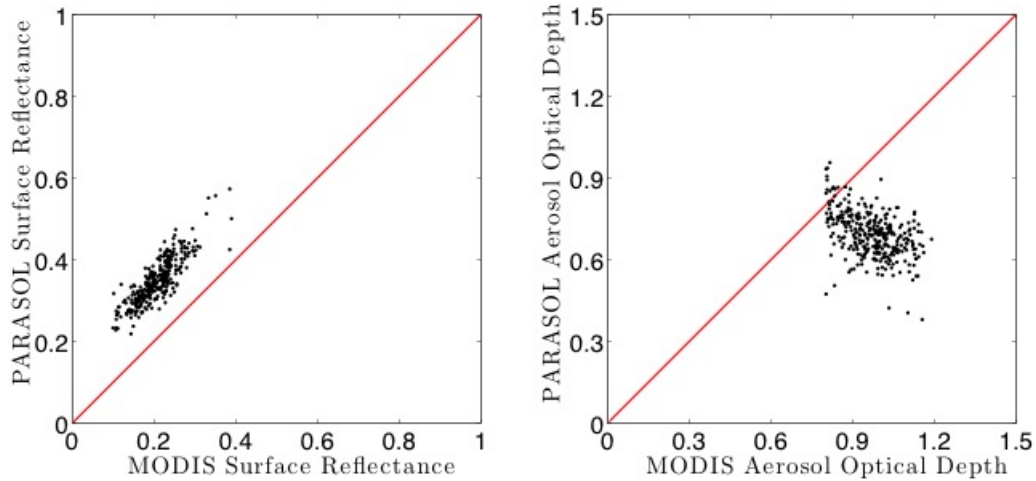


Figure 4.14: Comparison of surface reflectance and aerosol optical depth retrieved by MODIS Deep Blue algorithm and our new retrieval algorithm.

4.5 Summary

In this section, we developed a framework of a completely new retrieval algorithm for non-spherical dust aerosols. Compared with the traditional retrieval algorithms, the single-scattering properties calculation, the forward radiative transfer model, the set of input satellite data, the atmospheric gaseous correction and the retrieval technique, are all improved in the new algorithm: Instead of using limited and fixed aerosol models, we directly incorporate the newly developed single-scattering property database of tri-axial mineral dust aerosol in the retrieval algorithm; Beyond the first few orders of scattering, we fully consider the multiple scattering by solving the VRTE using the adding-doubling method in the forward model; Meanwhile, a BRDF library is imbedded in the forward model to consider various surface conditions; To relief the non-uniqueness problem in the aerosol retrieval, the multi-angular radiance and polarized measurements of the POLDER/PARASOL are used; Considering the limited spectral range and spatial resolution, the MODIS Deep Blue product is collo-

cated to perform cloud masking and detection of dusty pixel; In addition, an iterative retrieval algorithm based on the Levenberg-Marquardt method is employed to allow for retrieving a collection of aerosol parameters continuously and simultaneously.

5. SUMMARY AND FUTURE WORK

In this dissertation, a framework of a completely new retrieval algorithm for non-spherical dust aerosols was developed. Compared with the traditional retrieval algorithms, improvements are recognized in the following aspects: Instead of using limited and fixed aerosol models, we directly incorporate the newly developed single-scattering properties database of tri-axial mineral dust aerosol in the retrieval algorithm; Beyond the first few orders of scattering, we fully consider the multiple scattering by solving the VRTE using the adding-doubling method in the forward model; Meanwhile, a BRDF library is imbedded in the forward model to consider various surface conditions; To relief the non-uniqueness problem in the aerosol retrieval, the multi-angular radiance and polarized measurements of the POLDER/PARASOL are used; Considering the limited spectral range and spatial resolution, the MODIS Deep Blue product is collocated to perform cloud masking and detection of dusty pixel; In addition, an iterative retrieval algorithm based on the Levenberg-Marquardt method is employed to allow for retrieving a large collection of aerosol parameters continuously and simultaneously.

In Section 2, as an effort for solving light scattering problems of spheroidal particles, a new algorithm for the calculation of spheroidal functions was developed. The narrowband bulk scattering properties of dust aerosols for satellite remote sensing were obtained by using the newly developed single-scattering property database of mineral dust aerosols, which was incorporated in our aerosol retrieval algorithm.

As a study to improve the forward model in aerosol retrieval, in Section 3, an adding-doubling code is developed to solve the VRTE. The high efficiency of the code is achieved through the following ways: (a) The adding equations are realized

in the supermatrix form and supermatrix multiplications are handled with the BLAS; (b) The first order scattering is separated in the multiple scattering calculation to accelerate convergence of Fourier series; (c) The expansion of the phase matrix of dust aerosol in the generalized spherical functions can be truncated using delta-M method if necessary; (c) If a moderate precision is acceptable, all the integrations can be conducted on an icosahedral grid to further speed up the code. For the purpose of simulating reflection properties of diverse land and ocean surfaces, a surface BRDF library is embedded into the code.

In Section 4, the dusty pixel detection and cloud masking using the MODIS Deep Blue product were introduced. The sensitivity of multi-angular polarized and radiance measurements to the non-spherical dust aerosol was also investigated. The atmospheric gaseous correction was conducted with the LBLRTM. With all these efforts, we developed the new aerosol retrieval algorithm based on the Levenberg-Marquardt method. As an application, we used the new algorithm to derive properties of non-spherical dust aerosols over the Sahara Desert, such as the aerosol optical depth, fine mode mean radius, coarse mode mean radius, coarse mode fraction, aspect ratio, and single-scattering albedo.

In our future work, further validations of the new dust aerosol retrieval algorithm are required. The retrieval results from the AERONET (AERosol RObotic NETwork) are usually regarded as the benchmark for the satellite retrieval. Unlike the space-borne instruments which measuring mainly the backward scattering due to the limitation of observation geometry, the ground-based AERONET can measure the forward scattering. It would be interesting to compare our results with the long-term AERONET product. In the framework of the new retrieval algorithm, the non-spherical dust aerosol database could be improved by introducing some newly developed models of dust aerosol particles, such as fractal. It is found that the

spheroidal model works fine for the single-band retrieval, but may be inconsistent in the multi-band retrieval. To investigate multi-band dust aerosol retrieval algorithm, we have to improve the single-scattering database. Instead of confining ourself to those clear pixels uncontaminated by ice or water clouds, we may investigated the interaction between cloud and dust aerosol if a single-scattering property database of ice and water cloud is also incorporated. By implementing more surface BRDF models in our surface BRDF library, such as models for snow covered surface, vegetated land surface, urban surface, shallow water, etc, more applications would be explored to retrieve dust aerosol properties over various land and water surfaces under various cloud conditions.

REFERENCES

- [1] C. N. Adams, and G. W. Kattawar, “Solutions of the equations of radiative transfer by an invariant imbedding approach,” *Journal of Quantitative Spectroscopy and Radiative Transfer* **10**, 341-356 (1970).
- [2] L. Bi, P. Yang, G. W. Kattawar, and R. Kahn, “Single-scattering properties of triaxial ellipsoidal particles for a size parameter range from the Rayleigh to geometric-optics regimes,” *Applied Optics* **48**, 114-126 (2008).
- [3] C. F. Bohren, and D. R. Huffman, *Absorption and scattering of light by small particles* (Wiley-VCH, 2008).
- [4] S. Chandrasekhar, *Radiative transfer* (Courier Dover Publications, 1960).
- [5] H.-M. Cho, S. L. Nasiri, P. Yang, I. Laszlo, and X. T. Zhao, “Detection of optically thin mineral dust aerosol layers over the ocean using MODIS,” *Journal of Atmospheric and Oceanic Technology* **30**, 896-916 (2013).
- [6] J. Chowdhary, L. D. Travis, and A. A. Lacis, “Incorporation of a rough ocean surface and semi-infinite water body in multiple scattering computations of polarized light in an atmosphere-ocean system,” *Atmospheric Sensing and Modeling* **2311**, 58-70 (1995).
- [7] C. Cox, and W. Munk, “Statistics of the sea surface derived from sun glitter,” *Journal of Marine Research* **13**, 198-227 (1954).
- [8] J. L. Deuzé, F. M. Bréon, C. Devaux, P. Goloub, M. Herman, B. Lafrance, F. Maignan, A. Marchand, F. Nadal, G. Perry, and D. Tanré, “Remote sensing of aerosols over land surfaces from POLDER-ADEOS-1 polarized measurements,” *Journal of Geophysical Research* **106**, 4913-4926 (2001).

- [9] O. Dubovik, A. Sinyuk, T. Lapyonok, B. N. Holben, M. Mishchenko, P. Yang, T. F. Eck, H. Volten, O. Munoz, B. Veihelmann, W. J. van der Zande, J. F. Leon, M. Sorokin, and I. Slutsker, “Application of spheroid models to account for aerosol particle nonsphericity in remote sensing of desert dust,” *Journal of Geophysical Research-Atmospheres* **111(D11208)**, 1-34 (2006).
- [10] T. F. Eck, “Variability of biomass burning aerosol optical characteristics in southern Africa during the SAFARI 2000 dry season campaign and a comparison of single scattering albedo estimates from radiometric measurements,” *Journal of Geophysical Research* **108(D13)**, 8477-8497 (2003).
- [11] P. E. Falloon, P. C. Abbott, and J. B. Wang, “Theory and computation of spheroidal wavefunctions,” *Journal of Physics A: Mathematical and General* **36**, 5477-5495 (2003).
- [12] V. G. Farafonov, V. B. Il’in, and A. A. Vinokurov, “On use of the field expansions in terms of spheroidal functions,” *Journal of Quantitative Spectroscopy and Radiative Transfer* **106**, 33-43 (2007).
- [13] J. Fischer, R. R. Gamache, A. Goldman, L. S. Rothman, and A. Perrin, “Total internal partition sums for molecular species in the 2000 edition of the HITRAN database,” *Journal of Quantitative Spectroscopy and Radiative Transfer* **82**, 401-412 (2003).
- [14] C. Flammer, *Spheroidal wave functions* (Stanford University Press, 1957).
- [15] B. Fougnie, G. Bracco, B. Lafrance, C. Ruffel, O. Hagolle, and C. Tinel, “PARASOL in-flight calibration and performance,” *Applied Optics* **46**, 5435-5451 (2007).

- [16] J. F. d. Haan, P. B. Bosma, and J. W. Hovenier, "The adding method for multiple scattering calculations of polarized light," *Astronomy and Astrophysics* **183**, 371-391 (1987).
- [17] O. P. Hasekamp, and J. Landgraf, "Retrieval of aerosol properties over land surfaces: capabilities of multiple-viewing-angle intensity and polarization measurements," *Applied Optics* **46**, 3332-3344 (2007).
- [18] J. Haywood, and O. Boucher, "Estimates of the direct and indirect radiative forcing due to tropospheric aerosols: A review," *Reviews of Geophysics* **38**, 513-543 (2000).
- [19] R. Heikes, and D. A. Randall, "Numerical Integration of the Shallow-Water Equations on a Twisted Icosahedral Grid. Part I: Basic Design and Results of Tests," *Monthly Weather Review* **123**, 1862-1880 (1995).
- [20] D. B. Hodge, "Eigenvalues and Eigenfunctions of the Spheroidal Wave Equation," *Journal of Mathematical Physics* **11**, 2308-2312 (1970).
- [21] N. C. Hsu, S. C. Tsay, M. D. King, and J. R. Herman, "Aerosol properties over bright-reflecting source regions," *IEEE Transactions on Geoscience and Remote Sensing* **42**, 557-569 (2004).
- [22] Y. X. Hu, B. Wielicki, B. Lin, G. Gibson, S. C. Tsay, K. Stamnes, and T. Wong, "Delta-Fit: A fast and accurate treatment of particle scattering phase functions with weighted singular-value decomposition least-squares fitting," *Journal of Quantitative Spectroscopy and Radiative Transfer* **65**, 681-690 (2000).
- [23] H. Iwabuchi, and T. Suzuki, "Fast and accurate radiance calculations using truncation approximation for anisotropic scattering phase functions," *Journal of Quantitative Spectroscopy and Radiative Transfer* **110**, 1926-1939 (2009).

- [24] K. Kandler, L. Schütz, C. Deutscher, M. Ebert, H. Hofmann, S. Jäckel, R. Jaenicke, P. Knippertz, K. Lieke, A. Massling, A. Petzold, A. Schladitz, B. Weinzierl, A. Wiedensohler, S. Zorn, and S. Weinbruch, “Size distribution, mass concentration, chemical and mineralogical composition and derived optical parameters of the boundary layer aerosol at Tinfou, Morocco, during SAMUM 2006,” *Tellus B* **61**, 32-50 (2009).
- [25] A. A. Kokhanovsky, and G. De Leeuw, *Satellite aerosol remote sensing over land* (Springer, 2009).
- [26] F. Lambert, J. S. Kug, R. J. Park, N. Mahowald, G. Winckler, A. Abe-Ouchi, R. O’ishi, T. Takemura, and J. H. Lee, “The role of mineral-dust aerosols in polar temperature amplification,” *Nature Climate Change* **3**, 487-491 (2013).
- [27] L.-W. Li, M.-S. Leong, T.-S. Yeo, P.-S. Kooi, and K.-Y. Tan, “Computations of spheroidal harmonics with complex arguments: A review with an algorithm,” *Physical Review E* **58**, 6792-6806 (1998).
- [28] K. N. Liou, and Y. Takano, “Light scattering by nonspherical particles: Remote sensing and climatic implications,” *Atmospheric Research* **31**, 271-298 (1994).
- [29] P. Litvinov, O. Hasekamp, and B. Cairns, “Models for surface reflection of radiance and polarized radiance: Comparison with airborne multi-angle photopolarimetric measurements and implications for modeling top-of-atmosphere measurements,” *Remote Sensing of Environment* **115**, 781-792 (2011).
- [30] C. Liu, L. Bi, R. L. Panetta, P. Yang, and M. A. Yurkin, “Comparison between the pseudo-spectral time domain method and the discrete dipole approximation for light scattering simulations,” *Optics Express* **20**, 16763-16776 (2012).

- [31] J. V. Martonchik, D. J. Diner, R. A. Kahn, T. P. Ackerman, M. E. Verstraete, B. Pinty, and H. R. Gordon, “Techniques for the retrieval of aerosol properties over land and ocean using multiangle imaging,” *IEEE Transactions on Geoscience and Remote Sensing* **36**, 1212-1227 (1998).
- [32] Z. Meng, P. Yang, G. W. Kattawar, L. Bi, K. N. Liou, and I. Laszlo, “Single-scattering properties of tri-axial ellipsoidal mineral dust aerosols: A database for application to radiative transfer calculations,” *Journal of Aerosol Science* **41**, 501-512 (2010).
- [33] M. I. Mishchenko, and L. D. Travis, “T-matrix computations of light scattering by large spheroidal particles,” *Optics Communications* **109**, 16-21 (1994).
- [34] M. I. Mishchenko, L. D. Travis, and D. W. Mackowski, “T-matrix computations of light scattering by nonspherical particles: A review,” *Journal of Quantitative Spectroscopy and Radiative Transfer* **55**, 535-575 (1996).
- [35] M. I. Mishchenko, and L. D. Travis, “Satellite retrieval of aerosol properties over the ocean using measurements of reflected sunlight: Effect of instrumental errors and aerosol absorption,” *Journal of Geophysical Research-Atmospheres* **102**, 13543-13553 (1997).
- [36] M. I. Mishchenko, and L.D. Travis, “Satellite retrieval of aerosol properties over the ocean using polarization as well as intensity of reflected sunlight,” *Journal Geophysical Research-Atmospheres*, **102**, 16989-17013 (1997).
- [37] M. I. Mishchenko, L. D. Travis, and A. A. Lacis, *Multiple scattering of light by particles: radiative transfer and coherent backscattering* (Cambridge University Press, 2006).

- [38] F. Nadal, and F. M. Breon, "Parameterization of surface polarized reflectance derived from POLDER spaceborne measurements," *IEEE Transactions on Geoscience and Remote Sensing* **37**, 1709-1718 (1999).
- [39] E. M. Patterson, D. A. Gillette, and B. H. Stockton, "Complex index of refraction between 300 and 700 nm for Saharan aerosols," *Journal of Geophysical Research* **82**, 3153-3160 (1977).
- [40] V. Ramanathan, P. J. Crutzen, J. T. Kiehl, and D. Rosenfeld, "Aerosols, climate, and the hydrological cycle," *Science* **294**, 2119-2124 (2001).
- [41] L. A. Remer, Y. J. Kaufman, D. Tanre, S. Mattoo, D. A. Chu, J. V. Martins, R. R. Li, C. Ichoku, R. C. Levy, R. G. Kleidman, T. F. Eck, E. Vermote, and B. N. Holben, "The MODIS aerosol algorithm, products, and validation," *Journal of the Atmospheric Sciences* **62**, 947-973 (2005).
- [42] C. D. Schönwiese, "Climate change 1995, the science of climate change," *Journal of Atmospheric Chemistry* **27**, 105-106 (1997).
- [43] F. M. Schulz, K. Stamnes, and J. J. Stamnes, "Scattering of Electromagnetic Waves by Spheroidal Particles: A Novel Approach Exploiting the T Matrix Computed in Spheroidal Coordinates," *Applied Optics* **37**, 7875 (1998).
- [44] F. M. Schulz, K. Stamnes, and F. Weng, "Vdisort: An Improved and Generalized Discrete Ordinate Method for Polarized (Vector) Radiative Transfer," *Journal of Quantitative Spectroscopy and Radiative Transfer* **61**, 105-122 (1999).
- [45] I. Sokolik, A. Andronova, and T. C. Johnson, "Complex refractive index of atmospheric dust aerosols," *Atmospheric Environment. Part A. General Topics* **27**, 2495-2502 (1993).

- [46] I. N. Sokolik, and O. B. Toon, “Direct radiative forcing by anthropogenic airborne mineral aerosols,” *Nature* **381**, 681-683 (1996).
- [47] A. H. Strahler, J. Muller, W. Lucht, C. Schaaf, T. Tsang, F. Gao, X. Li, P. Lewis, and M. J. Barnsley, “MODIS BRDF/albedo product: algorithm theoretical basis document version 5.0,” MODIS documentation (1999).
- [48] R. Swap, M. Garstang, S. Greco, R. Talbot, and P. Kallberg, “Saharan dust in the Amazon Basin,” *Tellus B* **44**, 133-149 (1992).
- [49] A. Sinyuk, O. Torres, and O. Dubovik, “Combined use of satellite and surface observations to infer the imaginary part of refractive index of Saharan dust,” *Geophysical Research Letters* **30(2)**, 1081-1084 (2003).
- [50] I. Tegen, S. P. Harrison, K. Kohfeld, I. C. Prentice, M. Coe, and M. Heimann, “Impact of vegetation and preferential source areas on global dust aerosol: Results from a model study,” *Journal of Geophysical Research-Atmospheres* **107(D21)**, 4576-4611 (2002).
- [51] L. Tsang, and J. A. Kong, *Scattering of Electromagnetic Waves, Advanced Topics* (Wiley-Interscience, 2001).
- [52] S. Twomey, *Introduction to the mathematics of inversion in remote sensing and indirect measurements* (Courier Dover Publications, 2002).
- [53] H. Volten, O. Munoz, E. Rol, J. F. de Haan, W. Vassen, J. W. Hovenier, K. Muinonen, and T. Nousiainen, “Scattering matrices of mineral aerosol particles at 441.6 nm and 632.8 nm,” *Journal of Geophysical Research-Atmospheres* **106**, 17375-17401 (2001).
- [54] C. Wang, P. Yang, S. L. Nasiri, S. Platnick, B. A. Baum, A. K. Heidinger, and X. Liu, “A fast radiative transfer model for visible through shortwave infrared

- spectral reflectances in clear and cloudy atmospheres,” *Journal of Quantitative Spectroscopy and Radiative Transfer* **116**, 122-131 (2013).
- [55] W. Wanner, X. Li, and A. H. Strahler, “On the Derivation of Kernels for Kernel-Driven Models of Bidirectional Reflectance,” *Journal of Geophysical Research-Atmospheres* **100**, 21077-21089 (1995).
- [56] W. J. Wiscombe, “The Delta-M Method: Rapid Yet Accurate Radiative Flux Calculations for Strongly Asymmetric Phase Functions,” *Journal of the Atmospheric Sciences* **34**, 1408-1422 (1977).
- [57] P. Yang, and K. N. Liou, “Geometric-optics-integral-equation method for light scattering by nonspherical ice crystals,” *Applied Optics* **35**, 6568-6584 (1996).
- [58] P. Yang, K. N. Liou, M. I. Mishchenko, and B.-C. Gao, “Efficient Finite-Difference Time-Domain Scheme for Light Scattering by Dielectric Particles: Application to Aerosols,” *Applied Optics* **39**, 3727-3737 (2000).
- [59] P. Yang, Z. Zhang, B. A. Baum, H.-L. Huang, and Y. Hu, “A new look at anomalous diffraction theory (ADT): Algorithm in cumulative projected-area distribution domain and modified ADT,” *Journal of Quantitative Spectroscopy and Radiative Transfer* **89**, 421-442 (2004).
- [60] B. Yi, C. N. Hsu, P. Yang, and S.-C. Tsay, “Radiative transfer simulation of dust-like aerosols: Uncertainties from particle shape and refractive index,” *Journal of Aerosol Science* **42**, 631-644 (2011).
- [61] M. A. Yurkin, and A. G. Hoekstra, “The discrete dipole approximation: An overview and recent developments,” *Journal of Quantitative Spectroscopy and Radiative Transfer* **106**, 558-589 (2007).

- [62] E. P. Zege, and L. I. Chaikovskaya, “Approximate theory of linearly polarized light propagation through a scattering medium,” *Journal of Quantitative Spectroscopy and Radiative Transfer* **66**, 413-435 (2000).
- [63] P.-W. Zhai, G. W. Kattawar, and P. Yang, “Impulse response solution to the three-dimensional vector radiative transfer equation in atmosphere-ocean systems. I. Monte Carlo method,” *Applied Optics* **47**, 1037-1047 (2008).
- [64] P. W. Zhai, Y. Hu, C. R. Trepte, and P. L. Lucker, “A vector radiative transfer model for coupled atmosphere and ocean systems based on successive order of scattering method,” *Optics Express* **17**, 2057-2079 (2009).